Data-driven Concrete Damage Diagnosis with Thermal Imaging and Vibration Testing

By

Yanqing Bao

Dissertation

Submitted to the Faculty of the

Graduate School of Vanderbilt University

in partial fulfillment of the requirements

for the degree of

DOCTOR OF PHILOSOPHY

in

Interdisciplinary Studies: Systems Engineering

March 31, 2020

Nashville, Tennessee

Approved:

Sankaran Mahadevan, Ph.D.

Douglas E. Adams, Ph.D.

Benoit Dawant, Ph.D.

D. Mitchell Wilkes, Ph.D.

To the eternal loves of my life

父兮生我　　母兮鞠我

抚我畜我　　长我育我

顾我复我　　出入腹我

欲报之德　　昊天罔极

凯风自南　　吹彼棘心

棘心夭夭　　母氏劬劳

凯风自南　　吹彼棘薪

母氏圣善　　我无令人

出其东门　　有女如云

虽则如云　　匪我思存

缟衣綦巾　　聊乐我员

ACKNOWLEDGMENTS

Words cannot express my gratitude and appreciation for all the help that my advisor and mentor, Prof. Sankaran Mahadevan has given me. First and foremost, I would like to express my heartfelt gratitude to my advisor Prof. Sankaran Mahadevan for all the dedication, diligence, patience, and rigor that he has devoted to mentoring me throughout my graduate study. He has taught me how to be a good researcher. The patience, dedication and kindness throughout these years have allowed me to get to where I am today. Many people would have given up, but you never did. You challenged me, listened to me, and guided me in such an exemplary way that I can truly say: not only am I am a better researcher today, but I am also better person because of you. For that and more, I thank you. Over the past five years, he has been an exemplary person for me to follow. The joy and enthusiasm he has for his research is contagious and motivational for me, even at the times of difficulties during Ph.D pursuit. I am deeply indebted to Prof. Mahadevan for his encouragement and enormous support during my Ph.D study. I am looking forward to opening a new chapter in our relationship for the rest of my professional career.

Besides my advisor, I would also like to gratefully acknowledge the other members of my Ph.D committee: Prof. Douglas Adams, Prof. Benoit Dawant, and Prof. D. Mitchell Wilkes for their insightful comments and valuable feedback, but also for the constructive criticisms they raised which motivated me to deepen my research from different perspectives.

I would like to extend my appreciation to all my friends those I met in Pittsburgh while I was at Carnegie Mellon, and those I met in Nashville. I appreciate all the fun we have had and all the encouragements and support you have provided. Meanwhile, I want to thank many other colleagues for all the precious time we have spent together, without which this dissertation will not have been possible. It was a great experience to work with so many brilliant people at Vanderbilt University. In particular, I was lucky to work with Dr. Zhen

Hu, who was the go-to person for most members of our risk and reliability research group. I would like to thank Dr. Chen Liang, Dr. Guowei Cai, Dr. Chenzhao Li, Dr. Saideep Nannapaneni, Dr. Abhinav Subramanian, Dr. Paromita Nath, Dr. Pranay Seshadri, Dr. Pranav Karve, and Dr. Xiaoge Zhang for their tireless support, helpful suggestions, and all the inspiring discussions in understanding and tackling challenging research problems.

Lastly, I would like to thank my parents, my wife, and the rest of my family for their boundless care, love and encouragement. Especially, I am deeply thankful to my parents for their selfless support and invaluable sacrifice they has made since I moved to the United States a decade ago. Without their constant encouragement, I could not have survived in face of the challenges.

TABLE OF CONTENTS

LIST OF TABLES

Table Page

LIST OF FIGURES

Chapter 1

Introduction

1.1 Overview

In many industries, it is desirable to detect damage and flaws in products and systems as early as possible. Structural health monitoring (SHM) plays an important role in achieving this goal for structural, mechanical, and infrastructure systems. For instance, aerospace agencies such as NASA have been investigating SHM technologies to study the safety of space shuttle components. In the semiconductor industry, companies have been adopting SHM technologies such as thermography to examine the defect in chips as well as to minimize the inadvertent downtime during manufacturing, which could cost companies millions of dollars each hour. The focus of this dissertation is on concrete structures; concrete is well known for its extreme heterogeneity. However, the proposed approaches are generally applicable to other types of materials and structures.

During the past decades, researchers have studied different types of structural health monitoring techniques by combining finite element modeling, structural dynamics, signal processing, image processing, and statistical modeling.

Thermography Analysis (TA) -related techniques are based on the assumption that defects and malfunction will also lead to change in heat flow in the material/part. TA-related techniques have been applied in Condition Monitoring (CM)/ SHM in aero-vehicle, bearings, motors, electric generators, wind turbines, etc. Infrared Radiation (IR) transmitters and high-resolution IR cameras are the sensors in the application. Depending on the resolution, TA can be used as a local or global monitoring technique. However, challenges appear for early fault detection and large-scale objects. Researchers used spatial standard deviation of temperature data to monitor the fatigue crack initiation and growth [2]. Talai et al established online structural vibration monitoring systems to evaluate the surface

cracks through thermal imaging of the vibration-induced crack [3]. Bao and Mahadevan proposed performed interior damage detection, localization and quantification in concrete using infrared thermography with image processing techniques[4].

Traditionally, vibration-based condition monitoring techniques refer to the application of in-situ non-destructive (ND) sensing and analysis of system dynamic characteristics, in time and frequency domains, which may indicate damage/degradation. The time history response of a structure can be measured by sensors such as accelerometers, strain gauges, etc. Fourier transform (FT) analysis is often used to convert the data from time domain to frequency domain. Early approaches were based on connecting the numerical models to measured modal properties from damaged and undamaged conditions. A majority of the literature focuses on the modal parameters, which could be extracted from frequency domain information. e.g. methods based on natural frequencies, mode shapes (curvatures), matrix update methods, etc.

Farrar and Doebling suggested the problem being fundamentally a statistical pattern recognition problem, and advanced non-modal based methods, also known as data-driven methods . Fugate et al. applied autoregressive function to fit the time history response data and trace the mean and variance of the residual signals for undamaged cases to form a statistical control chart. Responses from the damaged cases were fitted to the same autoregressive model, and the resulting residuals outside the control limits indicated damage. Farrar et al. used the frequency response function to develop damage-sensitive features [5]. Adams et al. used internal feedback to account for non-linearity and estimate the parameters of non-linear parametric models [6]. Hidalgo et al. proposed a wireless SHM system, and fitted autoregressive models to predict the damage based on the fitting errors [7].

Computer vision (CV) based condition monitoring is an extension of traditional visual inspection using modern computer vision and image processing techniques, such as edge detection, template matching, segmentation, etc. CV-based methods focus on the assessment of cracking, spalling, and other defects on the surface of structures such as concrete

bridge decks and asphalt pavements [8]. The major data acquisition approach is through high resolution surveillance cameras. Abdelqader et al. first pre-processed the images by line filters in different directions and then used Principal Component Analysis to reduce the dimensions of feature vectors ; then they used k-Nearest Neighbor algorithm (KNN) to perform the classification [9]. Lattanzi and Milller developed an automatic clustering method for segmentation based on the Canny algorithm and K-means to achieve crack detection [10]. Poozesh et al. performed condition monitoring on a scaled wind turbine with full-field strain and displacement information from digital image correlation (DIC) [11, 12]. Murray et al. used the full-field displacement data from DIC to monitor a reinforced concrete bridge‘‘s static and dynamic displacement and compared to the results from the sensors on the bridge [13].

Optical fiber sensing (OFS) has been widely applied in the field of life-cycle monitoring of large civil structures, such as bridges, tunnels, and geotechnical structures. The OFS has a wide range of measurands such as strains, temperatures, accelerations, deflections/displacements, cracks, and corrosions. The OFS techniques have the advantages of small size, light weight, immunity to electromagnetic interference (EMI) and corrosion, and capability of embedment, but cost vs. benefit is a challenge. An OFS system contains a light transmitter, a receiver, an optical fiber, a modulator element and a unit for signal processing. As the core unit, the optical fiber will expand or contract when strain or temperature variation occurs at its location. Thus, the reflected light will change. Optical Time-Domain Reflectometry (OTDR) sensors are the most widely applied OFS sensors, in distributed monitoring of large-scale civil structures due to their ability to measure strain and temperature over a long distance [14]. Kinet et al. applied fiber Bragg grating (FBG) sensors in composite materials health monitoring and outperformed the traditional sensors [15]. Mallik et al. used plastic optical fiber to collect vibration information on a composite cantilever beam and applied neural network to perform damage location identification [16].

However, many of the methods were developed for homogeneous materials, such as alu-

minum and steel. Some studies proposed using ultrasonic waves to perform the tests and detecting the damage through frequency-based features [17, 18], but the method has been shown only with tiny concrete brick samples; experiments on larger sizes of concrete structures need to be done. Some studies proposed to study the dynamics of a structure using a high-speed video camera with advanced image processing algorithms, such as phase-based motion magnification, optical flow estimation, etc. Methods of this type are applicable for materials like steel and aluminum but face significant challenges in concrete. Some other vibration-based methods either can only perform damage detection or meet similar challenges when translating from small lab samples to larger concrete blocks. Therefore, it is essential to develop a method that can not only detect and localize damage but also can translate its effectiveness and efficiency from small samples to larger concrete blocks.

Some studies have used finite element models to infer the condition in the interior of the structure, but the accuracy and effectiveness of such an approach strongly relies on the accuracy and resolution of the finite element model [19, 20]. For a real-world structure with complex geometry, it is difficult to build an accurate and precise finite element model due to the complexity of the structure.

During the past several years, machine learning techniques have been introduced in health monitoring. Generalized as a pattern recognition problem, classical machine learning algorithms, such as Bayes classifiers, support vector machine (SVM) classifiers, etc., have been playing an important role in damage detection when associated with damage-sensitive-features from domain knowledge. Stiffness matrices, natural frequencies and some other values from dynamics, which usually change along with the health condition of the structure, have been used to train machine learning classifiers. However, the approaches mentioned above depend on and are limited by the accuracy and effectiveness of the physical models. Therefore, data-driven structural health monitoring has become a promising direction for complex structures with complicated material properties.

Building a general machine learning system requires careful engineering and tremen-

dous domain knowledge to design an effective feature. It is because that traditional machine learning algorithms are limited in their ability to process raw data directly from the experiment. The process of establishing an effective feature is usually tedious and require much effort in trial and error. Deep-learning methods, in the family of representation learning methods, enable the model to be fed with raw data and to find the appropriate representations required for detection and classification automatically. Deep-learning methods contain multiple levels of representations. A typical deep-learning model contains multiple simple but non-linear modules, and each of them transforms the representations into the next level with slightly more abstract representations, starting from the raw input to the output decision-making. Deep-learning algorithms are powerful in exploring the intricate structure in high-dimensional datasets. Therefore, deep learning has been applied in many fields such as face recognition, speech recognition, particle accelerator data analysis, brain circuit reconstruction, etc. The application of deep-learning methods in structural health monitoring is still in the infant phase, and the utilization of deep-learning so far has focused on replacing human visual inspection, such as steel rust detection, steel delamination detection, surface crack detection, etc.

An individual SHM technique with one type of data source usually has its limits. Therefore, it is desirable to provide a versatile capability for damage diagnosis by fusing multiple techniques and multiple data sources. Given that each of the monitoring techniques has its advantages and drawbacks (suitability for local damage vs. overall damage, surface crack or internal damage, etc.), the motivation of the research in this dissertation is to improve the damage diagnosis system with information fusion techniques. In addition, the uncertainty in the diagnosis is also significant to investigate. As we include multiple monitoring techniques and multiple datasets for information fusion, each of them will contain different types of uncertainty sources. For any individual damage diagnosis algorithm, there will be uncertainty in parameter selection. Further, uncertainty also exists during data acquisition from the experiments, and in processing the data. Using the methods of uncertainty

quantification, we will be able to incorporate multiple uncertainty sources and estimate the overall uncertainty in diagnosis.

The primary research objective of this dissertation research is to investigate the application of cutting-edge deep learning techniques in structural health monitoring (SHM) along with traditional SHM techniques of general scope (e.g., thermography and high-speed images with advanced image processing algorithms) and SHM techniques of local scope (e.g., pitch-catch tests, strain measurements at individual locations). Moreover, the proposed dissertation research also investigates information fusion and uncertainty quantification of combining multiple monitoring techniques for decision-making.

To demonstrate the proposed methodologies, we focus on concrete material, which is well-known to be a challenging material due to its extreme heterogeneity. One of the essential parts of the proposed research is to carry out experiments and collect data from multiple structural health monitoring techniques. However, the methodologies are not limited to just concrete but can be translated to other types of materials, such as metal, composite materials as well.

Thermography has been used much in structural health monitoring on metal materials, such as steel and aluminum. Little progress in research has been achieved on heterogeneous materials, such as concrete. Meanwhile, previous monitoring techniques with thermography have relied on engineers‘‘ experience and judgement to detect the potential defect or damage. In this research, we improved the techniques and provided engineer with a directed decision map about the structure by using advanced image processing techniques. The direct decision map is capable of multiple tasks, such as to detect, localize, and quantify the damage.

Vibration-based techniques also have significant applications in structural health monitoring. Guided-wave based pitch-catch test has been used for SHM in metals, such as steel plates and steel pipes. Swept-wave testing is used in monitoring wind turbines. A critical part of this research combines these two methods and establishes an effective and robust

damage-sensitive feature for detection using singular value decomposition (SVD). We also use the crest factor concept from signal processing to assist the damage localization.

Deep learning methods have shown great power over traditional machine learning techniques for applications with large datasets such as image classification, object detection, natural language processing, and DNA sequencing. In this research, we first generate training image datasets using finite element analysis. Then, we investigate the application of deep learning methods to perform damage diagnosis with images obtained using SHM techniques such as thermography.

This research considers multiple data analysis methods on datasets obtained from multiple monitoring techniques. Each method and monitoring technique will have its strength and drawbacks, and there are multiple uncertainty sources within each method. This research investigates how to quantify the uncertainty in the diagnosis.

1.2 Research Objectives

The research in this dissertation involves extensive experimental effort. Therefore, the first objective is to design and implement the experiments and data acquisition process for multiple monitoring techniques.

The second objective is to investigate structural health monitoring with advanced image processing techniques. The advantage of optical monitoring techniques, such as thermography and high-speed imaging, is that they are equivalent to having thousands of sensors and each screenshot contains thousands of measurements. Advanced image processing techniques can assist researchers to extract more information for a full-field damage diagnosis, such as edge detectors, optical flow estimation, image pyramid, phase-based motion magnification, etc.

The third objective is to investigate structural health monitoring with vibration testing and signal processing techniques. We treat structural health monitoring problem as a data-mining problem, with techniques such as singular value decomposition (SVD), K-means

clustering, and support vector machines (SVM). We use guided-wave harmonic vibration experiments as an example to demonstrate the method. The method is demonstrated with concrete specimens of different sizes to detect and localize the damage.

The fourth objective is to investigate the application of deep learning techniques in structural health monitoring. This one aims to fill the research gap that traditional image processing-based SHM techniques takes much time and effort in building and tuning the damage sensitive features and current deep learning-based techniques fail to handle damages other than the surface cracks. The goal of our proposed technique for this objective is to handle the internal damage and automate the feature generation. It uses the idea of transfer learning to take advantage of the current sophisticated pre-trained deep learning architectures, which is extremely helpful for small dataset problems, such as most cases in SHM. The method is demonstrated with thermography testing on concrete specimens to identify the most likely damage location.

The fifth objective is to investigate the uncertainty quantification and robustness within each of the proposed structural damage diagnosis methods. This investigation is conducted individually for each of the structural health monitoring techniques in this dissertation.

1.3 Dissertation Organization

This dissertation is organized to address the research objectives listed in 1.2. Chapter 3 investigates an image processing technique for internal damage diagnosis in concrete based on thermal imaging. Chapter 4 uses vibration-based testing to develop a framework for damage detection and localization in heterogeneous materials such as concrete. Chapter 5 develops a convolutional neural network based interior damage diagnosis framework using both computer simulation data and experimental data. The first objective (data generation with experiments and computer simulations) and the fifth objective (uncertain and robustness studies) will be addressed in each of Chapters (in relation to the particular technique considered) 3, 4, and 5. Chapter 6 concludes the dissertation summarizing the

accomplishments and outlining future directions.

Chapter 2

Background

2.1 Selected Image Processing Techniques in Structural Health Monitoring

This section briefly reviews the main filtering techniques used later in the dissertation for damage diagnosis using image processing. Figure 1 shows the general procedure of structural damage diagnosis using image processing. Images of the surface are first acquired. Second, different kinds of filters are applied for noise cancellation in the raw images to remove the environmental and operational effects. Third, based on the image content or objective of the monitoring process, different kinds of algorithms are applied to calculate the features of the image. Lastly, damage diagnosis decision making is accomplished based on appropriate criteria.

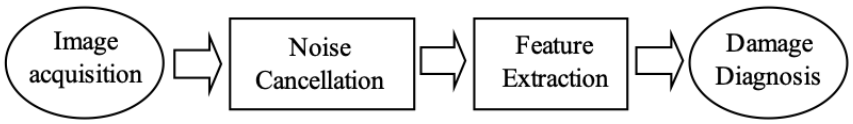

Figure 2.1: Steps in damage diagnosis using image processing

2.1.1 2-Dimensional simple moving average filter

In the noise cancellation step in Figure 2.1, a moving average filter tends to smooth out short-term variations and leaves in the long-term changes, by taking an average value of the data within a fixed-size window. The window shifts from one side of the data series to the other, thus covering the entire dataset [21]. Moving average has been used for time series analysis in many fields such as financial analysis, signal processing, etc[22]. There are usually three types of moving average approaches: simple moving average, cu-

mulative moving average, and weighted moving average [23]. The thermal images appear to have relatively long-term variation. Considering the balance between effectiveness and computational expense, the Simple Moving Average (SMA) filter is adequate [24], and is described as

$$\hat{P} = \frac{P_M + P_{M-1} + ... + P_{M-(n-1)}}{n} \tag{2.1}$$

where $\hat{P}$ is the new value at the middle point of vector, $P_M + P_{M-1} + ... + P_{M-(n-1)}$, P_i is the original value at position i, and n is the length of the vector[25].

2.1.2 Sobel filter

Image processing typically has two approaches to extract features: color-based and texture-based. In our system, the thermal images have differences in contours which reflects the heat conductivity difference. Therefore, a texture filter, such as Sobel filter, is more appropriate in our case. The Sobel filter, also called Sobel Operator, is one of the most commonly applied in image processing for edge detection. The Sobel filter used here contains two 3 by 3 convolution masks as follows [26, 27].

$$S_x = \begin{bmatrix} -1 & 0 & 1 \\ -2 & 0 & 2 \\ -1 & 0 & 1 \end{bmatrix} \tag{2.2}$$

$$S_y = \begin{bmatrix} 1 & 2 & 1 \\ 0 & 0 & 0 \\ -1 & -2 & -1 \end{bmatrix} \tag{2.3}$$

Given an image A, to apply the Sobel Filter, we usually convolve the mask separately with the input image to obtain the corresponding gradient component (g_x and g_y) along each direction as follows [26].

$$g_x = S_x * A \tag{2.4}$$

$$g_y = S_y * A \tag{2.5}$$

Typically, based on the above two formulas, the gradient magnitude, G, and the angle of the image orientation, ϕ, can be calculated as [27]

$$G = \sqrt{g_x^2 + g_y^2} \tag{2.6}$$

$$\phi = arctan(\frac{g_x}{g_y}) \tag{2.7}$$

As one of the most commonly applied methods in the gradient-based filter family, the Sobel filter uses the property that an edge is usually characterized by a threshold value of the gradient. Since the pixel intensity value at the edges will be usually higher than their surrounding pixels, a threshold value is commonly set [28, 29]. And an edge will be declared when the calculated gradient at a pixel crosses the threshold.

2.2 Singular value decomposition and reconstruction

Singular Value Decomposition (SVD) performs a linear decomposition of the data to create a set of orthogonal bases [30, 31]. Given a matrix $X_{m\times n}$, with a rank of $r < n < m$, the SVD method decomposes the matrix as

$$X = USV^T \tag{2.8}$$

where U is an $m \times m$ matrix and the columns, U_k, called left singular vectors, form an orthonormal basis. S is an $m \times n$ rectangular diagonal matrix. V^T is an $n \times n$ matrix and the rows, V_k^T, called right singular vectors, form another orthonormal basis.

SVD has been commonly used for dimension reduction, in reducing model complexity and computational burden by effectively representing the dataset with lower dimensions. It also has been applied to create features from the face images in face recognition applications [32, 33]. In the field of structural health monitoring, several researchers have been applying SVD for the calculation of natural frequencies or as a type of dimension reduction technique [34, 35].

2.3 Comparing signals with the crest factor metric

In signal processing, the crest factor or K-factor, is used to measure the deviation of a signal from a sinusoidal waveform [36]. Given a signal y_i, RMS stands for root mean square value, and one definition of the K-factor is

$$K = max(y_i) \times RMS(y_i) \tag{2.9}$$

To better illustrate the performance of the K-factor, we show a few simple examples of how the K-factor value changes for different signals. These signals were created by combining two different sinusoidal components (one with a higher frequency and one with a lower frequency). The waveforms and the corresponding K-factor value are shown in each of the subplots of Figure.2.2. Subplots (a) and (b) show a relatively high frequency wave and a relatively low frequency wave. And their K-factors are 0.7067 and 0.70048 respectively. In an ideal case, namely an infinitely long pure sinusoidal wave of magnitude 1, the K-factor would be $\frac{1}{\sqrt{2}}$ (roughly 0.707). In the subplot (c) and (d), we mixed the high frequency signal with the low frequency signal in two different ratios, 90% high signal with 10% low signal and 90% low signal with 10% high signal and we keep the energy of the synthetic signals to be the same and in (e) we mixed them in equal proportion (50/50), which makes it less sinusoidal. Their calculated K-factors increased a little but still close to the theoretical value of the ideal case.

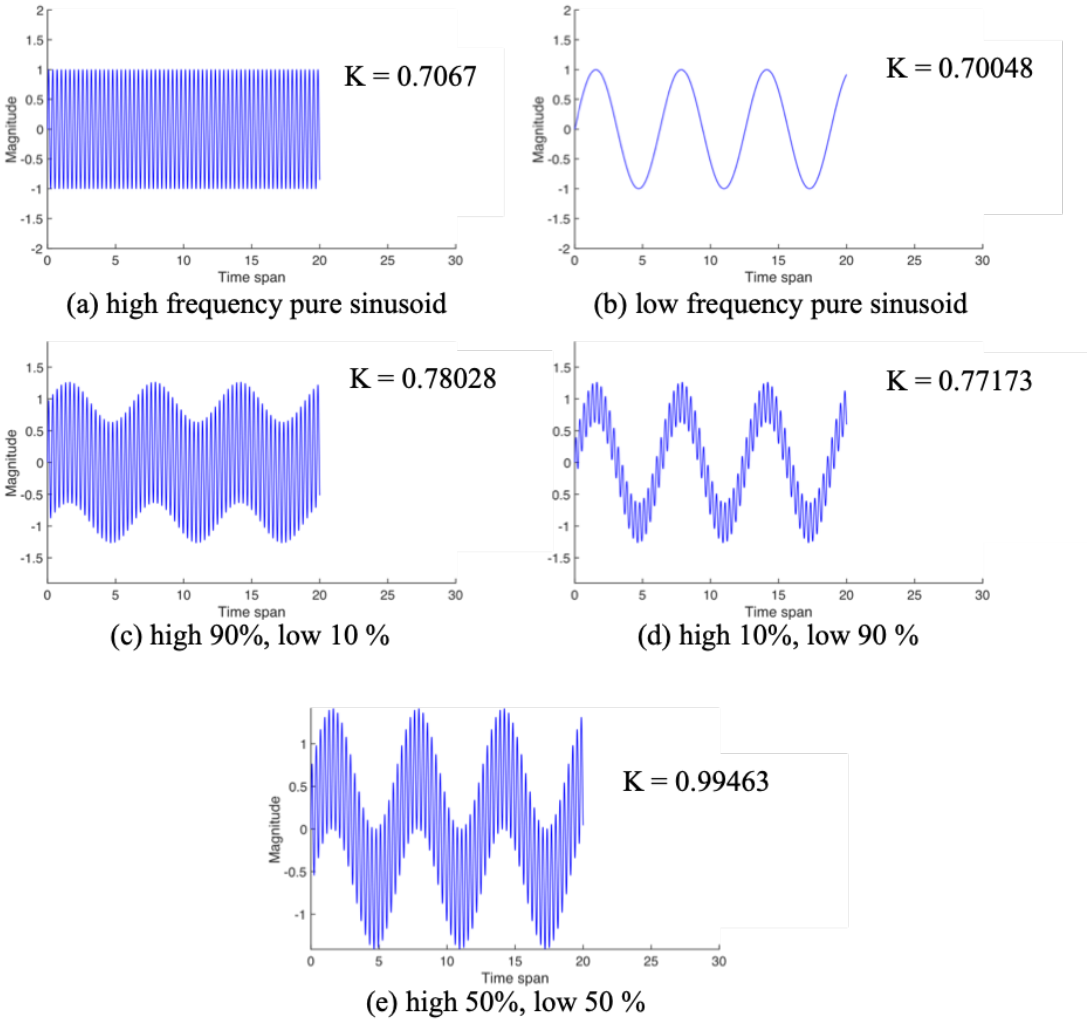

Figure 2.2: K-factor values for different signals

Therefore, the *K*-factor can be used to describe the deviation of a signal from a pure sinusoidal wave. The more the signal deviates from a sinusoid, the higher the crest *K*-factor will be. The assumption is that the damage in the structure changes the property of the structure such that the acquired signal would be different (deviated) from the signal source (pure sinusoid wave).

2.4 k-means clustering

As mentioned previously, during the damage localization step, we need to use clustering methods to differentiate the locations of the damaged regions from the locations of the intact regions. The k-means clustering method, which is a classical clustering method, is a possible technique for this purpose. Therefore, in this section, we present some basic concepts of k-means clustering.

In signal processing and machine learning, the k-means clustering algorithm aims to partition the given observations into k clusters. Here, k is predetermined and stands for the number of clusters one sets up [34, 35].

Given n observations $x_1, x_2, x_3, ‘‘, x_n$, the k-means clustering algorithm allocates each observation into one of the k clusters by minimizing the distance between that point and the centroid of the allocated cluster μ_j. There are several different approaches to perform the optimization, such as an expectation-maximization (EM) algorithm [37, 38]. Following is a pseudocode to perform k-means clustering using EM:

- Determine the number of clusters, k;
- Initialize k centroids randomly, μ_1, μ_2, ‘‘, μ_k;
- Allocate each observation to the cluster with the closest centroid (Euclidean distance);
- Update the centroids based on the observations assigned;
- Repeat the allocation and updating steps until clustering results become stable.

In Chapter 4 , we apply k-means clustering to the calculated K-factor values from different candidate damage locations. Based on our assumption, the K-factor values reflect the damage severity. Therefore, we track the corresponding locations of the K-factor values from each of the clusters and identify damage zones with different damage levels.

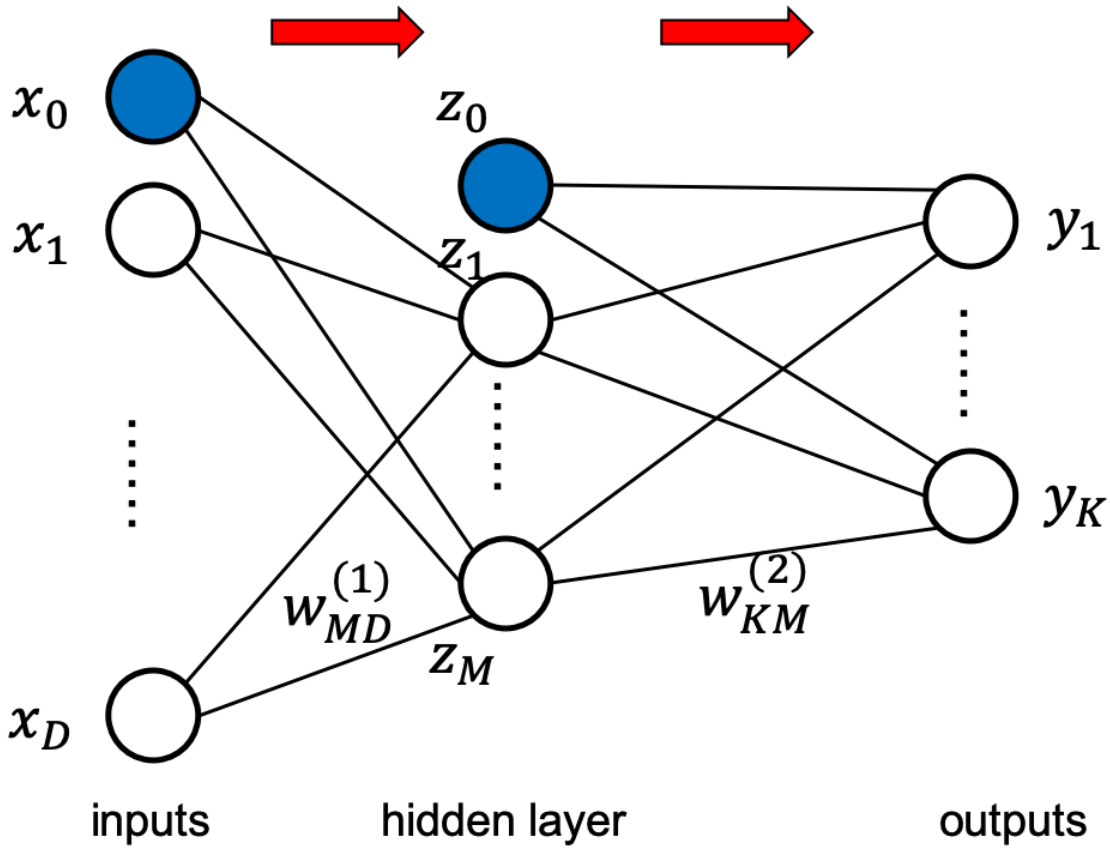

Figure 2.3: Feed-forward neural network architecture

A basic type of neural network model is the feed-forward neural network, also known as the multi-layer perceptron. An example of the feed-forward network is shown in Figure 2.3. In the input layer x_1 to x_D represent the input variables. x_0 is the bias term for the input layer. $w_{ji}^{(n)}$ is the corresponding weight from node i in the $n-1$th layer to node j in the nth layer. The forward computation consists of two parts: linear combination and non-linear activation. First, we construct the linear combination of the input nodes (including bias term) with corresponding weights as shown in Eq. 2.10

$$a_j = \sum_{i=1}^{D} w_{ji}^{(1)} x_i + w_{j0}^{(1)} \tag{2.10}$$

Second, we transform the results from the linear combination through a nonlinear, but

differentiable activation function $\sigma_i()$ as shown in Eq. 2.11. The purpose of applying the activation function is to bring nonlinear features into the neural network model to fit complex data sets. Some of the commonly used activation functions are logistic sigmoid (Eq. 2.12), softmax (Eq. 2.13), and ReLU (short for Rectified Linear Units) activation function (Eq. 2.14; in practice, sometimes a_j is directly used instead of computing $\sigma_{sigmoid}(a_j)$). The choice of the activation function is based on the nature of the input data and the expected distribution of the output variables.

$$z_j = \sigma_1(a_j) \tag{2.11}$$

$$\sigma_{sigmoid}(a_j) = \frac{1}{1+exp(-a_j)} \tag{2.12}$$

$$\sigma_{softmax}(a_j) = \frac{exp(a_j)}{\sum_j exp(a_j)} \tag{2.13}$$

$$\sigma_{ReLU}(a_j) = max(0, \sigma_{sigmoid}(a_j)) \tag{2.14}$$

The model shown in Figure 2.3 can be summarized into Eq. 2.15. Since the neural network model only contains linear combination and a differentiable activation function, the parameters of the model are trained through error back-propagation algorithms, such as the Adam optimizer. The detailed procedure of the error back-propagation and Adam optimizer can be found in [39].

$$\mathbf{y} = \sigma_2(\Sigma_{j=0}^{M} w_{kj}^{(2)} \sigma_1(\Sigma_{i=0}^{D} w_{ji}^{(0)} x_i)) \tag{2.15}$$

2.6 Convolutional neural network

Convolutional neural networks (CNNs), also known as convnets, belong to an important category of neural networks used to process grid-like data sets. CNNs have been widely applied in the fields of computer vision, image processing, and time-series analysis and have become state-of-the-art techniques for tasks such as image classification and object detection. CNNs and other deep learning techniques have also been proven significantly effective in other fields, such as medical image segmentation in CT and MRI scans [40, 41].

CNN layers contain two important operations: convolution and pooling. The convolution operation follows the form in Eq. 2.16, where I represents the input (such as the pixel values of an image), K represents the kernels (sometimes called filters), S represents the output (sometimes called feature map), and i, j, m, n are the indices for rows and columns. One of the major advantages of the convolution layer is parameter sharing over traditional neural networks, such as the feed-forward neural network. Each of the nodes in a feed-forward neural network has its own weights, as shown in Eq. 2.10 [42]. However, in convolution layers, each of the kernels is applied to all the input values. Parameter sharing significantly cuts down the computational expense and makes the CNN more efficient in representing complex models.

$$S(i,j) = (I * K)(i,j) = \Sigma_m \Sigma_n I(m,n) K(i-m, j-n) \tag{2.16}$$

The pooling operation replaces the elements in the output from the previous layer with summary statistics of their neighboring elements. Some common pooling operations are max pooling (maximum value within a rectangular region) and average pooling (average value within a rectangular region). With selected stride sizes, the pooling operation can reduce the number of the nodes to pass to the next layer. This is essential in handling model inputs of large sizes or varying sizes due to high-resolution images [42].

2.7 Transfer learning and VGG nets

Transfer learning assumes that the knowledge learned in one task T_1 has overlap with another task T_2. Therefore, the models for task T_1 (done previously) should offer us advance insights for T_2 and accelerate the training of new models for T_2. This is because many of the tasks share the same pre-processing steps, such as measuring geometrical shapes, low-level edges, repeated patterns, and changes in lighting conditions [42]. Transfer learning helps to model the field with fewer data sets (for instance, the SHM task) using the parameters learned from fields with abundant data sets [43]. The model proposed in this chapter takes the VGG-19 CNN model as base layer and then adds layers to specifically handle the damage diagnosis of the structural specimen of interest.

VGG-19 was developed by the Visual Geometry Group at Oxford and had successful results in the ImageNet Large Scale Visual Recognition Challenge (ILVRC 2012) [44, 45, 46]. Although the model has 19 layers, it is still concise and elegant. Deeper layers provide better performance and smaller convolution filters than previous deep neural networks, and balanced the computational cost and performance. This is because that the model consists of repeated simple modules (convolution layers with small 3×3 kernels) of convolution and pooling operations. The CNN configuration of the VGG-19 is summarized in Table 2.1. All convolution operations use ReLU as their activation function. The VGG-19 model contains 144 million parameters in total, and the parameters trained on ImageNet are available in the public domain [44].

2.8 Uncertainty Quantification

It is known that the damage diagnosis results from the monitoring techniques have significant variation, regarding the diagnosis accuracy, etc. Several uncertainty sources contribute to the overall uncertainty in diagnosis, such as natural variability, measurement uncertainty, data processing uncertainty, and model uncertainty. Uncertainty quantification

Input (224×224 **RGB images)**
conv3-64
conv3-64
max-pool
conv3-128
conv3-128
max-pool
conv3-256
conv3-256
conv3-256
conv3-256
max-pool
conv3-512
conv3-512
conv3-512
conv3-512
max-pool
conv3-512
conv3-512
conv3-512
conv3-512
max-pool

Table 2.1: Configuration of CNN part in the VGG-19 neural network

involves both forward propagation of uncertainty from model inputs and parameters to the output, and inverse analysis in terms of quantifying the various uncertainty sources. Background information is provided here for two forward analysis techniques, namely Monte Carlo simulation and sensitivity analysis

2.8.1 Monte Carlo Simulation for forward uncertainty propagation

The interest in forward uncertainty propagation is to find the expectation of some function $f(x)$, corresponding to a probability distribution $p(x)$ [47]. Considering a continuous variable, the expectation is written as

$$E[f] = \int f(x)p(x)dx \tag{2.17}$$

However, sometimes the expectation is too complex to be evaluated using an analytical method. Therefore, the principal idea behind Monte Carlo simulation is to draw N samples independently from distribution $p(x)$ [28]. Then, the integral in Eq. 2.17 is approximated as

$$E\hat{[}f] = \frac{1}{N}\sum_{i=1}^{N} f(x_i) \tag{2.18}$$

2.8.2 Global Sensitivity Analysis

The purpose of sensitivity analysis is to learn how the output of a given model depends on its inputs. There are two types of sensitivity analysis in practice, local sensitivity analysis, and global sensitivity analysis. Local sensitivity analysis is performed at a specific given point in the region of inputs, typically based on derivatives [48]. On the other hand, the global sensitivity analyses focus on the study of the output uncertainty when the input parameters vary along the entire region of themselves [48]. As a form of global sensitivity analysis, variance-based sensitivity analyses decomposes the variance of the output into portions from each input and quantifies the sensitivity based on the percentage of variance corresponding to each input. Mathematically, the variance-based global sensitivity analysis can be expressed as follows. Given a model

$$y = f(X) \tag{2.19}$$

where y is the model‘‘s output, and X denotes a series of model inputs, i.e., x_1, x_2‘‘x_n. The decomposition of variance is expressed as

$$Var(y) = \sum_{i=1}^{n} V_i + \sum_{i<j}^{n} V_{i,j} + \sum_{i=1}^{n} V_{1,2,\ldots,n} \tag{2.20}$$

$$V_i = Var_{X_i}(E_{X\,i}(y|X_i)) \tag{2.21}$$

$$V_{i,j} = Var_{X_{i,j}}(E_{X_{\ i,j}}(y|X_{i,j})) \tag{2.22}$$

where X_i denotes the i-th variables in vector X. $X_{\ i}$ in Eq. 3.3 denotes all other input variables except X_i . $X_{i,j}$ in Eq. 3.4 denotes all other input variables except X_i and X_j.

Based on the above decomposition, the first order sensitivity index is expressed as [49, 50]

$$S_i = \frac{V_i}{Var(y)} \tag{2.23}$$

This first order sensitivity index measures the contribution to the output variance from x_i alone. To analysis the global sensitivity, several methods have been proposed. The Fourier amplitude sensitivity test (FAST) was suggested in the 1970s and is still one of the most elegant methods for sensitivity analysis. By calculating multivariate integrals through the Monte Carlo Method, Sobol indices are efficiently calculated [51, 52]. Li and Mahadevan proposed to estimate the first-order Sobol index using modularized sample-based method[53]. Hu and Mahadevan proposed to used enhance surrogate with global sensitivity analysis for reliability analysis [54]. Sankararaman and Mahadevan includes both aleatory and epistemic uncertainties in their method[55].

2.9 Summary

This chapter reviewed some of the fundamental and theoretical concepts, which are used in the following chapters. Selected image processing techniques (2D-Moving average filter, Sobel filter) will be used to implement thermal image-based damage diagnosis in Chapter 3. Concepts of singular value decomposition and reconstruction, K-factor analysis, and k-means clustering will be used to develop a vibration-based damage diagnosis methodology in Chapter 4. Neural network related concepts, including activation functions, convolutional neural work, VGG nets, and transfer learning are discussed in preparation for

Chapter 5.

Chapter 3

Thermal Image-Based Concrete Diagnosis

3.1 Introduction

Image processing has been studied for several decades in many different engineering applications. With the rapid development in computing speed and storage capabilities in recent years, image processing has rapidly advanced in several directions, such as image compression, enhancement and restoration. Image compression focuses on the balance between fewer bits for image representation vs. deterioration in quality. Image enhancement and image restoration techniques have been studied to improve the quality of an image, usually through raising the contrast of the image from the background either for better visualization by the human eye or for better detection by the computing algorithm [56]. With respect to image enhancement, researchers have studied several techniques such as threshold transformation [57], logarithmic transformation [58], histogram equalization [19, 20], and local enhancement [17].

Digital image processing techniques have also been studied in the context of non-destructive testing (NDT) of structures and materials in recent years. Researchers have tried to apply image processing to monitor and evaluate the condition of concrete structures using different type of imaging systems. Ito et al. proposed an automatic detection technique for cracks in a concrete block by utilizing image-processing techniques on raw images acquired by a high-resolution camera. Fujita et al. implemented a line-filter and threshold processing to improve the robustness of the above method [59, 60]. Edge-detection algorithms and statistical methods [18, 61, 62] have been advocated and evaluated for assessing images obtained by acoustic televiewers and high-resolution cameras. An automatic detection and quantification technique for micro-cracks and other micro-defects was introduced based on scanning electron microscope (SEM) and optical microscope images [63].

Image processing using high-resolution camera, acoustic televiewers, scanning electron microscope (SEM), and optical microscopes are rather effective in identifying micro-cracks or largely propagated cracks on the *surface* of concrete. But none of them are helpful in interior structure inspection, since interior damage may not cause detectable external change until the damage has progressed to a considerable extent. X-ray tomography has been studied and applied in internal structure diagnosis [64]. However, as a radioactive and hazardous technique, X-ray tomography is not suitable for frequent inspections. Therefore, an automated, less hazardous internal damage detection method is attractive, considering both efficiency, effectiveness and capabilities of internal damage assessment.

In this chapter, we investigate the processing of thermal images for internal defect diagnosis (detection, localization and quantification) in concrete. Thermographic cameras have been used to detect the differences of temperature in the material in the health monitoring of metallic components such as turbine blades [65, 66]. The idea behind this is that defects or irregularity in a material might cause differences in heat conductivity and temperature diffusivity, when compared with intact material [67, 68]. Thermographic damage diagnosis has been applied locally and globally [69, 70, 71, 72]. One influential factor is the resolution of the thermographic camera [73]. Typically, in image processing, the parameters were selected based on the experts‘‘ experiences. The chapter proposed a more sophisticated approach for parameter selection through Bayesian updating.

The image processing technique consists of four steps: cropping, smoothing, feature identification, and decision-making. Each of these steps requires the selection of values for the processing parameters, which will affect the diagnosis result in turn. We will elaborate the parameters in our proposed method in Session 3. In reality, however, it is hard to determine which values should be chosen for these parameters. In order to study the uncertainty in the diagnosis result, we first perform Monte Carlo simulation of the image processing system by randomly choosing values of the image processing parameters. Next, the contributions of various image processing parameters to the uncertainty in the diag-

nosis result are analyzed using the global sensitivity analysis (GSA) technique. Finally, a Bayesian approach is pursued to select the optimal values of parameters for the image processing system. The obtained optimal parameters can provide guidance in the selection of parameters for damage diagnosis of similar structures. Thus the proposed damage diagnosis methodology consists of four elements: (1) thermal image processing, (2) uncertainty quantification, (3) sensitivity analysis, and (4) parameter selection.

The remainder of the chapter is organized as follows. Section 3.2 describes the proposed methodology for damage diagnosis in concrete, using thermal image processing, uncertainty quantification, sensitivity analysis, and parameter selection. Section 3.3 illustrates the implementation of the proposed methodology for a concrete slab. Finally, Section 3.4 provides concluding remarks.

3.2 Proposed Methodology

In this section, we will first discuss how thermal image processing can be implemented for internal damage diagnosis. Following that, we will quantify the uncertainty in the diagnosis results and develop the method for selecting the optimal values of image processing parameters.

3.2.1 Damage Diagnosis Using Thermal Image Processing

The main idea of using thermal image processing for damage detection is that an internal damage beneath the surface will cause a discontinuity in the thermal conductivity of the material. Therefore, the captured images will be different from those of the original, intact material in heating cycles. As long as differences in images exist, we can distinguish them by calculating features with image processing algorithms.

Figure 3.1 provides a flowchart of the thermal image processing system for internal damage diagnosis. The inputs of the system are raw images captured from thermographic camera. Due to the limitations of the camera and experimental setup, some portion of an

image may capture regions that are not related to the studied specimen. Therefore, the first step of our image processing system is to crop the raw image to remove the irrelevant parts. Secondly, with the cropped image, a same size cropped image from an intact structure is subtracted from the acquired one as baseline removal [21]. After that, a smoothing filter (namely, SMA filter) mentioned in Section 2.1.1 is employed for noise-cancellation [21]. With the smoothed image, the feature extraction filter (namely, Sobel filter) as reviewed in Section 2.1.2 is used for feature calculation. With the calculated features, we can apply threshold settings for pixel-wise decision-making. After scanning through the entire image, a pixel-wise damage detection and decision matrix is produced and can be shown as a black-and-white image (suspected damage shown as white spots in Figure 6). Based on the aforementioned matrix, the amount of damage is estimated. In order to determine the location of the damage, a pixel-to-length unit convertor first needs be calculated based on photogrammetry and the relative positions of the camera and the specimen. An illustrative example will be provided shortly.

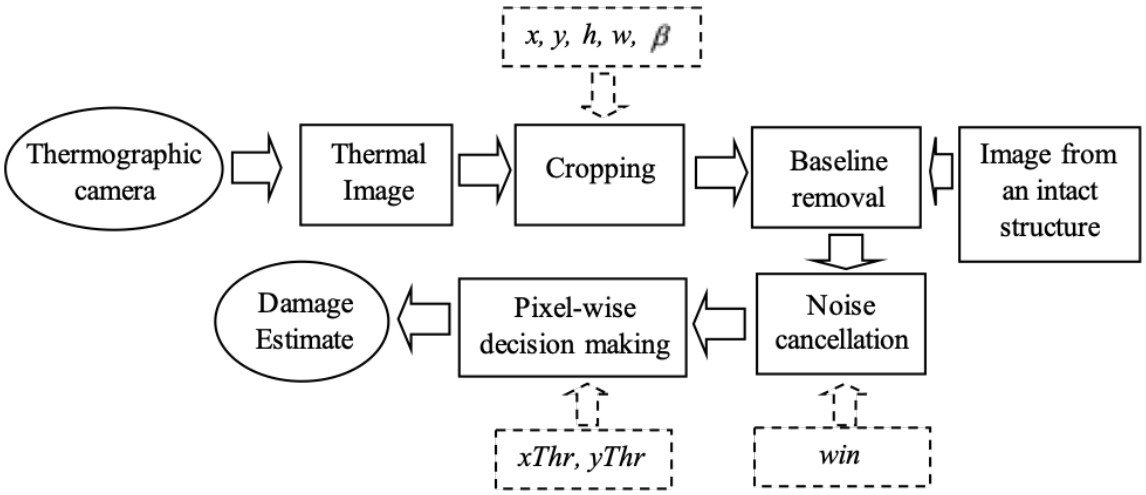

Figure 3.1: Flowchart of internal damage diagnosis of concrete

In Figure 3.1, each of the dashed boxes contains the parameters that need to be determined for the corresponding image processing step. In the cropping step, we have x and y

, representing the x and y coordinates of the starting point; h and w, representing the height and weight of the cropped images; and β representing the potential rotation of the studied specimen. In the noise cancellation step, we have, *win*, which is the window size of the selected smoothing filter. In the pixel-wise decision making step, we have $xThr$ and $yThr$, which are the threshold values for the x gradient and y gradient respectively. Even if some empirical ranges can be provided for these parameters, determining the optimal values of the parameters is not straightforward.

In order to quantify the effects of the image processing parameters on the damage diagnosis results, the next step is to perform uncertainty quantification of the damage diagnosis, and assess the relative contributions of different parameters to the diagnosis uncertainty through sensitivity analysis.

3.2.2 Uncertainty quantification and Sensitivity Analysis

As mentioned in Section 3.2.1, ranges of values may be available, based on previous experience, for the parameters in the image processing system. Based on the intervals, we first use Monte Carlo sampling to quantify the uncertainty in the diagnosis results. We then use global sensitivity analysis to identify important parameters. The noises and errors in the measurement and numerical method are also considered during this process.

The Monte Carlo simulation is performed by generating random realizations of the image processing parameters. Uniform distributions over the aforementioned ranges are used for the random sampling of the parameter values, in the absence of any information about preferred values. It should be noted here that, even though we use Monte Carlo simulation, the image processing parameters are not random variables. Their values are chosen by the analyst, and the chosen value affects the diagnosis result. The purpose of using Monte Carlo simulation and sensitivity analysis is to observe the effect of the choices on the diagnosis result in a quantitative manner. In addition, this exercise can also shed light on the stability of the image processing procedure, by observing whether the diagnosis

result changes slightly or drastically for a small perturbation of the parameter values.

The purpose of sensitivity analysis is to analyze how the output of a given model is affected by its inputs. There are two types of sensitivity analysis in practice, local sensitivity analysis and global sensitivity analysis. Local sensitivity analysis is performed at a specific given point in the region of inputs. Global sensitivity analysis focuses on the study of the output uncertainty by considering the variation of the input parameters over their entire range [74, 75]. As a form of global sensitivity analysis, variance-based sensitivity analysis decomposes the variance of the output into contributions from each input and quantifies the sensitivity based on the percentage of variance corresponding to each input. Mathematically, variance-based global sensitivity analysis can be expressed as follows [21]. Given a model

$$y = g(X) \tag{3.1}$$

where y is the model output and X denotes a vector of model inputs, i.e. $x_1, x_2, ..., x_n$.

The decomposition of variance is expressed as

$$Var(y) = \sum_{i=1}^{n} V_i + \sum_{i<j}^{n} V_{i,j} + \sum_{i=1}^{n} V_{1,2,...,n} \tag{3.2}$$

$$V_i = Var_{X_i}(E_{X_{\sim i}}(y|X_i)) \tag{3.3}$$

$$V_{i,j} = Var_{X_{i,j}}(E_{X_{\sim i,j}}(y|X_{i,j})) \tag{3.4}$$

where X_i denotes the i-th variables in vector X. $X_{\sim i}$ in Eq. 3.3 denotes all other input variables except X_i . $X_{\sim i,j}$ in Eq. 3.4 denotes all other input variables except X_i and X_j.

Based on the above decomposition, the first order sensitivity index is expressed as [49, 50]

$$S_i = \frac{V_i}{Var(y)} \tag{3.5}$$

This first order sensitivity index measures the individual contribution of x_i to the output variance. The index is practically computed by calculating the multivariate integrals in Eq. 3.6 and Eq.3.7 through Monte Carlo sampling [35]. By investigating the global sensitivity results, we can distinguish the parameters of more significant impact on the desired output from those with less significant impact. This information can be used to narrow the study to the most important parameters for more detailed investigation [51, 52].

3.2.3 Selection of Optimal Image Processing Parameter Values

Define the input parameters of the damage diagnosis system as $\alpha = [x, y, win, xThr, yThr]$, and expressing the damage diagnosis result mathematically as $r = g(\ \alpha) + e_r$, where r is the estimated amount of damage, $g()$ is the internal damage diagnosis system, and e_r is the error in the diagnosis system. Then the optimization problem to identify the optimal values of the image processing parameters α is formulated as $argmin(|r - r_{true}|)$ where $r = g(\ \alpha) + e_r$, r_{true} is the true damage and $\alpha \in \Omega$, where Ω stands for the random domain of the input variables.

Due to the fact that r_{true} is unknown during actual diagnosis and the input parameters can be chose as any value in the domain Ω, solving the optimization model given above is impossible during actual diagnosis. However, if the damage diagnosis system is to be applied to a class of similar structures, we may able to calibrate the optimal parameters for the internal damage diagnosis system based on experimental observation of $r_t rue$ for a given structure.

Three approaches commonly available for parameter estimation can also be used to solve the optimization problem. The least squares (LS) approach attempts to minimize the square of the sum of differences between the observed data and the model prediction. The

maximum likelihood estimator (MLE) obtains the value of α that maximizes the likelihood $f(r_{true}|\ \alpha\ )$. A third approach is to use Bayesian estimation, and the parameter values could be selected as maximum a posteriori (MAP) estimates, thus including any prior information about the parameters in the estimation [29]. If a uniform prior is assumed, then the MAP estimate is the same as the MLE estimate. The Bayesian approach is used in this chapter.

Thus the problem of image processing parameter value selection is solved through a parameter estimation approach in this chapter. Note that the selection of the processing parameter values is actually a design problem; the analyst gets to select these values. However, using a parameter estimation approach is a convenient way to solve the design problem and is mathematically correct.

Using Bayes‘‘ theorem, the posterior distribution of the image processing system parameters are computed as

$$f(\boldsymbol{\alpha}|r_{true}) = \frac{f(r_t rue|\boldsymbol{\alpha})f(\boldsymbol{\alpha})}{\int f(r_t rue|\boldsymbol{\alpha})f(\boldsymbol{\alpha})d\boldsymbol{\alpha}} \tag{3.6}$$

where $r_t rue$ is the true damage extent, $\boldsymbol{\alpha}$ represents the parameters selected in the image processing system. $f(\boldsymbol{\alpha})$ represents the prior distributions of the parameters. $f(r_t rue|\boldsymbol{\alpha})$ represents the likelihood of the true damage extent of the particular parameter selections. $f(\boldsymbol{\alpha}|r_{true})$ represents the posterior of the distributions of the image processing parameter given the true damage extent.

Markov Chain Monte Carlo(MCMC) simulation is commonly used to estimate the posterior distribution based on the following proportionality relationship:

$$p(\boldsymbol{\alpha}|r_{true}) \propto p(r_{true}|\boldsymbol{\alpha})p(\boldsymbol{\alpha}) \tag{3.7}$$

In this chapter, MCMC is implemented using the Python package PyMC, and the Metropolis-Hastings sampling method is used [76, 74, 75].

Thus we obtain the optimal parameters for the image processing system. It should be

noted that the optimal parameter values may vary with structure and damage geometry. The obtained optimal parameters are only applicable to structures with similar features and damage characteristics as the structure used for the parameter optimization. An illustrative example is given in the next section to explain the implementation procedure of the proposed framework.

3.3 Illustrative Example

Damage detection in a concrete slab is used to illustrate the proposed methodology. The experimental setup is first described, followed by description of the diagnosis implementation and parameter estimation.

3.3.1 Experimental Setup

The thermal imaging experiment was carried out on concrete slabs with dimensions (in inches) $15.5 \times 15.5 \times 1.75$. The slab was placed on a thermal blanket for uniform heating at the bottom, and a thermographic camera was placed to take pictures from over the top of the slab. To simulate internal damage, three parallel holes with different sizes were drilled from one side of the concrete slab. The dimensions and positions of the holes are shown in Figure 3.2. Experiments were carried out both before and after drilling. The images were taken while the slab was subjected to heating. Applied heating profile is provided in Figure 3.4.

3.3.2 Data Collection

The images were obtained using an FLIR‘ Infrared (IR) camera from the top of the slab every 2 minutes during the experiment. The relative positions of the slab and the thermographic camera are shown in Figure 3.3.

The temperature profile of the heating blanket is shown in the following image. And

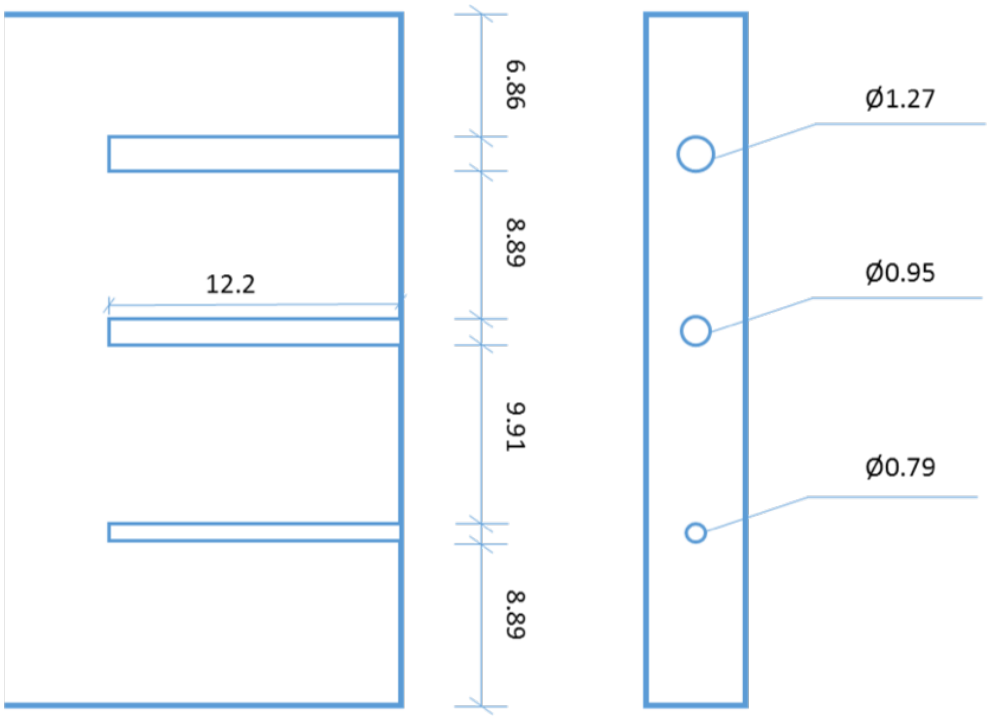

Figure 3.2: Dimensions and locations of the holes in the concrete slab (cm)

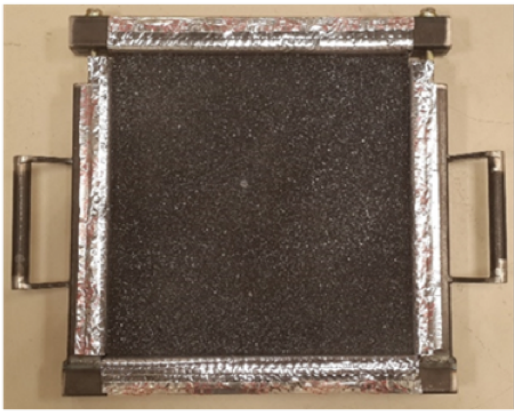

Concrete slab

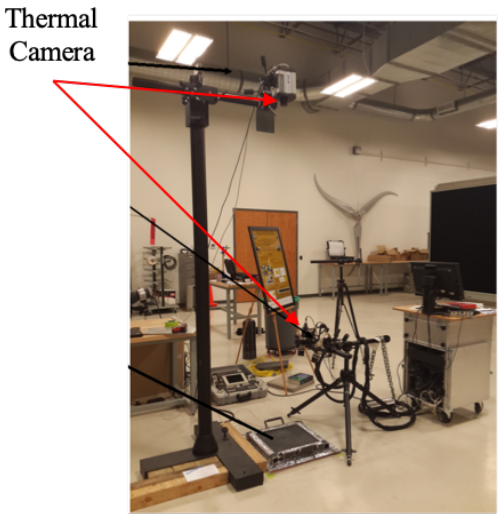

Experimental setup

Figure 3.3: Positions of the thermographic camera and concrete slab

the image selected for parameter optimization is at 18^{th} minute. The reason for choosing that particular time instant is that at the beginning of the heating cycle, initial conditions dominate and it may take a while for the heating blanket and other equipment to function smoothly. Since the internal damage in the concrete will have effect on the heat conductivity in the corresponding area, the images that are taken while the temperature of the slab is increasing should reflect the heat conductivity of the internal condition better than during steady temperature. Thus we selected 18^{th} minute, which is immediately after the temperature of the heating blanket reaches its maximum value.

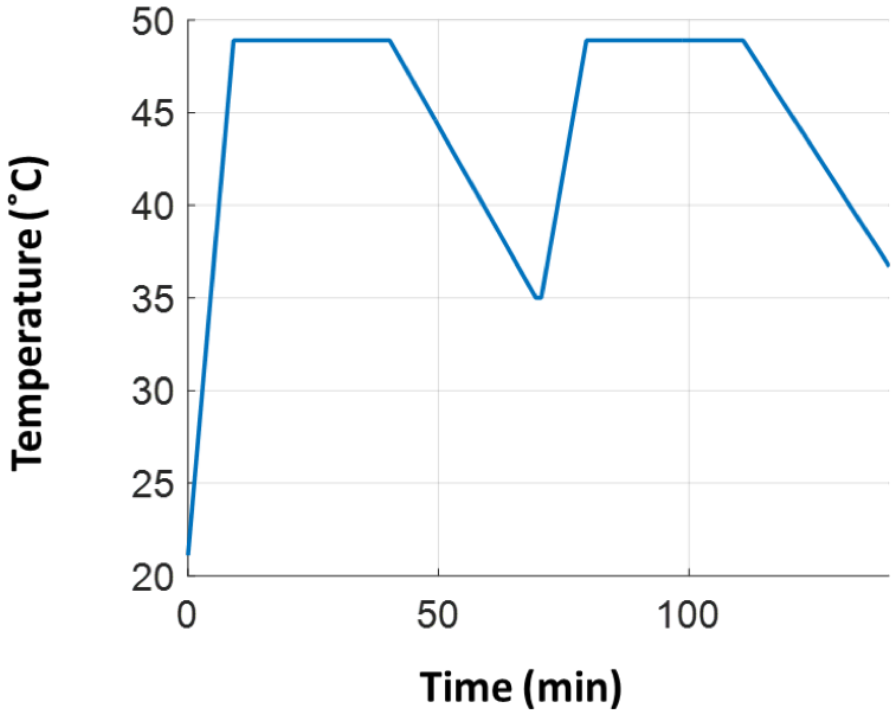

Figure 3.4: Temperature profile in the thermal blanket

The images were taken for both the intact concrete slab and the drilled slab. Figure 3.5 shows one collected raw image for the slab with the holes.

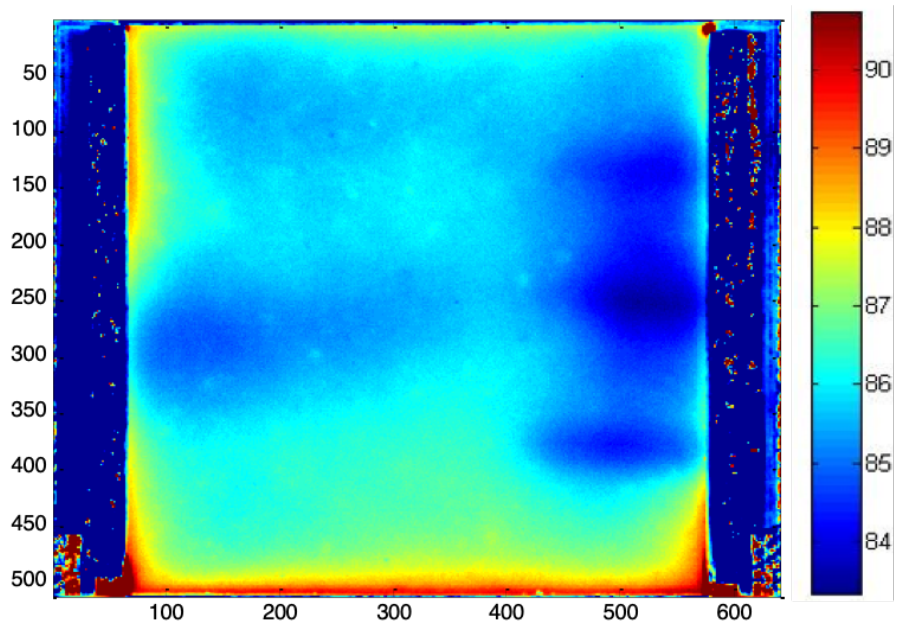

Figure 3.5: Raw image from thermographic camera

3.3.3 Image Processing Methodology

As shown in Figure 3.4, due to the limitation of the camera, there are segments on both edges, which are due to the metal frame and unrelated to the concrete slab. Therefore, the first step is to crop the image into purely concrete part. Next, a cropped image of the same size from an intact slab is subtracted from the acquired one for baseline removal. After that, a 2-dimensional simple moving average filter, with a window-size *win*, is applied for noise-cancellation [77] as described in Section 2.1. With the smoothed image, a Sobel filter is employed to calculate the gradients (features) g_x and g_y of the image as introduced in Section 2.1.2. A threshold value needs to be selected for each feature; in each pixel, if both $xThr$ and $yThr$ are below the corresponding threshold; damage is declared at that pixel. After scanning through the entire image, a pixel-wise damage detection and decision matrix is produced and can be shown as a black-and-white image (suspected damage shown as white spots in Figure 3.6).

The location of damage can be quantified based on the pixel-wise damage matrix. In this calculation, the length-to-pixel convertor is as follows,

$$1pix \approx 0.0777cm \iff 12.86pix/cm \tag{3.8}$$

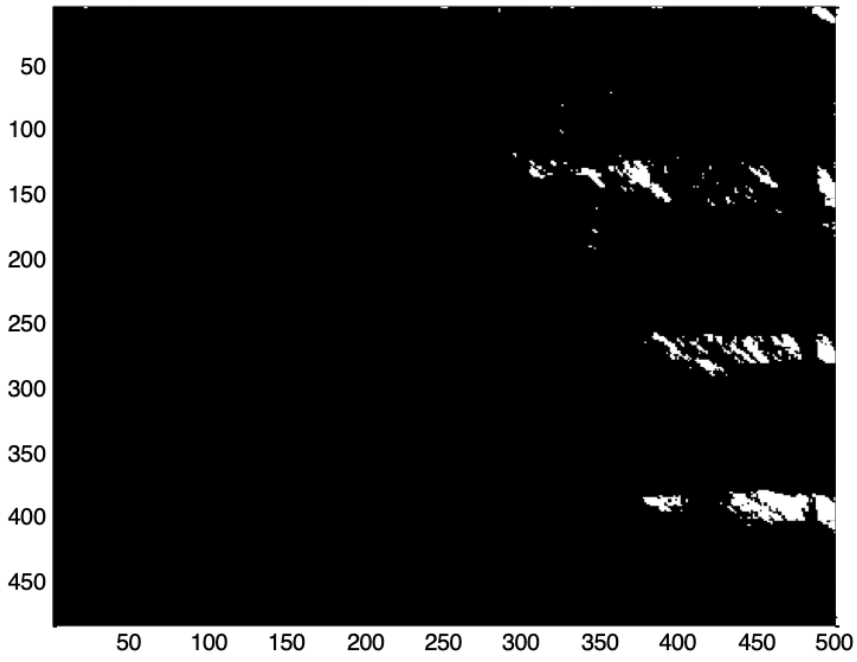

Figure 3.6: Pixel-wise damage detection and decision matrix (parameter values: [$x = 74$, $y = 16$, $win = 25$, $xThr = 0.08$, $yThr = -0.08$)]

The extent of damage is first provided by the pixel counts in terms of the damage area-ratio defined as

$$\psi = \frac{N_d}{N_t} \tag{3.9}$$

where ψ is the damaged area ratio, N_d is the number of suspected internal damage pixels and N_t is the total number of pixels within the cropped image.

We make an assumption that the area ratio, ψ, calculated in Eq. 3.9 is equal to the actual area ratio in the concrete slab. With the calculated area ratio, ψ from Eq. 3.9 and

knowing the physical area of the slab, A, we build the following relationship:

$$A_d = \psi A \tag{3.10}$$

where A_d is the estimated damaged area.

The function above is deterministic, which means that given a combination of all the five parameters and the measurement of the concrete slab dimensions, estimated damaged area, A_d is a fixed number. However, the analyst is uncertain about the values to be selected for these parameters; each combination of the parameter values will give a different result. Next, we will investigate how to quantify the uncertainty in the diagnosis result due to the uncertainty regarding parameter selection. As the three parallel holes are not extremely close to each other, we can assume that they are independent. Therefore, we can further predict the damage area individually. Based on the Eq. 3.8, Eq. 3.9, and Eq. 3.10, we can calculate the damage area for upper hole, $16.324cm^2$, the damage area for middle hole, $17.075cm^2$, and the damage area for lower hole, $12.436cm^2$. Compared with the true areas, $15.494cm^2$, $11.590cm^2$, and $9.638cm^2$, though the middle hole area seems relatively overestimated, the estimated results are close the true values. We are able to estimate the diameter of each of the drilled holes from Figure 3.6, upper hole, $2.33cm$, middle hole, $1.55cm$, and lower hole, $1.32cm$. Compared with the true diameters: $1.27cm$, $0.95cm$, and $0.79cm$, the estimations are also very close to the truth.

3.3.4 Uncertainty Quantification and Sensitivity Analysis

As mentioned in Section 3.3.2, we assume that the parameter settings in the image processing steps are independent from each other [78]. The selected range of x and y are based on direct observation of the raw images. The range of window size *win* is assumed to be 15 to 35 pixels. The selected ranges of $xThr$ and $yThr$ are based on trial and error, namely, a process that carries out a greedy search on different parameter combinations for

suitable settings.

For the purpose of uncertainty quantification using Monte Carlo simulation, all five parameters are sampled from uniform distributions, since there is no information regarding preferred values for the parameters. Table 3.1 summarizes the five variables in the image processing system. Note that x, y ,and win refer to the coordinate and smoothing window size, which are measured in pixels, whereas, $xThr$ and $yThr$ are threshold values of gradients. Therefore, we sample x, y, and win from discrete uniform distributions, and $xThr$ and $yThr$ from continuous uniform distributions. The lower and upper bounds of the uniform distributions are also given in Table 3.1.

Variable	x	y	win	$xThr$	$yThr$
Distribution	**Uniform (D)**	**Uniform (D)**	**Uniform (D)**	**Uniform (C)**	**Uniform (C)**
Parameters	[64, 84]	[6, 26]	[15, 35]	[0, 0.1]	[-0.1, 0]

Table 3.1: Five variables of the image processing system and their empirical intervals Variable. Note: D: discrete distribution (in our case: only take integer values), C: continuous distribution

From each of the distributions in Table 3.1, we randomly draw $30,000$ samples. With each realization of the parameter values, the four image processing steps are applied according to the procedure given in Figure 2.1 in order to calculate the estimated damage area. With the $30,000$ values of estimated damaged area, A_d, the histogram is plotted as in Figure 3.7. The total computation time for the Monte Carlo simulation is about 31.3 hours on a 4-core-CPU computer.

The true damage area (known because we drilled the holes to a specified size) is $36.008cm^2$. From the MCS results in Figure 3.7, we can observe that the peak of the histogram of estimated damage area is at about $60cm^2$ assuming that the area ratio in the cropped image carries over to the full slab. If we directly compute the damage area from the pixels and the convertor in Eq. 3.8 without carrying the area ratio to the full slab, the peak of the histogram is still at about $56cm^2$. Thus there is a conservative overestimation of damaged area with the thermal imaging technique in this example. This is expected, be-

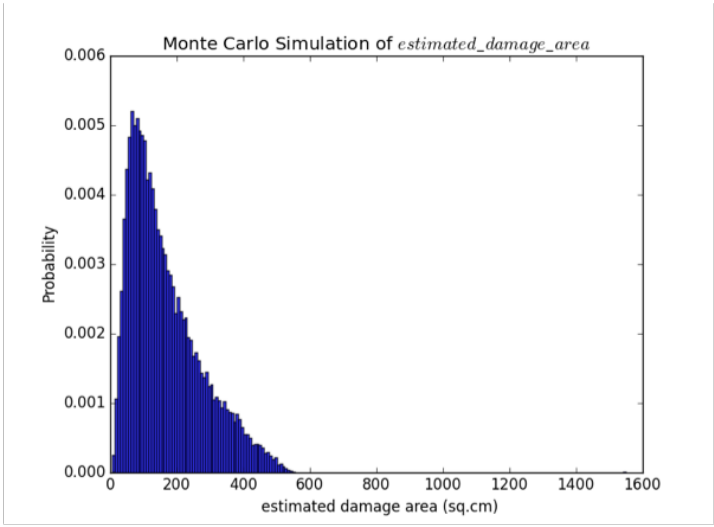

Figure 3.7: Histogram of estimated damaged area obtained from MCS

cause the thermal conductivity of the areas adjacent to the holes is reduced by the presence of the holes, and therefore these adjacent areas are also identified as damaged through the image processing analysis. This is also visually seen in Figure 3.6, where the white pixels cover widths larger than the true widths of the three holes.

Next we perform global sensitivity analysis of the damage diagnosis result, and Table 3.2 gives the first-order indices (i.e., individual effects).

Variable	x	y	win	$xThr$	$yThr$
First-order indices	0.001622	0.031796	0.028584	0.75492	0.069603

Table 3.2: Global sensitivity analysis results

Table 3.2 indicates that $xThr$ has the highest first-order sensitivity index, followed by $yThr$. It implies that the selection of $xThr$ and $yThr$ is critical for the accuracy of the diagnosis result. The reason for a dominant sensitivity of $xThr$ is considered as the geometric spread of the drilled holes in the concrete slab. As shown in Figure 3.5, due to the specific geometry of the holes, the temperature field in the slab varies less horizontally(x-direction) than vertically(y-direction). Therefore, a small change in will make a significant difference

in the decision making result, i.e. $xThr$ should have a relatively high sensitivity. In the next section, we select optimal values of these parameters based on our knowledge of the true damage.

3.3.5 Selection of Optimal Parameters

In this example, we assume that the error e_r, in the system follows normal distribution. The mean of the error is the assumed to be zero, and the variance is unknown and needs to be estimated along with the parameters. We use a uniform prior for the standard deviation (σ $Uniform[0.01, 0.0126]$). Figure 3.8 shows a simple Bayesian network connecting all the variables, output and observation.

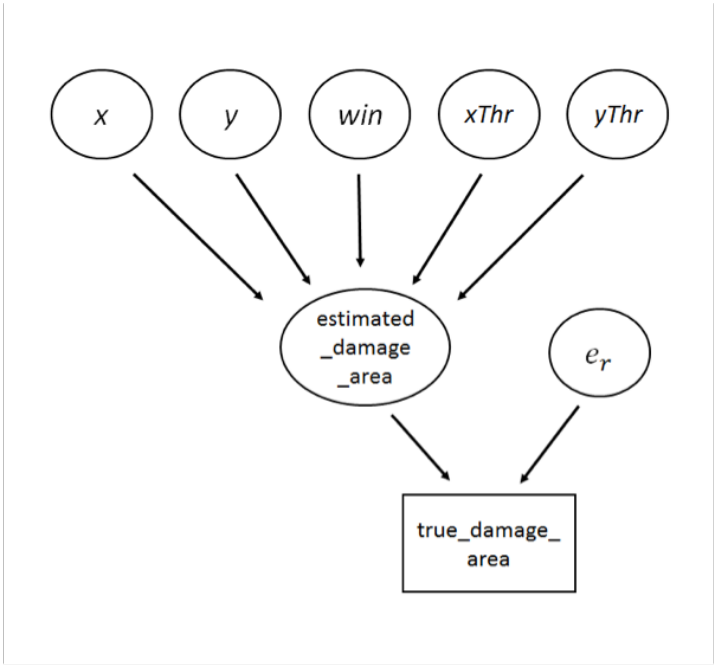

Figure 3.8: Bayesian model connecting processing parameters and the output

We estimate the posterior distributions of the processing parameters based on the Bayesian updating mentioned in Section 3.3.3. Figures. 3.9 - 3.13 give the obtained posterior distributions of the image processing parameters. We ran 10000 samples for MCMC using

Metropolis-Hastings algorithm. As the algorithm takes some iterations to reach a steady state [79], we discarded the first 1000 samples. The total computational time is about 26.9 hours on a 4-core-CPU computer.

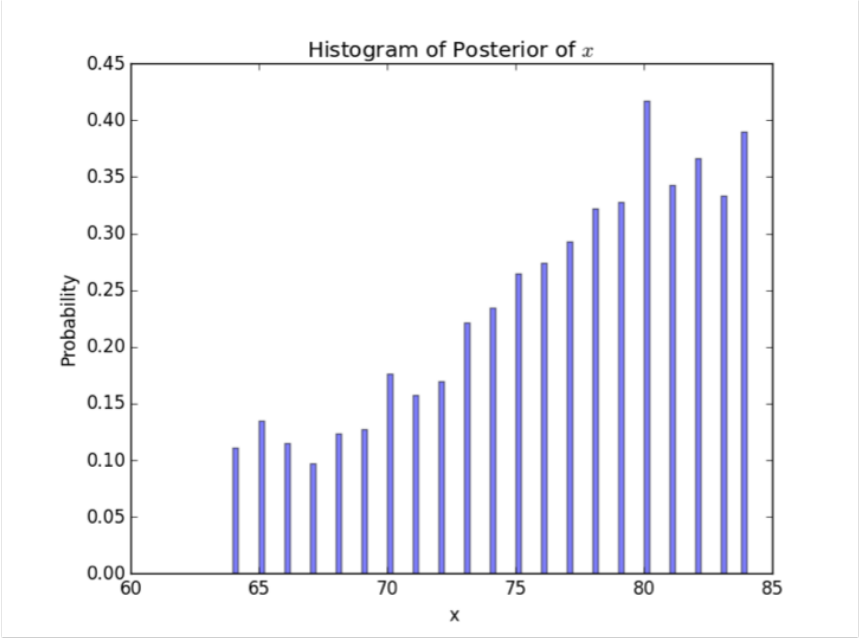

Figure 3.9: Posterior distribution of x

The posterior distributions of x, y, and *win* do not provide much guidance for selecting their optimal values. This result is expected, since these three parameters were observed to have very low sensitivity indices (Table 3.2). In the case of significant parameters $xThr$ and $yThr$ the MAP estimates are found to be $xThr = 0.09$ and $yThr = -0.09$; these estimates are similar to the result from trial and error: $xThr = 0.08$ and $yThr = -0.08$. By the Eqs. 3.8 - 3.10, we calculate the damage area using parameters from Bayesian updating, $26.706cm^2$ and the parameters from trial-and-error, $45.835cm^2$. Compared with the true area, $36.008cm^2$, the result from Bayesian updating parameters is more aggressive and the result from trial-and-error seems more conservative.

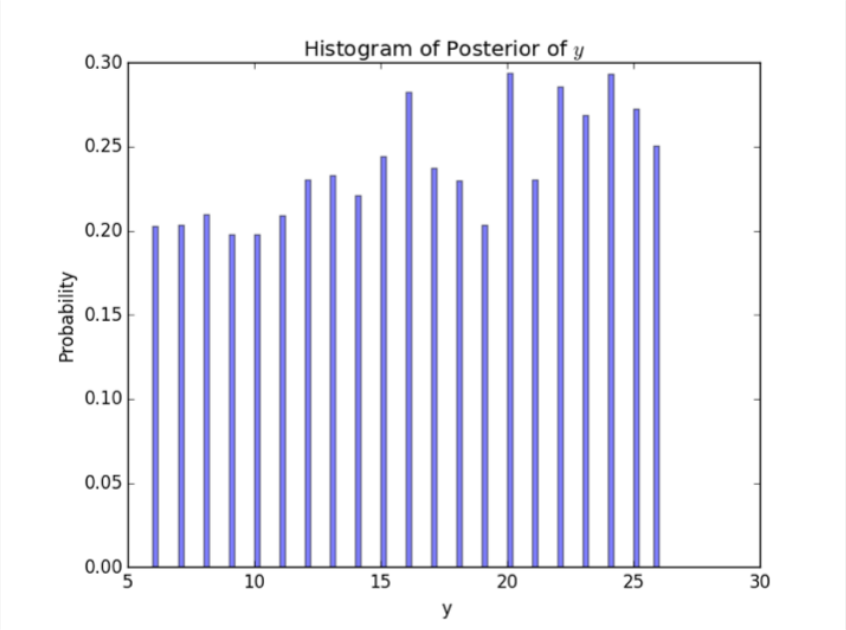

Figure 3.10: Posterior distribution of y

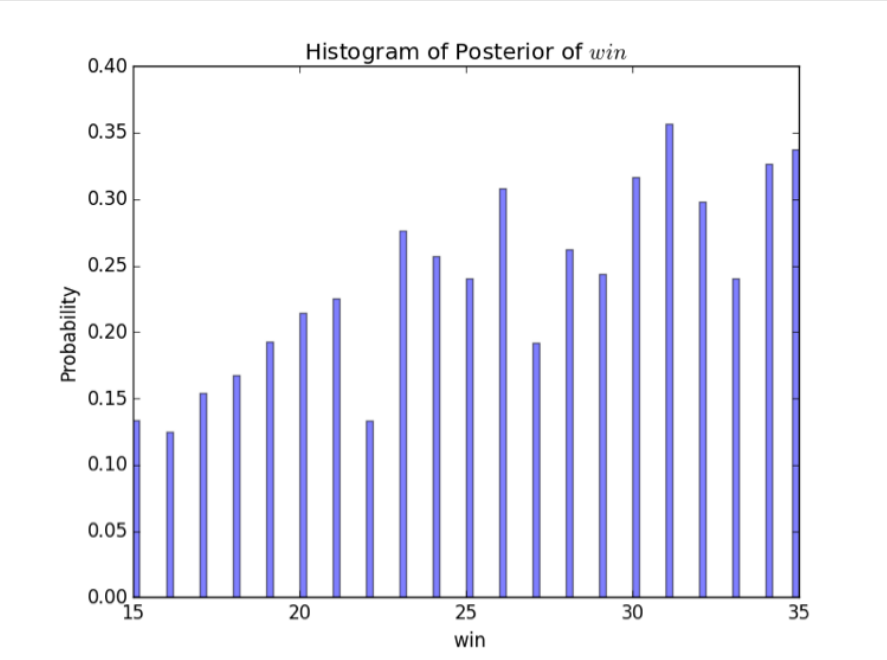

Figure 3.11: Posterior distribution of *win*

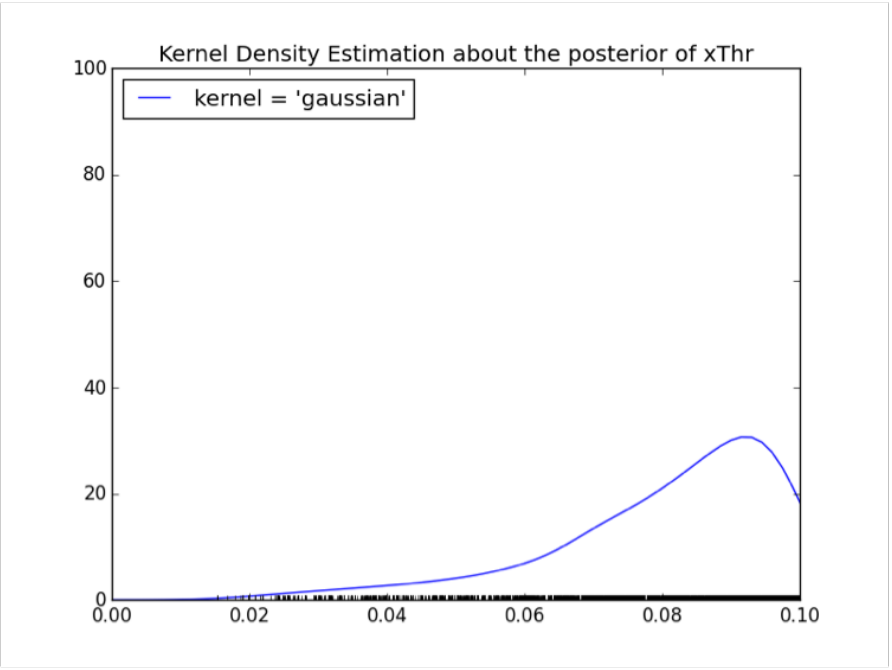

Figure 3.12: Posterior distribution of $xThr$

3.4 Conclusion

This chapter investigated thermal image processing for internal damage detection, localization and quantification in concrete. From the Monte Carlo simulation, we are able to gain insight into the uncertainty of the diagnosis result based on ranges of the values for the image processing parameters. The sensitivity analysis identifies the significant parameters that affect the diagnosis uncertainty. The Bayesian approach is able to identify optimum values of the significant parameters. The proposed damage detection and quantification framework is validated by the damage of drilled holes due to the fact that concrete specimen casting and curing consume weeks. Specimens containing other kinds of damages should be casted and tested to study the generality of the proposed damage diagnosis framework. Chapter 4 explores damage detection and localization based on vibration testing.

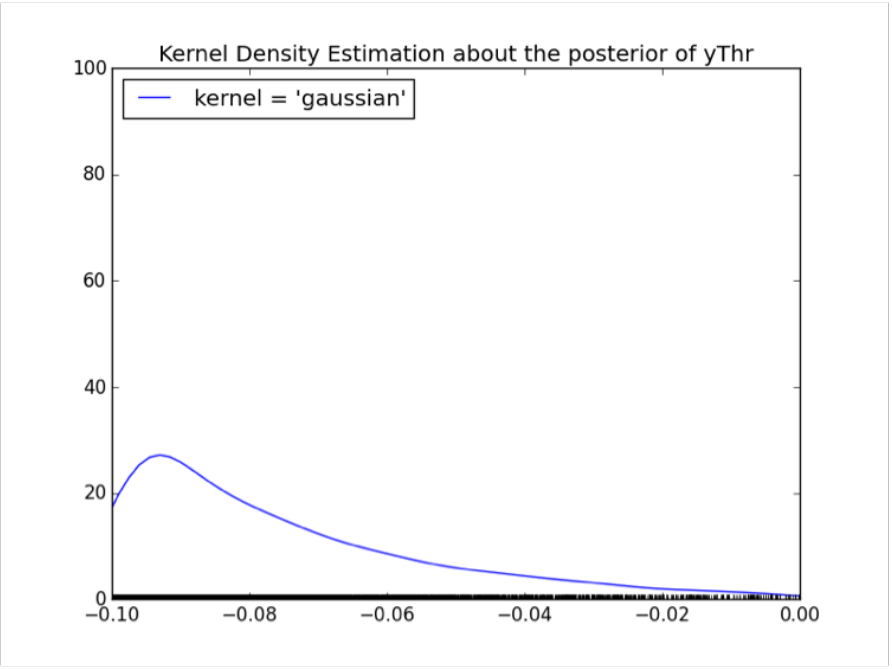

Figure 3.13: Posterior distribution of $yThr$

Chapter 4

Harmonic Vibration Testing for Damage Detection and Localization

4.1 Introduction

Condition monitoring or health monitoring in heterogeneous materials, such as concrete, has been a challenging problem. Researchers have studied different types of structural health monitoring techniques using structural dynamics, signal processing, image processing, and finite element and statistical modeling [80, 81, 82]. However, many of the methods were developed for homogeneous materials, such as aluminum and steel. (Finite element modeling has been used for the prediction of structural condition and verification of experimental observations, and model updates have been done using monitoring data [83, 84]. And for real-world structure with complex geometry, it is complicated to build an accurate and precise finite element model due to the complexity of the structure.) Some studies proposed using ultrasonic waves to perform the tests and detecting the damage through frequency-based features [85, 86]. But the method has been shown only with very small concrete brick samples. Meanwhile, experiments on larger sizes of concrete structures need to be done. Some studies proposed to study the dynamics of a structure using a high-speed video camera and advanced image processing algorithms such as phase-based motion magnification, optical flow estimation, etc. [87, 88]. Methods of this type are applicable for materials like steel and aluminum but face significant challenges in concrete. Other studies proposed using infra-red thermography to perform damage detection and localization [4]. But due to the limitation of the camera and the low heat conductivity of the concrete, these methods also face challenges for larger size concrete blocks. Some other vibration-based methods either can only perform damage detection or meet similar challenges when applying the technique developed from small laboratory samples to larger concrete blocks [89, 90, 91, 92, 93]. Recent studies have considered hybrid condition mon-

itoring of concrete with embedded PZT and optical fibers [94]; this approach is feasible only for new structures. Other studies have built ultrasonic tomography systems for evaluating concrete structures [95], but the method requires access to both sides of the structure, causing challenges when one side of the structure is not accessible (e.g., the inner side of the concrete shield around a nuclear reactor). Therefore, it is important to develop a method that can not only detect and localize damage but also can achieve simplicity, effectiveness and efficiency in applications to large concrete structures.

This chapter investigates swept and harmonic vibration tests for damage diagnosis in concrete. This work is inspired by the research on pipeline health monitoring using guided ultrasonic waves and the research on using swept waves for detecting cracks within steel beams [96, 97, 36, 98]. A robust SVD-based damage-sensitive feature is developed for damage detection, and a damage location-sensitive K-factor metric is developed for damage localization. To demonstrate and validate the proposed two-stage damage diagnosis framework, experiments are carried out on patio blocks (thin slabs) and medium-sized concrete blocks. At the damage localization stage, we propose to use unsupervised learning techniques to cluster the locations of intact parts and damaged parts. There are many clustering methods and for demonstration purposes, we use k-means clustering, a classic clustering method, in this chapter.

The rest of the chapter is organized as follows. In Section 4.2, we present the proposed two-stage damage diagnosis methodology, and describe the steps to calculate the proposed SVD-based damage-sensitive feature and the K-factor metric. In Section 4.3, we describe our experiments on different concrete samples with different types and amounts of damage, and demonstrate the methodology through the analysis of the collected datasets. In Section 4.4, we conclude the chapter with a brief summary.

4.2 Proposed Methodology

The proposed methodology consists of two stages, i.e., detection and localization. During the detection stage, there are two inputs, namely, the data collected previously on the intact sample (to compute the left singular vectors) and the newly received data from the sample whose health status is unknown. Both of these datasets are from sine-sweep harmonic vibration experiments. The core part of the first stage is to compute the proposed SVD-based damage-sensitive feature and compare it with those calculated from the intact sample dataset. If the estimated feature value lies outside the threshold, the damage is detected and we move to the next stage for localization.

At the second stage, namely, the localization of damage, the only input is the data from harmonic vibration tests with the sinusoidal input on the same sample. The core part of this stage is to compute the crest K-factor from the data collected by the accelerometer at each of the different locations. The location where the computed crest K-factor value is above a threshold indicates the damaged region.

4.2.1 Proposed SVD-based features with linear swept waves

Besides dimension reduction, in the field of non-destructive evaluation (NDE), researchers have analyzed the datasets collected from ultra-sonic pitch-catch experiments on steel pipes and found that the projection values on one specific left singular vector is significantly different between an intact pipe and a pipe with simulated damage [99]. This direction is promising because SVD provides us different angles to observe the structure of the data compared to traditional decomposition methods, such as Fourier Transform, Wavelet Transform, which decompose the signal in to fixed periodic bases or mother wave bases. On the other hand, SVD decomposes the data based on the data samples themselves and offers more flexibility in monitoring different structures. For structural health monitoring, we are primarily interested in the internal damage that is highly correlated with the

health condition. However, there are several issues that need to be addressed in this regard. The order where the damage-indicating left singular vector occurs changes from one experiment to another. The difference is not significant enough to observe and sometimes it may not even exist. Therefore, we need more robust and stable damage-sensitive features. In particular, the monitoring of concrete, due to the complex heterogeneity, requires more reliable and stable damage-sensitive features.

To address these issues, we propose a damage-sensitive feature based on the energy of the signal reconstructed from the projections on the last several left singular vectors that are calculated from the data of intact samples. Researchers performed monitoring on pressurized pipe under operation and they found the correlation between the first several singular vectors and the experimental design and operational set-up [100]. The reasoning behind this damage-sensitive feature is that the first several left singular vectors reflect the information of some of the statistics of the signal (such as magnitudes, frequencies, bandwidth, etc.) and the general medium properties (material type) in which the signal travels, etc. On the other hand, the changes in the material (such as internal damage, cracking, etc.) dominate the latter left singular vectors. Therefore, the projections onto the last several singular vectors should reflect these types of changes. Thus, we use the projections onto the last several left singular vectors to reconstruct the signal and choose the energy (sum of the squared values) of the reconstructed signal as the damage-sensitive feature. Meanwhile, to enrich the content of the vibration signal, instead of a pure sinusoidal input, we employ a linear sweep.

Given the data collected from the experiments, after preprocessing, we place them in a matrix $X = [x_1, x_2, ``, x_n]$, where each x_i represents a column vector of vibration data collected in test number i. Then we perform singular value decomposition as described in Section 2.2, as $X = USV^T$. Since the columns of U form an orthonormal basis, we reconstruct the signal with the last several left singular vectors, from $k4ton4$, which can be done practically by setting the diagonal values of S to be zeros from 1 to $k-1$, to get S^*.

The reconstructed signals are calculated as

$$X^* = [x_1^*, x_2^*, ..., x_n^*] = US^*V^T \tag{4.1}$$

Each x_i^* is a reconstructed signal using one of the last several left singular vectors as set above. Next, the proposed damage-sensitive feature is calculated using the

$$E_i = \sum_{j=1}^{n} {x_{i,j}^*}^2 \tag{4.2}$$

where E_i represents the energy of the reconstructed signal x_i^*, and $x_(i,j)^*$ represents the value of the reconstructed signal at time step j. With the calculated damage-sensitive feature values from the intact condition and later conditions, we can perform damage detection by setting a threshold based on the feature values from the intact condition. In real-world applications, we can also build a time-series model of degradation by performing continuous monitoring of the structure.

4.2.2 Selection of singular vectors

In this section, we first discuss the reasons for the selection of the singular vectors to reconstruct the signal to compute the damage-sensitive feature. Then, we discuss the robustness of the proposed approach. To illustrate the robustness of selecting singular vectors, we will follow the section with a comparison of the results of using different combinations of singular vectors to reconstruct the signal.

As mentioned in the previous section, each of the newly collected signals is projected onto the intact bases and the signal is reconstructed with the latter several signal vectors. In the experiments discussed in Section 4.2.3, we used the 21^{st} to 50^{th} singular vectors to reconstruct the signal. During this process, we neglected the first twenty singular vectors due to the assumption that these first several singular vectors represent the basic information of the tests such as the material types, experiments setup, etc. And the basic information

should remain the same if we test on the same material (concrete) and use the same type of experiment. Meanwhile, we also removed the very last few singular vectors, in order to remove the noise in the signal. The selection of the singular vectors was based on trial and error. And the selection criterion could be quantified by the variance explained by the selected singular vectors. We found that removing the first several singular vectors that explained 50% of the variance and the last few vectors that explained 5% of the variance would be a reasonable and effective selection.

The selection of the singular vectors to reconstruct the signal is found to be quite robust to minor changes in terms of the singular vectors included. To better demonstrate this argument, we performed reconstructions of the signal with multiple different selections of the singular vectors around the 21^{st} to 50^{th} singular vectors. Based on the singular value decomposition results of the intact dataset, the first 20 singular vectors explain about 50% of the signal variance and the singular vectors after 50^{th} represent about 5% of the signal variance. As described previously, we drop out these singular vectors and reconstruct the signal with the remaining ones. To demonstrate the robustness of feature values, we changed the starting and ending singular vectors and calculated the proposed damage-sensitive feature values with different selections of singular vectors. We presented the results with six different singular vector selections in Figure 4.1. The x-axis describes the test numbers and the y-axis describes the value of the proposed damage-sensitive feature. In all six cases, three sets of points are shown. The blue plus signs represent the damage-sensitive feature values from the intact dataset that we used to create the intact basis. The red plus signs represent the damage-sensitive features from the damaged dataset. And the blue circles represent the intact dataset reserved for validation.

The results of finer changes in combinations are summarized in a table. We varied the starting and ending singular vector by a range of -5 to 5, so we had 11 choices for starting singular vector and 11 choices for ending singular vectors. Therefore, we have 121 singular vector selection candidates overall. To quantify evaluate the performance of

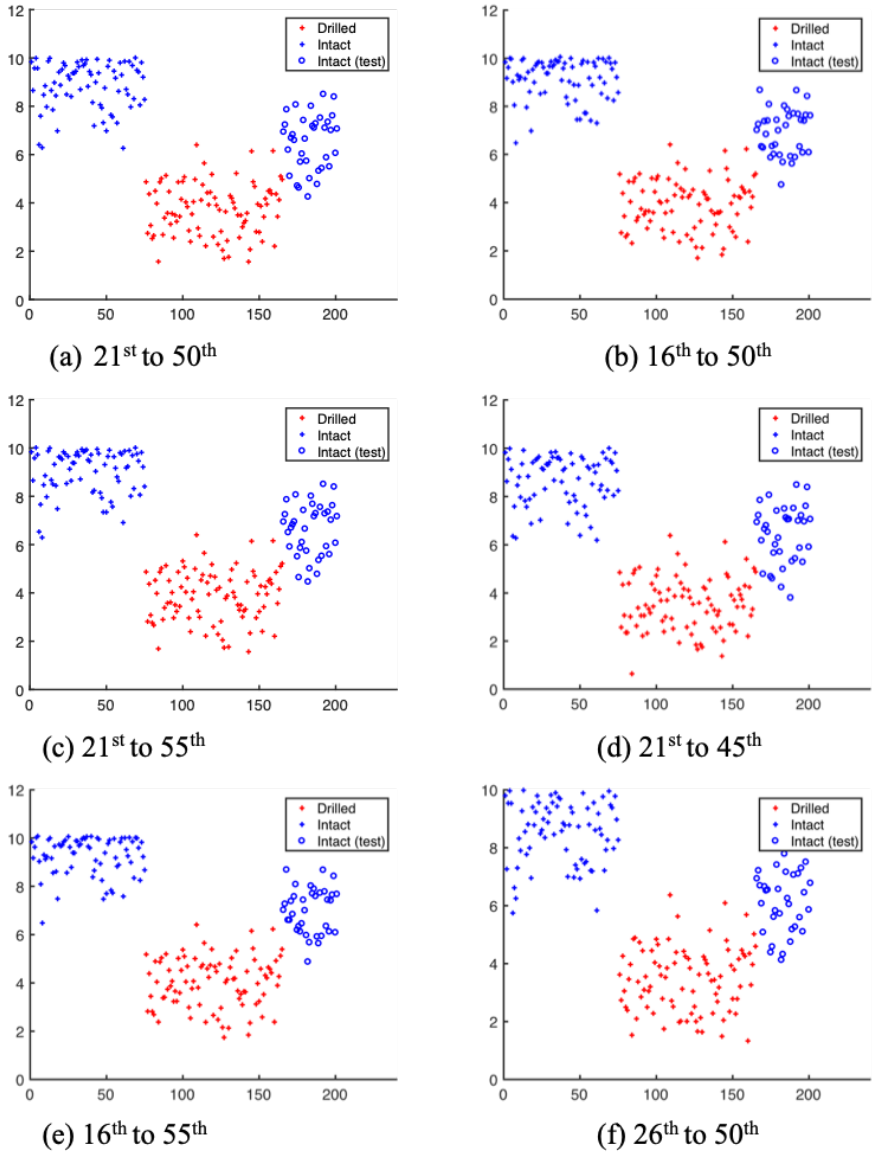

Figure 4.1: SVD-based feature values with different singular vector selections for signal reconstruction (x-axis: dataset number; y-axis: SVD-based feature value)

each of the combinations, for each singular vector selection, we trained a Support Vector Machine classifier with two kernels: RBF Gaussian kernel and polynomial kernel. We performed 10-fold cross-validation of the SVM classifier 10 times and gathered the error rates . (Note however, that the SVM analysis is only for evaluating the performance of the selected singular vectors, and is not actually used in damage detection). With the RBF-

kernel, 118 out of 121 singular vector (SV) combination candidates reached the accuracy of over 90% and only 3 out of 121 combination selections had an accuracy rate slightly less than 90%. And for the polynomial-kernel case, all 121 singular vector combinations reached over 90% accuracy and more than 60% of them reached an accuracy over 92.5%. Table 4.1 lists the SVM classifier results for each sensor location during one test. It is then seen that the results were not affected by minor changes in the singular vector selection. In other words, the damage-sensitive feature is quite robust to the singular vector selection. (In many SHM studies, statistical hypothesis testing is often employed for damage detection [47, 101]. In the case of Figure 4.1, the separation between the intact and damaged cases is quite distinct, thus hypothesis testing does not seem necessary; however, hypothesis testing could be employed if overlap is seen among the two sets of values, to check whether the overlap is significant).

Sensor Location	$0 \sim 2.5\%$	$2.5\% \sim 5\%$	$5\% \sim 7.5\%$	$7.5\% \sim 10\%$	$10\% \sim 12.5\%$	$12.5\% \sim 15\%$	$15\% \sim 20\%$
1	0	0	12	104	5	0	0
2	0	0	25	96	0	0	0
3	0	0	0	0	50	45	26
4	0	0	0	11	106	4	0
5	0	2	93	26	0	0	0
6	0	0	0	0	119	2	0
7	0	0	8	104	9	0	0
8	0	0	56	65	0	0	0
9	0	0	83	38	0	0	0

Table 4.1: Number of SV selection at different error at each sensor location

4.2.3 K-factor as an indicator for damage localization

The proposed SVD-based damage-sensitive feature is able to differentiate the data collected on damaged samples from the data collected on intact samples, as shown in the numerical study later. The next step is to identify the location of the damage by using the data from multiple sensors.

The assumption here is that the internal damage or crack will cause discontinuity in the material, especially for acoustic wave transmission. Therefore, if we set the waveform at the actuator to be a sinusoid, the acquired signals at accelerometers mounted at differ-

ent locations will be differently affected by the damage and deviate from the sinusoid at different levels. The amount of deviation will be affected by the location of the accelerometer, with the highest deviation observed when the accelerometer is mounted closest to the region where damage is present. As we acquire time series data from the accelerometers at different locations, we calculate the corresponding K-factor for each of the locations. Thereafter, by comparing the relative values of the K-factors, we will be able to identify the possible locations of the damaged zones.

For each of the sinusoidal input vibration tests, x_i, the K-factor can be calculated as

$$K_i = max(x_i) \times RMS(x_i) \tag{4.3}$$

After the calculation of the K-factors from the data collected by the accelerometers at each location, damage localization can be performed by comparing the K values. There are several possible methods to determine the damage locations, such as direct observation, maximum-value position, and use of unsupervised learning algorithms. In this study, we choose two methods ($k = 2$), direct observation and k-means clustering (an unsupervised learning method) for the sake of illustration. Other metrics might be found suitable for different applications.

4.2.4 Implementation of the proposed methodology

Using the proposed SVD-based damage-sensitive feature and the crest K-factor metric, we establish a procedure for damage detection and localization as shown in Figure 4.2. Two types of vibration datasets are needed: swept-input and sinusoidal input. Suppose $X = x_1, x_2, x_3, ‘‘, x_n$ represents the dataset from n swept-wave vibration tests where x_i represents the acquired signal from the ith test, and $Y = y_1, y_2, y_3, ‘‘, y_m$ represents the dataset from m sinusoid-wave vibration tests where y_j represents the acquired signal from the j^{th} test. Note that the swept-wave vibration experiments are performed on all the samples (i.e., both

intact samples and damaged samples in this study; in practical application, they will be time series datasets collected from the same structure at different dates based on the monitoring schedule, with the early stage treated as intact or initial condition.). On the other hand, the sinusoid vibration tests are performed only on the damaged sample. When monitoring an actual structure, the sinusoid tests may be performed only after the SVD-based damage-sensitive feature indicates the presence of damage, thus resulting in some cost savings.

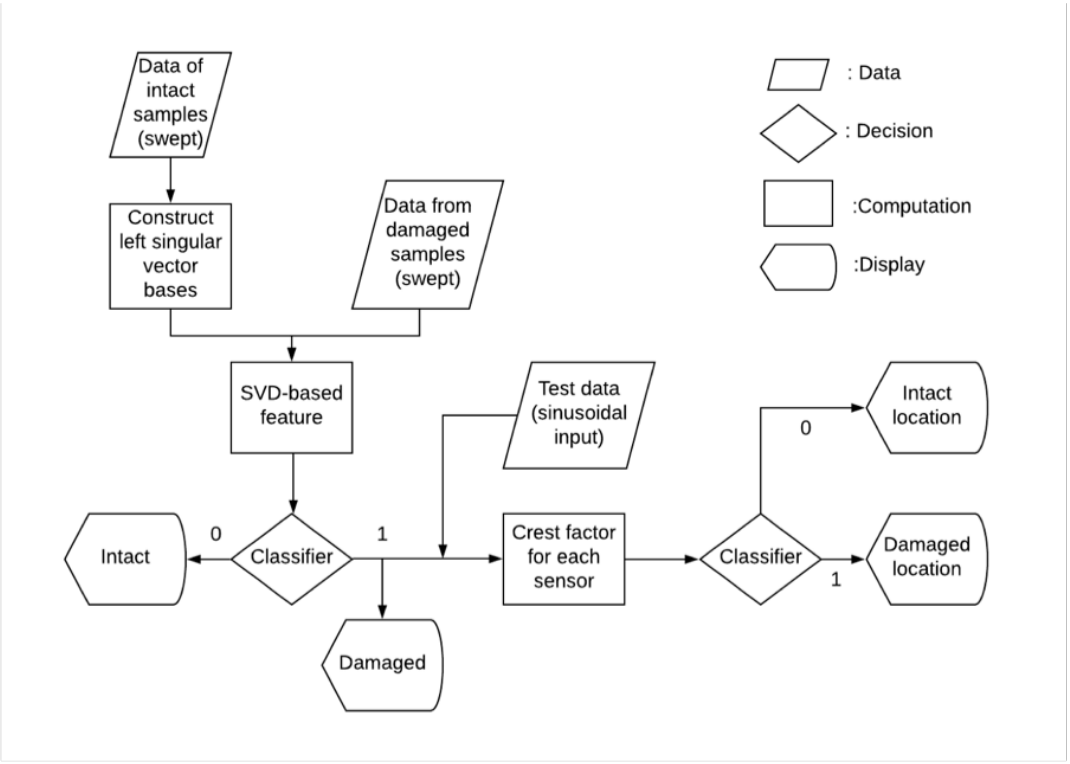

Figure 4.2: Flowchart of the proposed health monitoring framework

Suppose X_0 is the dataset from the intact/initial case, and $X_1, X_2, X_3 \ldots$ are the subsequent datasets. We first establish the singular vector bases using the dataset X_0 as

$$X_0 = U_0 S_0 V_0^T \tag{4.4}$$

For a subsequent dataset X_i $(i > 0)$, the projection of this dataset on the established singular vector bases will be

$$S_i = U_0^T X_i V_0 \tag{4.5}$$

Next, we reconstruct the signal with the last several singular vectors. This can be done by setting the first several projection coefficients to be zero to get S_i'. The reconstructed signal is

$$X_i' = [x_{i1}', x_{i2}', ...] = U_0 S_i' V_0^T \tag{4.6}$$

where x_{ij}' represents the j^{th} reconstructed signal from the i^{th} dataset. Then the proposed SVD-based damage-sensitive feature is computed as

$$E_{ij}' = {x_{ij}'}^T x_{ij}' \tag{4.7}$$

After the calculation of the feature values for all the collected datasets, we obtain the time series of the feature values starting from the intact/initial condition, and infer damage detection based on the selected threshold value of the feature.

During health monitoring over a lifetime of a structure, one issue needs to be considered is that, as we collect an increasing number of datasets, how to maintain the singular vector bases. Several options may be considered. The first one is not to update but continue to use the original bases. The benefit of this strategy is that we always compare the current condition against the initial condition. But the bases need to be updated once there is major maintenance or repair on the structure.

The second option is to update the singular vector bases every time we acquire a new dataset and establish the bases based on all the collected datasets up to this time. The benefit of this plan is that it can include the data over a long time-span. But this will increase the data storage expense and the computational load as we collect more and more datasets. The third option is also to update the bases once we have a new dataset but, instead of saving and using all the collected datasets, we save and use only the n most recent datasets

to create the singular vector bases. This option implies a Markov-type assumption (i.e., the singular vector bases are only affected by recent history) and reduces the storage and computation expense.

Once we detect damage in the structure, we enter the second stage of the health monitoring methodology by starting the data acquisition with the sinusoidal input vibration tests. In this stage, the K-factor calculation is relatively simpler compared with the SVD-based damage-sensitive feature calculation. Using the K-factor, we identify the most probable damage location(s) by direct observation, k-means clustering, or some other criterion; although different criterion can be used, the essential step is the calculation of the K-factor. As the grid for the accelerometers becomes finer (i.e. more accelerometer locations), the damage localization becomes more refined. The next section presents experiments with concrete samples with two different types of damage, and illustrates the proposed methodology.

4.3 Illustrative Example

To demonstrate and verify the proposed method, we conducted experiments on concrete samples with different sizes and different kinds of damage. Two types of samples were used for the experiments: patio block (thin slab) samples and thick block samples. Both types of samples were made of plain concrete.

4.3.1 Harmonic vibration experiments on patio block (thin slab) samples

The patio block samples were made of concrete and purchased from the hardware store. The dimensions of the patio block are shown in the Figure 4.4. A few of the slabs are preserved as intact samples; in other samples, to simulate internal damage, we drilled holes on one side of the block. The detailed locations and dimensions of the drilled holes are also shown in the Figure 4.4.

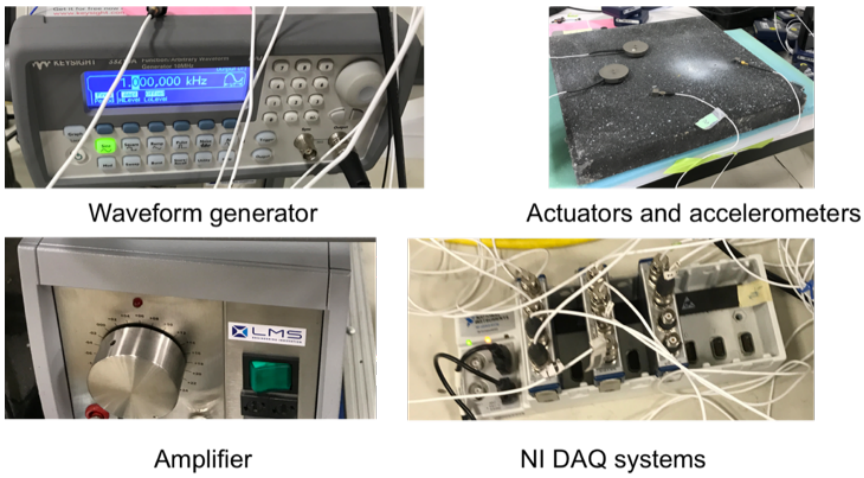

Figure 4.3: Testing equipment used in the experiment

The Harmonic vibration tests employed a waveform generator, a wave amplifier, a National Instruments data acquisition (NI-DAQ) system, an actuator, and nine single-axis accelerometers as shown in the Figure 4.3. The waveform generator was used to tune the parameters of the waveform. The actuator and the nine accelerometers were mounted on the top surface of the sample at the locations shown in the Figure 4.4 and 4.5.

The experiments used sinusoidal waveforms at $5000Hz$ and a sweep waveform (linearly swept from $200Hz$ to $5000Hz$). The frequencies were chosen based on the lowest effective frequency of the actuator and the highest sampling frequency in the NI-DAQ system. Due to the limitation of the accelerometer range, the amplitude of the waveform was constantly set to be $1000mV$ for all the tests. In each vibration test, the signal of a specific waveform (one of the aforementioned waveforms) generated by the actuator was received by the nine accelerometers at different locations, and each test lasted for $1.5seconds$. Overall, 100 tests were carried out with each of the waveform settings for both the intact sample and the damaged sample.

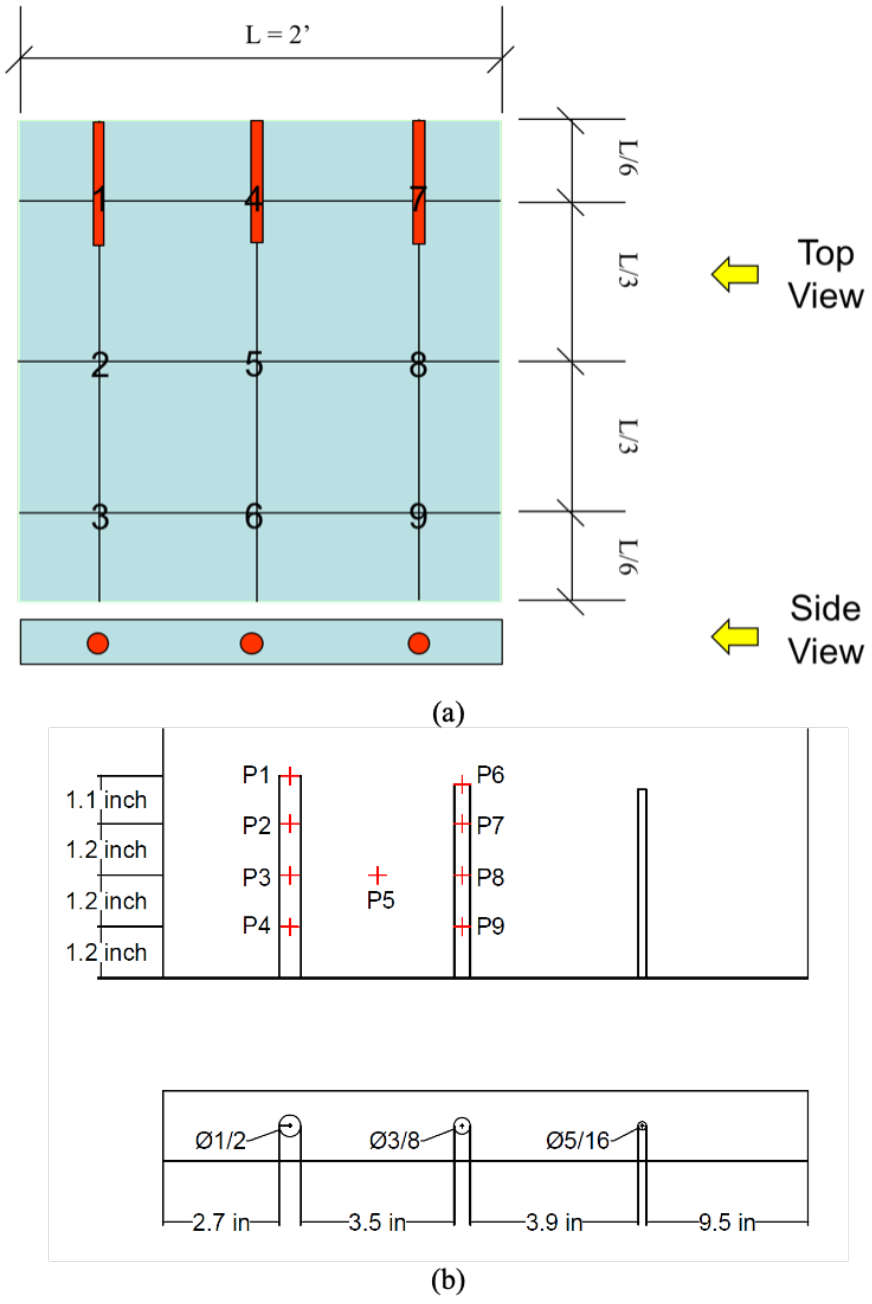

Figure 4.4: Dimensions and locations of the sensors (a) and drilled holes (b) in the patio block sample

4.3.2 Data Analysis

The data from the intact slab was divided into two subsets, 70% for damage detection and 30% for validation. SVD was performed on the former subset to establish the damage-

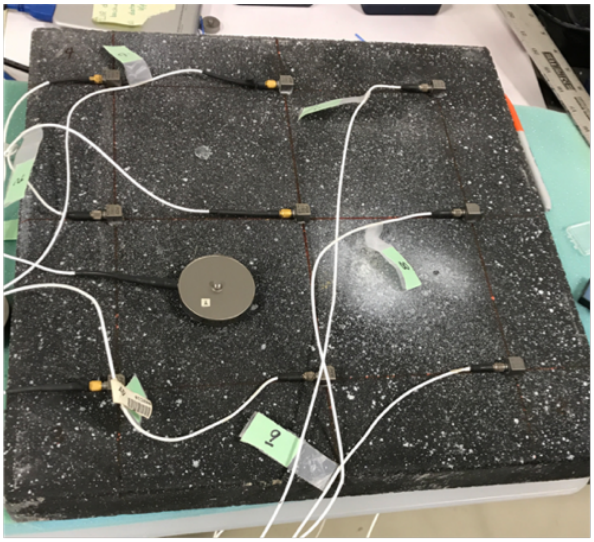

Figure 4.5: Thin slab sample with accelerometers mounted on the top surface

sensitive basis using the singular values. The data points collected from the damaged sample were not used to construct the intact condition basis. Since the feature values for the test set were calculated based on the projection to the bases calculated by the training data, it is expected that there is a little different for the two sets.

After the construction of the intact condition basis, each of the data points from both the intact and the damaged samples was projected onto the intact condition basis. We used the 21^{st} to the 50^{th} singular values to reconstruct the signal and calculate the energy of the reconstructed signal – the proposed damage-sensitive feature. In Figure 4.6, the blue points represent the values of the damage-sensitive features from the intact data, and the red points represent the values of the damage-sensitive features from the damaged sample. The blue circles represent the values of the damage-sensitive features from the intact dataset set aside for validation. The x-axis shows the dataset number, and the y-axis shows the energy value. Same as the shown in Figure 4.1, the blue plus signs indicate the damage-sensitive feature values from the intact dataset that we used to create the intact basis. The red plus signs indicate the damage-sensitive features from the damaged dataset. And the blue circles show the intact dataset reserved for validation. The plots indicate that the energy values from

the damaged cases were much lower than those from the intact samples. The results are consistent for each of the 9 sensors, showing significant difference between the feature values from the intact samples and those from the damaged samples, thus making the damage detection very effective.

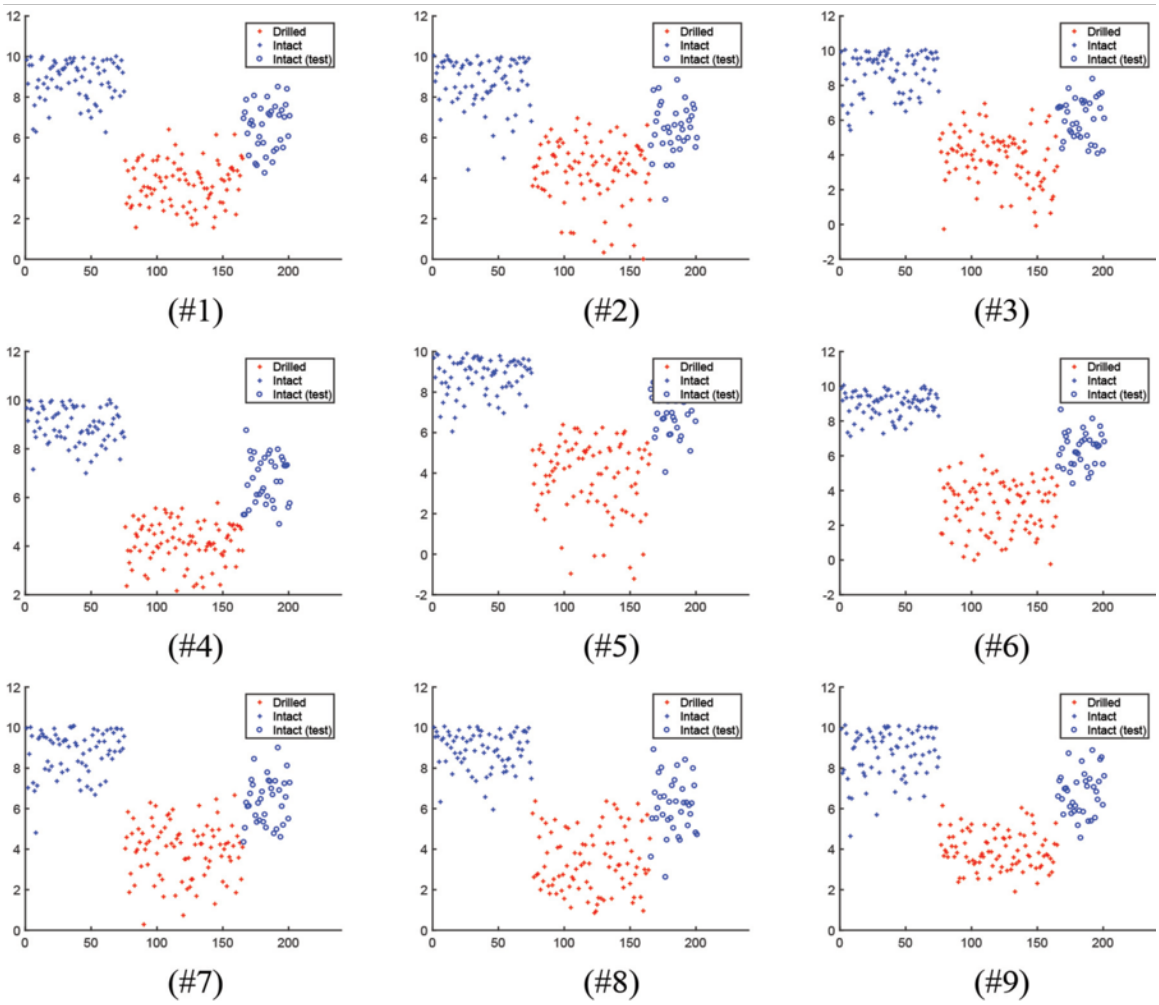

Figure 4.6: SVD-based features from patio block samples (x-axis: dataset number; y-axis: SVD-based feature value

Next, we use the data from tests with the pure sinusoid waveform (here we used a frequency of $5kHz$) for damage localization analysis. Since there are 100 tests, 100 K-factors are calculated at each of the 9 locations and plotted in Figure 4.7. From the plot, we observe that the values of K-factor at locations No.1, No.4, and No.7 are much higher than those at the other locations. Therefore, these three locations are identified to have

a high probability of damage. This result matches with the design of the sample, since accelerometers No.1, No.4, and No.7 were mounted above the drilled holes.

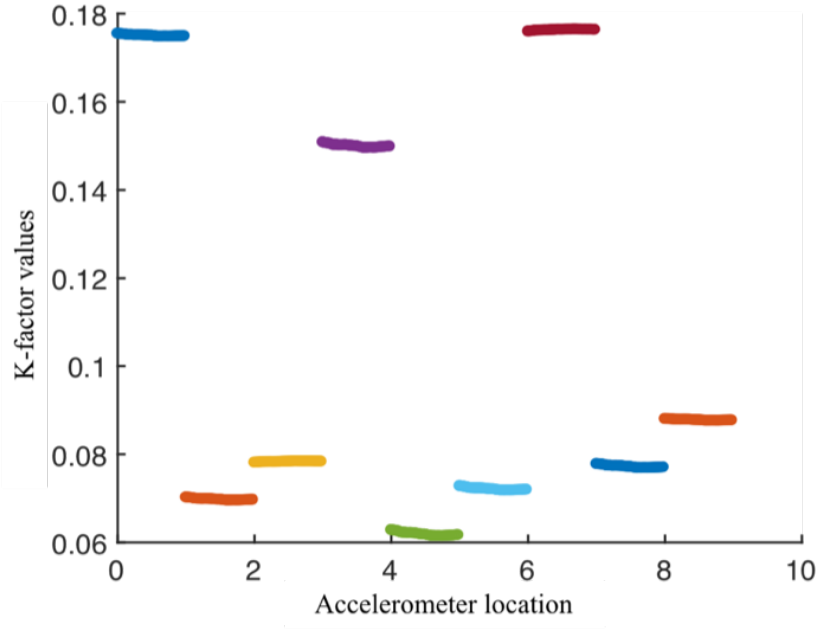

Figure 4.7: *K*-factor calculation from the drilled patio block sample

For the patio block sample, we know the ground truth and could make the diagnosis directly by visual observation. However, for the next studied sample, which is conducted with much larger and thicker samples, the damage is not visible, and the damage locations are unknown.

4.3.3 Harmonic vibration Experiments on the Thick Block Samples

These samples were made at the University of Alabama, and were utilized to simulate damage due to alkali-silica reaction, a type of damage seen in concrete structures such as dams. Some types of aggregates chemically react with the cement to form an alkali-silica gel, which continues to grow in the presence of moisture and eventually causes cracking. The samples contained two kinds of reactive aggregates, from North Carolina and Colorado. For each type of aggregate, the concrete samples were prepared by adding chemi-

cals to either boost the reactivity (referred to as reactive samples), or suppress the reactivity (referred to as control samples). The reactive samples were cured in alkaline solution to further accelerate the alkali-silica reaction. In the following discussion, we will refer to the samples as AR, AC, BR and BC, where A and B refer to the sources of the aggregates (North Carolina and Colorado), and R and C refer to reactive and control samples respectively. These samples were cured in alkali and humid condition for over a year. The presence of alkali-silica reaction (ASR) was first detected using deformation measurements (i.e., expansion of the AR and BR blocks).

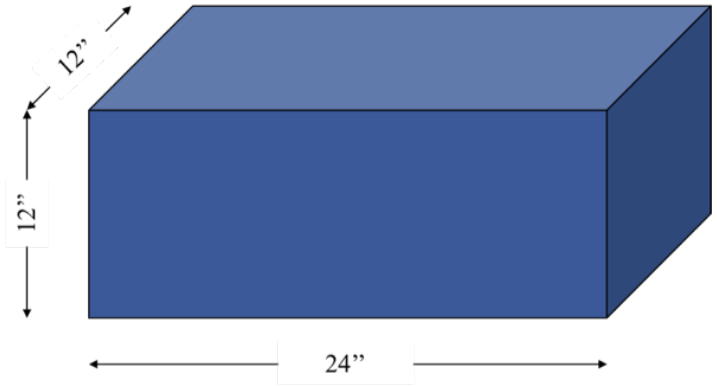

Figure 4.8: Dimensions of the block samples

The locations of the accelerometers and the actuator for the vibration tests are shown in Figure 4.9. For the sake of illustration, we concentrate the placements of the accelerometers on one half of the sample. The parameter settings of the waveforms were maintained the same as in the case of the thin patio slabs, including the frequencies and the magnitudes. Then, 100 tests for each of the specific settings, each with 1.5 seconds duration, were conducted.

Similar to the thin slab case, the datasets of the control samples were divided into two subsets, 70% for damage-sensitive basis construction and 30% for validation. Then, all the data points were projected on the created basis, and the damage-sensitive feature (energy) was computed based on the reconstructed the signal with the 21^{st} to 50^{th} singular values.

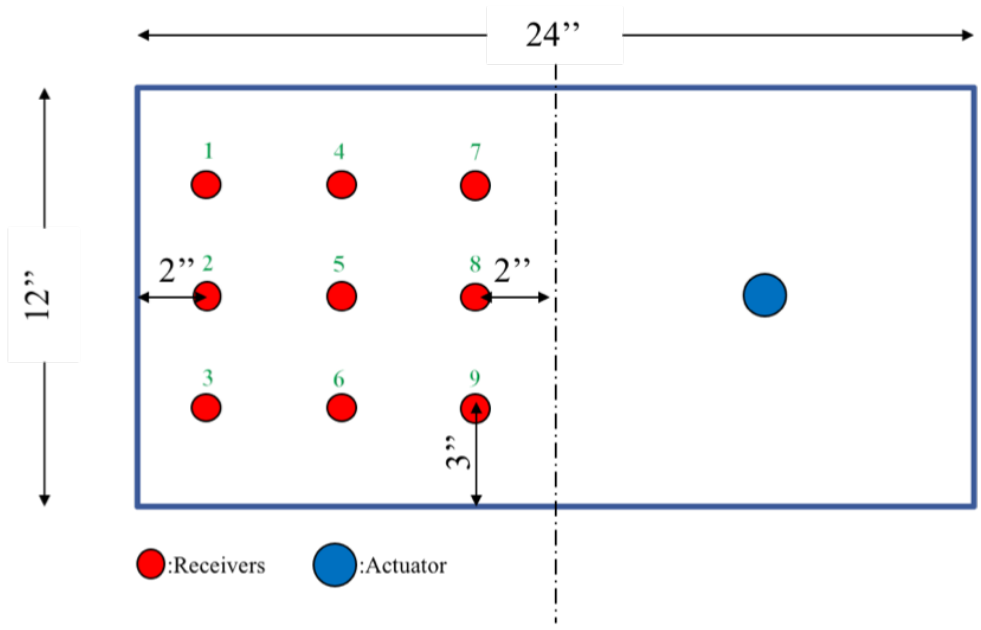

Figure 4.9: Locations of the accelerometers and the waveform actuators

The results are shown in Figures 4.10 and 4.11. As before, the blue plus signs represent the feature values for the 70% control samples, the red plus sings represent the values for the reactive samples, and the blue circles represent the values for the 30% control validation samples. It can be observed that the feature values for the reactive samples were much lower than those for the control samples. Meanwhile, the differences were significant enough to make the damage detection quite clear.

Similar to the process for the patio block samples, sinusoidal vibration test data on the reactive samples are used next, to compute the K-factors at each of the accelerometer locations. The assumption in using the K-factor is that higher values of the K-factors indicate more damage under that specific accelerometer. Since this process was a relative comparison, there could be multiple different metrics to make decisions. Here we illustrate two metrics: direct observation and k-means clustering.

The results from direct observation are shown in Figures 4.12 and 4.13. For the AR sample, it is seen that the values of the K-factors from accelerometer No.2, No.3, No.5, and No.6 were much higher than the other accelerometers. Therefore, we could identify

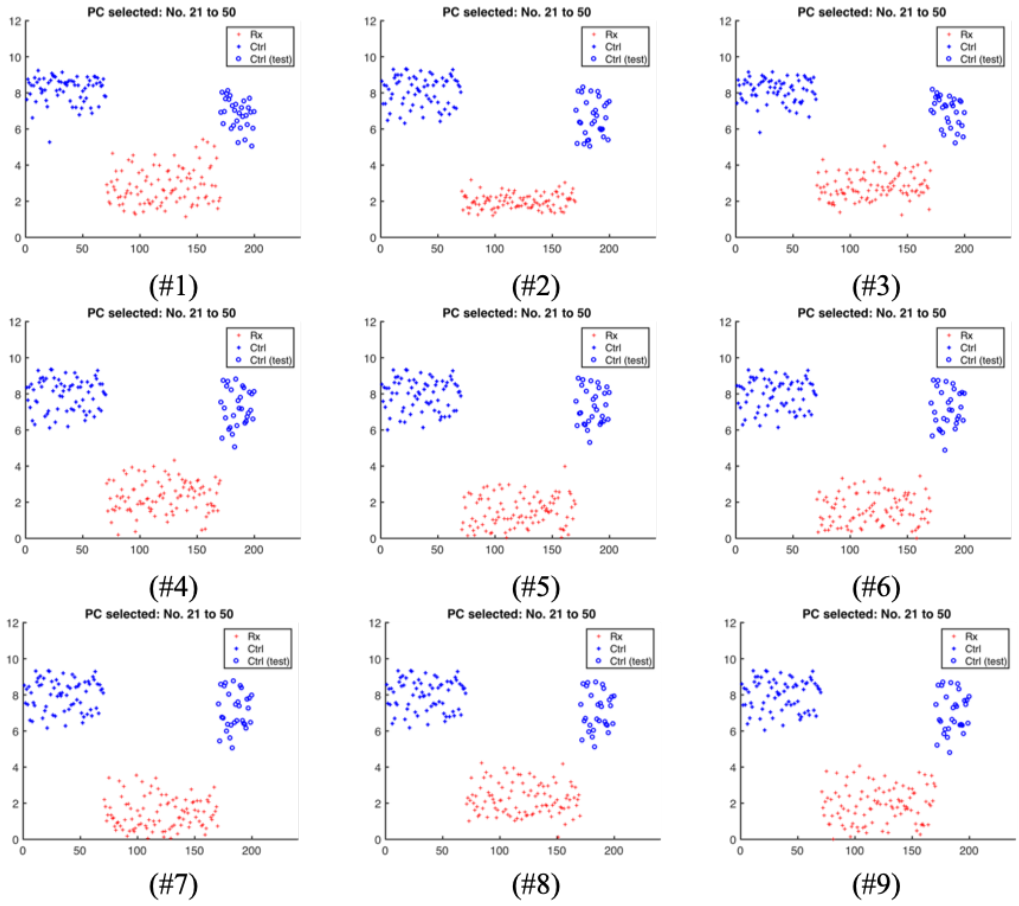

Figure 4.10: SVD-based features of North Carolina samples (x-axis: dataset number; y-axis: SVD-based feature value)

locations No.2, No.3, No.5, and No.6 as more likely to be damaged than the other locations. For the BR sample, the K-factors from accelerometer No.6 were much higher than at other locations, implying a higher probability of damage in the zone close to location No.6. (Hypothesis testing is not necessary to distinguish between the K-factor values since they are remarkably consistent at each location, with negligible variance).

As an alternative to direct observation, we could also use an unsupervised learning method to cluster the values of the K-factors. Here we use k-means clustering to group the candidate locations based on their damage condition, and set the number of clusters to be two. (Note that we could set the number of clusters to be greater than two, thus offering more flexibility in identifying and locating multiple levels of damage severity). After a

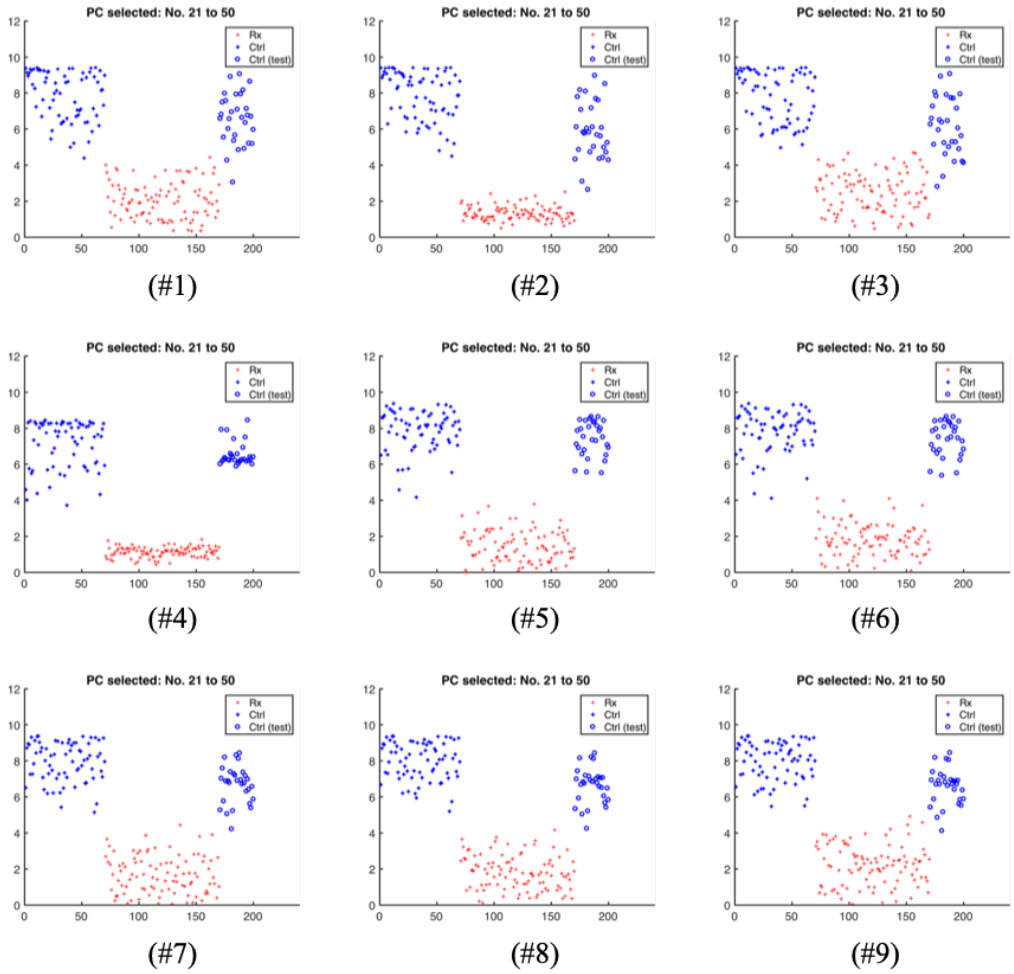

Figure 4.11: SVD-based features of Colorado samples (x-axis: dataset number; y-axis: SVD-based feature value)

hundred iterations of K-means clustering, the clustered groups reached a stable result. The results are shown in Figures 4.14 and 4.15. The red points indicate the ‘‘damage‘‘ cluster, and the blue points indicate the ‘‘intact‘‘ cluster. For the AR sample, the results from direct observation and the results from k-means clustering ($k = 2$) match with each other. For the BR sample, the results using k-means clustering ($k = 2$) are more conservative than the results from direct observations, since more locations are identified as damaged. When we apply this method to a relatively large structure, we should expect damage of different kinds and severity, and adjust the number of the clusters accordingly.

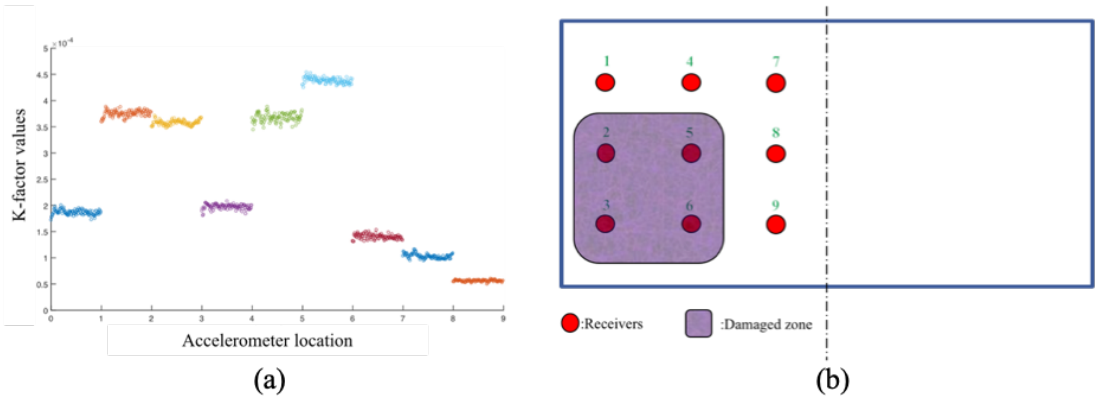

Figure 4.12: *K*-factors for AR samples: (a) direct observation; (b) possible damaged zone

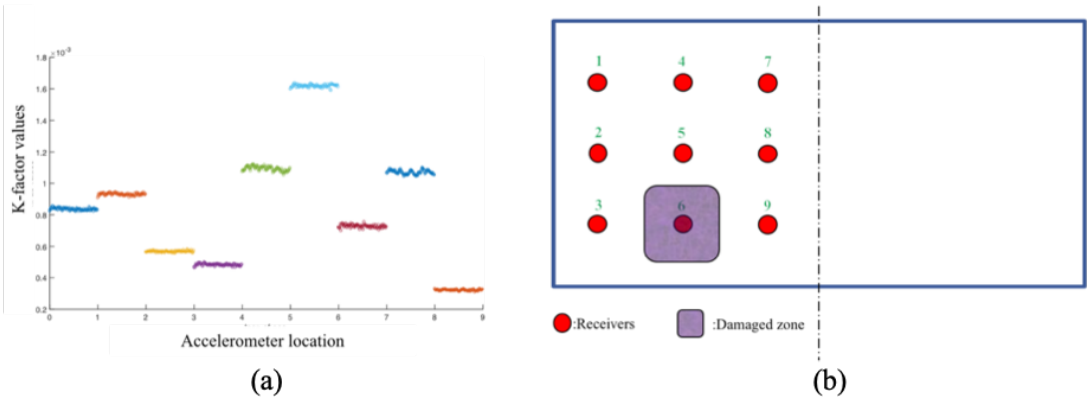

Figure 4.13: *K*-factors for BR samples: (a) direct observation; (b) possible damaged zone

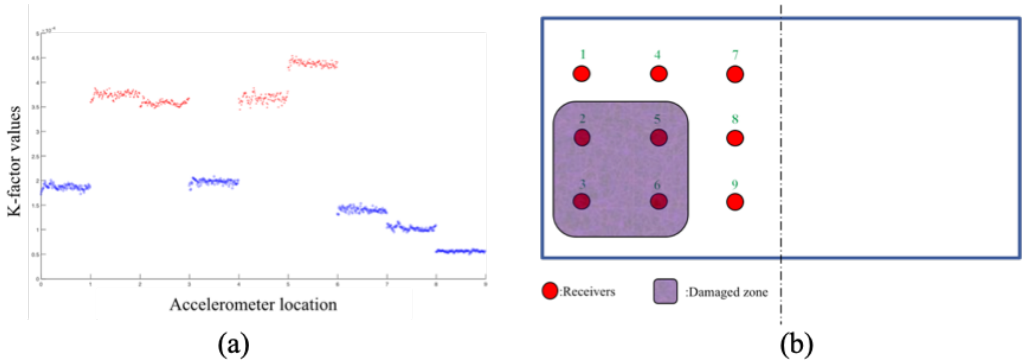

Figure 4.14: AR sample *K*-factors: (a)*k*-means clustering; (b) possible damaged zone

4.3.4 Robustness study about location-choice of the actuator

For the harmonic vibration test, there are many possible locations where a researcher can place the actuator on a sample. Especially, we want to study whether the relative

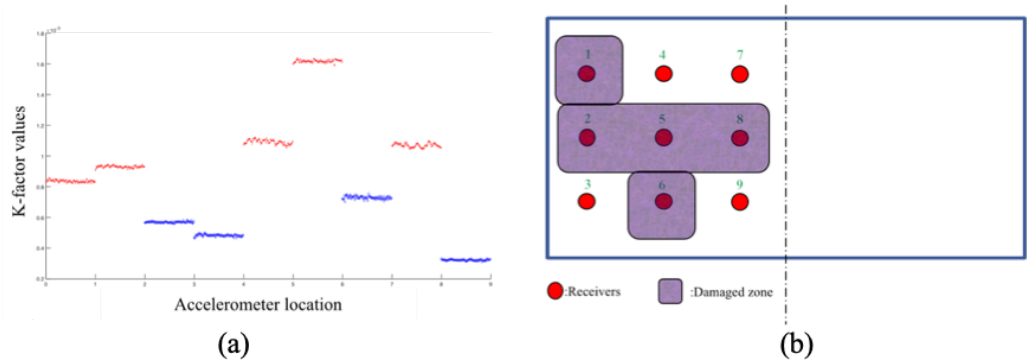

Figure 4.15: BR sample K-factors: (a)k-means clustering; (b) possible damaged zone

distances from the actuator to the nine accelerometers will affect the calculation of the crest factors, which may affect the prediction of the damaged area. Therefore, we draw a grid on the top surface of the sample and select the locations of the actuator based on the grid. Here in the Figure 4.16 is the grid we draw on the Alabama sample with 18 selected locations for the actuator placement.

For each of the scenarios, we carry out 100 harmonic vibration tests and acquire responses from 9 accelerometers. Then we calculate the corresponding crest factor for each location. With the calculated crest factors for each of the scenarios, we can perform damage localization with hard-max direct observation (locations with the maximum crest factor values) and the k-means clustering algorithm. The predicted damage locations are listed in the following Table 4.2.

If we use a voting mechanism, we can further identify the damaged area based on the location(s) with the most votes. The following two tables, Table 4.3 and 4.4, summarized the votes for each location.

4.4 Conclusion

In this chapter, we developed a novel two-stage methodology for damage detection and localization using vibration tests. For the purpose of damage detection, we proposed an SVD-based damage-sensitive feature using swept waves. For damage localization, we

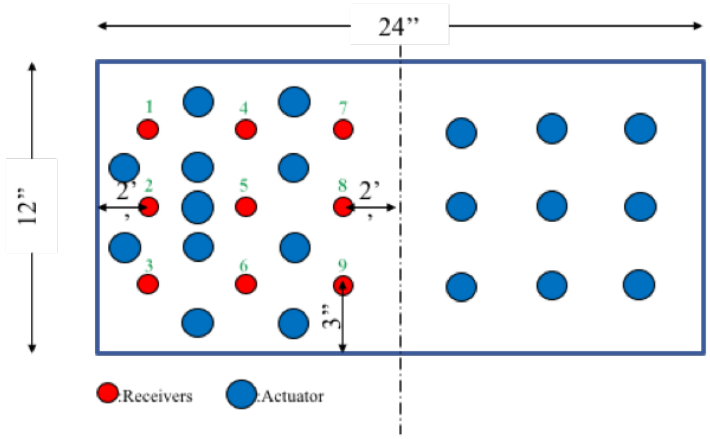

Figure 4.16: Locations candidates of the actuator placement

Scenarios	Hard-Max	*k*-mean
1	6	1,2,5,6,8
2	2, 5	2, 5
3	8	2, 4 5, 7, 8
4	8	2, 5, 7, 8
5	8,	8, 9
6	2, 6	1, 2, 5, 6, 8
7	8	1, 2, 5, 6, 7, 8
8	6	2, 5, 6
9	2	2, 5, 6
10	2	2, 5
11	6	6
12	6	6, 8
13	3, 5	3, 5
14	2	2, 5
15	2	2, 5
16	2, 5	2, 4, 5, 8
17	2	2
18	2	2, 5
19	3	3
20	2	2, 4, 5, 6

Table 4.2: Prediction results from each scenario

introduced the K-factor metric using sinusoidal waves.

The proposed methodology is demonstrated using experiments on two types of concrete

Acc #	**2**	3	5	6	8
Votes	**10**	2	3	5	4

Table 4.3: Votes for damaged locations with hard-maximum

Acc #	1	**2**	3	4	**5**	6	7	8	9
Votes	3	**15**	2	3	15	8	3	8	1

Table 4.4: Votes for damaged locations with k-means clustering

samples ‘‘ thin slabs with drilled holes and thicker blocks with internal ASR damage. In both cases, the SVD-based damage-sensitive feature was effective in differentiating damaged samples from intact samples. (There is some variance in the damage-sensitive feature values from test to test, but there is still clear separation between the intact and the damaged datasets for all the specimens). And the values of the K-factors were able to provide insights for damage localization. For the patio blocks, other conventional methods can also detect the holes; however, the advantage of the proposed approach becomes clearer in the thicker concrete blocks, where the performance of the proposed SVD-based feature values is much better than its performance on patio blocks, whereas the other methods have difficulty as specimen thickness increases.

Note that our method is equally applicable to homogeneous and heterogeneous materials, and there is no customizing of the method to particular cases of heterogeneous conditions. However, our illustrations using real laboratory experiments on patio concrete blocks and thick concrete blocks are all considering heterogeneous material. In all cases, we employ the same techniques for damage detection and localization.

It can been seen from the methodologies from Chapter 3 and this chapter that feature development takes a lot of trial-and-error effort and time-consuming. Therefore Chapter 5 explores using deep learning, by employing convolutional neural networks and the concept of transfer learning, which can save much effort and time in feature generations through its multi-resolution architecture, which can be treated as feature automation.

Chapter 5

Convolutional Neural Network for Interior Damage Diagnosis using Simulation and Experimental Data

5.1 Introduction

Visual inspection-based structural monitoring techniques continue to be the primary approaches for inspecting massive structures such as bridges and dams. During the past decade, computer vision-based techniques have been developed to overcome the limitations of close-distance inspection and variations in the inspector‘‘s experience and judgement. Computer-vision based structural health monitoring (SHM) techniques have dense information due to the high resolution (large number of pixels) in images. This provides an advantage over vibration-based techniques which are limited by the number of sensors and space available for sensor placement, and the dynamic effects introduced by sensor weights [102, 103, 104].

Most applications of traditional image processing techniques focus on testing their fitness to one specific structural damage mechanism. For example, some studies have used edge detection and sequential image filtering to perform crack detection on concrete bridges [105, 106, 107]. Some studies have used entropy-based image processing techniques to detect concrete spalling [108], and Hough transform and support vector machines to detect loose bolts and rust in steel bridges [109, 110, 111] . Other studies have used Gabor filter, textual pattern recognition, and Adaboost techniques to detect crack and other defects in pavements [112, 113, 114]. Researchers have also attempted to improve the efficiency and robustness of traditional vision-based SHM techniques with machine learning algorithms [110, 109]. Each of these methods have considered only for one type of damage (and mostly for homogeneous material), and require much effort in creating damage sensitive features [115, 116, 117, 118].

Deep learning techniques have shown unprecedented success in major image classification/object recognition and natural language understanding (NLU)/natural language processing (NLP). Some of the significant applications of deep learning methods in structural health monitoring include deep belief network models for failure detection and estimation in aircraft engines and power transformers [119, 120], and convolutional neural networks to perform detection and localization of surface cracks and rust [121, 122]. Also, some researchers used denoising autoencoders with multiple hidden layers to detect faults in bearings and other rotating machines [123, 124]. These studies have used deep learning techniques to enhance SHM with more complex, comprehensive models and automated the feature generation. However, as mentioned above, most of the applications are on homogeneous materials such as metal parts, or surface cracks in heterogenous materials such as concrete.

This chapter addresses the limitations in both traditional image processing techniques and current deep neural network techniques with respect to SHM. A damage diagnosis framework is proposed, which is capable of detecting internal damage in structures and also automating the feature generation process. The methodology is applied to images from thermography experiments, thus providing the capability for internal damage diagnosis.

The rest of the chapter is organized as follows. Section 5.2 presents the proposed damage diagnosis framework. Section 5.3 discusses the generation of a large volume of data using finite element computer simulations and real-world laboratory experiments. The details of the proposed deep convolutional neural network methodology for damage diagnosis are presented. We also discuss data preparation, model training, and model performance on simulated as well as real-world data sets. Section 5.4 presents the Bayesian inference of the deep convolutional neural network model using Monte Carlo simulations on Dropout models. Lastly, Section 5.5 provides a brief summary of contributions.

5.2 Proposed Methodology

As mentioned earlier, the proposed methodology aims to fill the research gap between the interior damage detection capability of traditional image processing techniques (such as line and edge detections, which are mostly based on the analyst‘‘s experience and judgement and specific descriptions of the features) and the surface damage detection capability reported thus far with deep neural networks. The proposed methodology also handles the problem of limited experimental datasets by augmenting it with finite element simulation data and taking advantage of transfer learning techniques. Even though the methodology is illustrated in this chapter for SHM of concrete (a heterogeneous material), the methodology itself is general and can be used in a wide range of applications, such as SHM of homogeneous materials with relatively small datasets.

The proposed methodology has two major steps. The first step is training data generation using finite element models to simulate the laboratory experiments of the same setup. And the second step is to take advantage of transfer learning using convolutional cores of a selected pre-trained neural network, which has been trained using a large dataset of many different types of images and has shown significant performance in computer vision tasks such as object detection.

5.2.1 Data generation from computer simulations and laboratory experiments

5.2.1.1 Data set from laboratory thermal tests

The training data generation consists of two parts, laboratory data and computer simulated data. The laboratory experiments should be designed based on the practical application conditions. For example, in the laboratory experiments illustrated in this chapter, a concrete specimen is placed on the top of a heating mat, which is programmed to provide a pre-designed heating profile. During the heating-cooling process, a thermal camera is placed on the other side of the specimen to record the temperature field information of

the specimen. The design of the heating-cooling profile should heat up / cool down the specimen as far away from room temperature as possible and as fast as possible to increase the contrast of the impact and damaged parts. On the thermal camera side, temporal sampling frequency of the camera is selected to balance the accuracy and the limitations of the hardware (thermal camera and data acquisition equipment). The relative positions of the concrete sample and the equipment can be found in [125], which has a very similar experimental setup. We seek to generate a large amount of data samples from computer simulations for training and testing the deep neural network model.

5.2.1.2 Data generation from computer simulations

For computer simulation-based data generation, the finite element models should be built to cover as many damage scenarios as possible. For instance, finite element models should cover various damage locations and damage geometries. The thermal conditions and data acquisitions in the computer simulation are based on the laboratory experiment or field condition. We would like the finite element model to closely represent the physical data collection condition as much as possible and cover as many different damage scenarios as possible.

The size of the data set plays an essential role in successful training of machine learning models. Large data sets contribute to the recent superior performance of deep neural networks over other traditional machine learning models. However, in SHM, the preparation and monitoring of thousands of actual concrete samples with various health conditions demands significant expense in finance, labor, and time. Therefore, we take advantage of computer simulations using finite element (FE) models built in the Abaqus software.

Using the Abaqus FE model, we simulate concrete samples with various damage locations and shapes by changing the model parameters. In the FE model, we design the dimension of the model to be the same as the physically monitored specimen/structure. The FE model needs material properties, such as density, thermal conductivities in intact condition

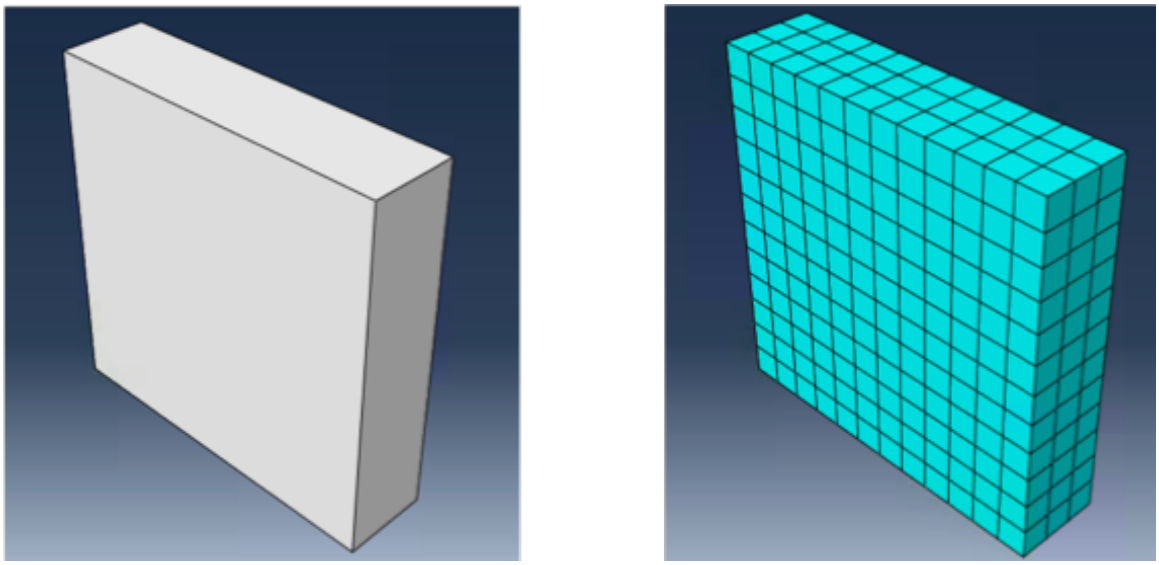

Figure 5.1: Finite element model in Abaqus

and of damaged condition, and specific heat capacity. These properties can be found in literature or through preliminary laboratory testing. The finite element model simulation follows the same thermal load profile (heating and cooling) as used for the thermography experiment in the laboratory.

Thousands of finite element model simulations to train the CNN can face significant computational expense. Therefore, it is critical to carefully choose the model parameters such that there is balance between computational expense and model accuracy. The candidate parameters are the number of CPUs, mesh size, and the duration of the time steps. The number of CPUs represents the computational power. The mesh size indicates the spatial resolution of the finite element model, specifically the number of elements along the z-dimension, i.e., along the thickness L_z. The duration of time steps is another issue that affects the FE model prediction. The metrics we use to decide the values of these parameters are CPU time and r-value. The r-value shown in equation 5.1 should be lower than 0.5 to fulfill the Courant-Friedrich-Lewy (CFL) requirement for a stable result in the finite element simulation [126].

$$r = \frac{\alpha \Delta_t}{\Delta_x^2} < 0.5 \tag{5.1}$$

, where

$$\alpha = \frac{K}{\rho C_p} \tag{5.2}$$

Here, Δ_t stands for the time step duration, Δ_x stands for the mesh size (same in all three dimensions), K stands for the material's thermal conductivity, ρ stands for density, and C_p stands for specific heat capacity. As shown in equation 5.2, given the material properties (density, specific heat capacity, and thermal conductivity), α should be a constant value. Therefore, we select different combinations of Δ_t and Δ_x, and track the corresponding CPU time and r-value. After a systematic parametric study, we build the computer simulated models with chosen optimal parameters and collect the results to form the training dataset for the damage diagnosis model.

5.2.2 Damage diagnosis based on convolutional neural network

The dataset from computer-simulated and laboratory experiments contains the internal health conditions of the structure. And the assumption is that the health condition of the structure will affect the thermal properties of the material. As mentioned earlier, with these dataset, traditional image processing based structural health monitoring techniques will spend much effort manually to develop damaged criteria based on features, such as gradients and edges. The proposed damage diagnosis framework uses convolutional neural network, which can be viewed as a type of multi-scale/multi-resolution analysis, to automate the feature generation process. This architecture decompose the original images into elementary features and, as the information pass through layers, these elementary features start to form various combinations to describe more complex image features, which previously require extremely complex calculation, such as Scale-invariant feature transformation (SIFT). Further, we use transfer learning to build the diagnosis model; i.e., a sophisticated

CNN model already trained on a large dataset containing millions of images is used as an initial model, and new layers are added to this initial model based on the training data to tailor it to the particular specimen considered for damage diagnosis.

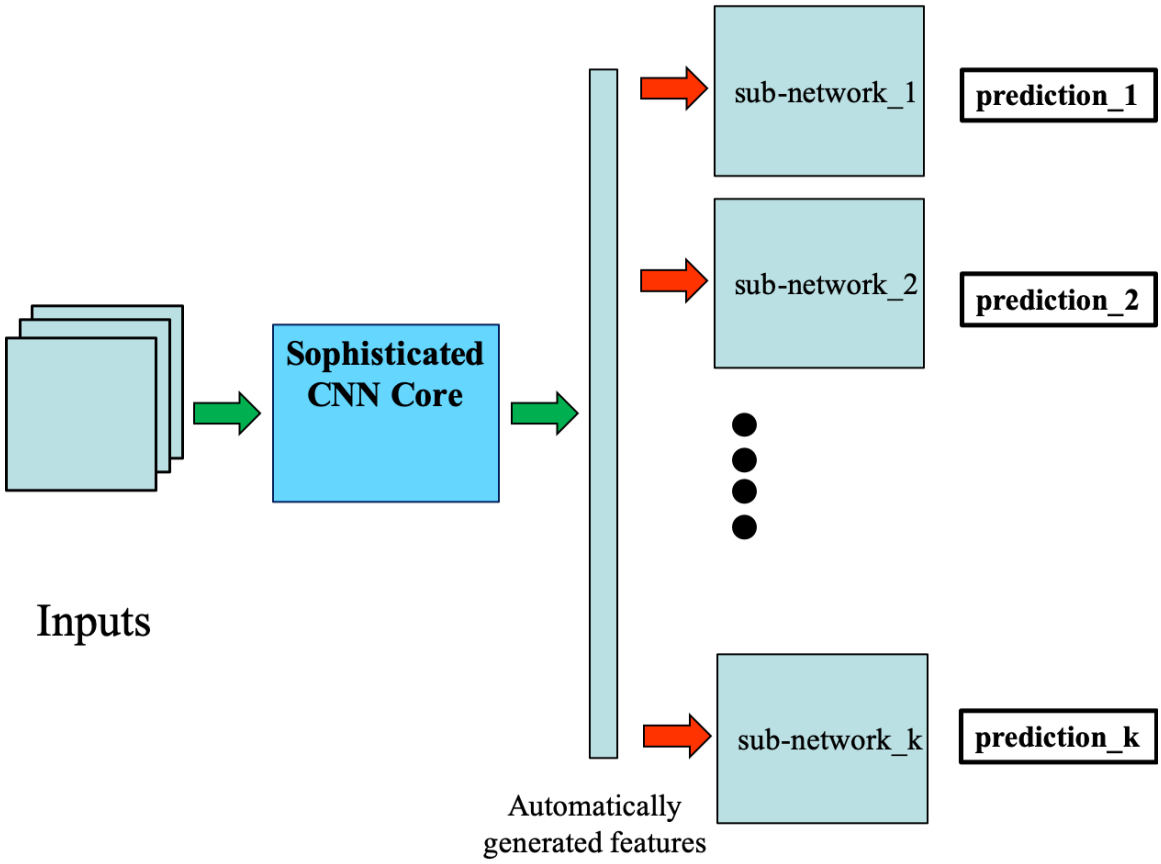

Figure 5.2: Proposed deep neural network architecture for damage diagnosis

To simplify the model and to reduce the computational cost, we set the model inputs to be the images obtained when the temperature changes the most, thus increasing the contrast between the intact and damaged areas. The work flow of the proposed methodology is shown in the Fig. 5.2. The first half of the model is the convolutional core of a pre-trained sophisticated deep CNN, trained on millions of samples with state-of-the-art performance on image processing and computer vision tasks. As the selected convolutional core has many layers with tens of millions of connections, it can be viewed as an automatic multi-scale analyzing process for generating and selecting valuable features. To connect the convolutional core, the second half of the model are sub-neural networks, each of which

focuses on a specific prediction, such as horizontal and vertical locations of the damage, and damage shape. Detailed information regarding the specific damage diagnosis model developed using this approach is provided in Section 5.2.

5.2.2.1 Deep neural network model

As described above, we use the pre-trained CNN core as the base and append additional fully connected layers to map the computed feature values and perform damage diagnosis for a specific specimen. The inputs are chosen to be the temperature field on the top surface of the structure of interest. And the outputs of the damage diagnosis framework are values of quantities related to the structural health condition, such as damage location, damage size and damage shape.

We demonstrate the damage diagnosis model development using VGG-19 as an example. VGG-19 has a deep neural network architecture, and has shown excellent performance in many image processing and computer vision tasks. The inputs of the original VGG-19 architecture are images in RGB format (three channels for the third dimension). Therefore, we set the inputs as three consecutive thermal images at a specific time, as thermal images in the thermography experiment are captured and stored as two-dimensional matrices with numerical values.

The dimension of the outputs from a chosen CNN core is usually very large, a vector with thousands of entries. This large vector is found to encapsulate the input images in various directions [127]. Therefore, building upon these feature values offers significant power in various computer vision assignments [128]. It also provides advantages in computational expense and storage cost [129, 130]. Meanwhile, these thousands of entries can be treated as a source of features, which are generated by the multi-scale multi-resolution architecture of deep convolutional neural networks. This automatic generation of features saves tedious manual feature tuning effort.

The quantities of interest (QOI‘‘s) in structural health monitoring can be multiple, and

the proposed damage diagnosis model is designed to be capable of adjusting to the desired QOI‘‘s. As shown in Fig. 5.2, the number of sub-networks is determined by the number of QOI‘‘s. Each of the sub-networks takes care of one specific prediction. For instance, the output of sub-network A can be damage shape, the output of another sub-network B can be the damage size, and so on. The performance of the model depends on how we address the following questions. Do we treat this as a regression problem or classification problem? How many categories for classification? How to select the inputs? How to encode the outputs? In the illustration in Section 5.3, one of the major issues is that, given the limitation of computational resources, the finite element model has a coarse mesh with limited resolution in the $x-y$ plane. This limits the choices of damage locations, and therefore the number of samples generated for the training data. As a result, a quantitative prediction model will have low accuracy.

One way to overcome this challenge is to treat the problem as a classification problem and to reduce the number of targets. For example, the image can be divided into a coarse grid. Instead of predicting the exact x and y coordinates (numerical values), we can predict the cells of the grid as targets (categorical values). We use one-hot encoding for the categorical values, which has been widely used in encoding categorical data [131, 132, 133]. The length of the encoded vector depends on the number of categories, and each of the elements in the vector corresponds to a specific category. For instance, if we want to encode four categories of damage: surface crack, internal crack, rust, and loose bolt, the corresponding one-hot encoding is shown in Table 5.1

Category	**Results of one-hot encoding**
surface crack	1000
internal crack	0100
rust	0010
loose bolt	0001

Table 5.1: An example of one-hot encoding

Next we discuss the selection of inputs. As described in Section 5.2.1.2, the training

data are a series of thermal images sampled over several hours. Thus, each sample in the dataset is very large. To reduce the computational effort and storage, we select images at one critical time instant. From previous work, we know that during the heating-cooling cycle, the images with the highest contrast are usually most helpful to perform damage diagnosis. And, these images are often obtained when the thermal condition in the sample is unstable, especially during the heating process [117, 134].

We consider two options (two different time steps) for input images. The first one is based on the outputs of the finite element model. The images we obtain from the finite element model are a series of temperature fields with limited resolution in pixels. Therefore, for each pixel of the top surface, we take its temperature time-series profile and plot the first derivatives. These plots help us to identify the time step with the highest rate of change. Therefore, one option is to select the temperature field with as many peak first derivatives as possible. The second approach is to select based on the heating-cooling profile for the heating mat. We can select the time steps on the rising segment, before it reaches the designed highest temperature.

Another issue is the resolution of the images (inputs to the model). The thermal images from the finite element models usually have low resolution due to the use of the coarse mesh (limited by the computational cost). However, the convolutional cores of the pre-trained initial CNN usually have many pooling layers. The sizes of the images will generally be reduced into halves after each pooling layers. Therefore, to maintain a relatively high resolution regarding the original field in the later layers (that are specific to the structure being monitored), the input images cannot be too low in each dimension. Interpolation of the thermal images from finite element models is one way to overcome this issue.

5.2.3 Model training and validation

In the model training, we use the concept of transfer learning and take the advantage of sophisticated CNN architectures already available in the public domain. These parameters

have been trained on millions of samples on datasets such as ImageNet. We use the CNN core as the initial layer and only train the parameters within each subsequent sub-network. The finite element dataset is partitioned randomly into training and testing subsets. The loss function is set to be cross-categorical entropy, with Adam optimizer used for the training. Cross-categorical entropy (CE) is defined in Eq.5.3 below, where t_i represents the ground truth and s_i represents the score for each class i in C. $f()$ represents the activation function [135]. Adam optimizer is a widely used optimization algorithm for training deep neural networks, and it has many advantages over the classical stochastic gradient descent optimizer, such as suitability for noisy gradients, straightforward implementation, computational efficiency, and low memory requirement [39].

$$CE = -\Sigma_i^C t_i log(f(s_i)) \tag{5.3}$$

The validation of the model is done in two steps. The first step is from the reserved dataset from the finite element models. This step mainly checks the training effectiveness of the model. Decrease of loss function and improvement in prediction accuracy are expected. Comparison of the accuracy on both training and testing data can be used to check underfitting and over-fitting conditions. The second step of the validation is from the laboratory experiments with real samples. This step checks the performance of the trained model on real-world data. Section 5.3 discusses the validation results of the machine learning model with both simulated and laboratory datasets for a concrete specimen.

5.3 Illustrative Example

This section presents an example of structural health monitoring with deep convolutional neural network on a concrete specimen. The following steps are discussed below: (1) data generation with computer simulated models and laboratory experiments; (2) selection of inputs and outputs; (3) training of the model; and (4) performance assessment of the

model on both simulated and laboratory datasets.

5.3.1 Data set description and generation

5.3.1.1 Dataset from laboratory simulations

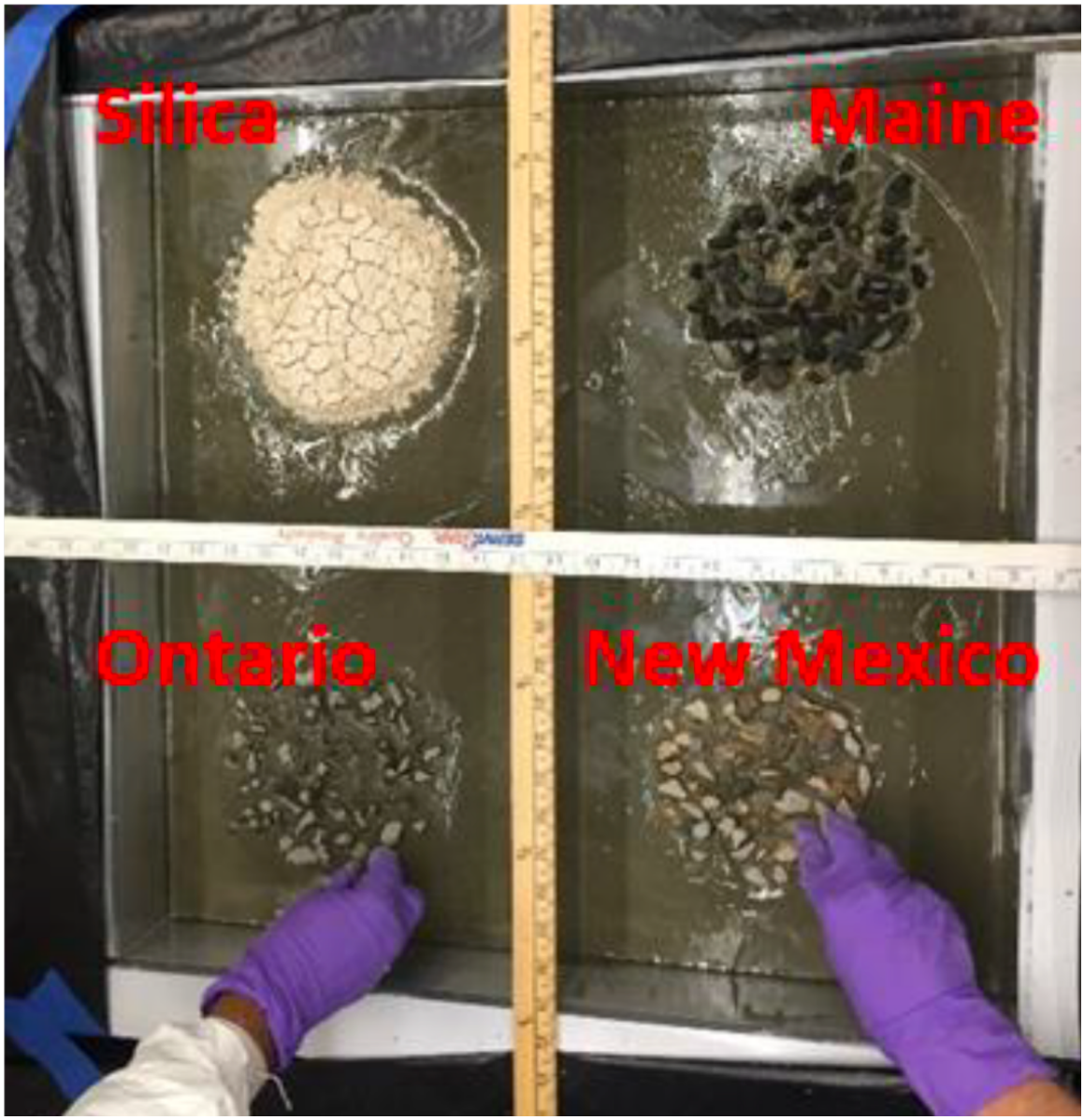

Figure 5.3: Placement of reactive aggregates in the test specimen

A concrete block with dimensions $60.96cm \times 60.96cm \times 15.24cm$ was cast and cured at Vanderbilt University. Each of the four quadrants of the concrete block has a different

type of reactive aggregate (single layer, mid-thickness, about 4 inches in diameter) that is prone to alkali silica reaction (ASR). As shown in the Fig. 5.3, the aggregate types used in each quadrant were amorphous silica (top left), Maine coarse aggregate (top right), Ontario coarse aggregate (bottom right), and New Mexico coarse aggregate (bottom right). The concrete block is cured in alkali solution under 60°C and 100%humidity for over a year to produce ASR damage. After 10 months of curing, cracks appeared on the two outside edges of the top left quadrant and on the horizontal edge of the bottom right quadrant, followed by gel effluent. The gel effluent was subjected to chemical characterization and the presence of ASR was confirmed [136]; the thermography experiment was performed subsequently.

Before the thermography experiment, the concrete specimen is removed from the oven and rested for a sufficiently long time to allow cooling to room temperature. During the thermography experiment, the specimen is placed on top of a heating mat; the other sides of the specimen are freely in contact with the ambient environment maintained at constant temperature [117]. The heating mat is programmed to provide the thermal load depicted in Figure 5.4. Temperature images of the top surface of the specimen are collected using an FLIR®Infrared (IR) camera every 30 seconds. The details of the sample and the experimental setup can be found in [137, 138, 139, 140].

5.3.1.2 Dataset from computer simulations

As mentioned in Section 5.2, we use finite element models to prepare the training data for the deep neural network. Brittle damage in concrete, such as cracking, could result in a significant reduction in its thermal conductivity [141]. Therefore, in the FE model, we simulate the damaged area by specifying its thermal conductivity to be 20% lower than the intact area's thermal conductivity based on Ref. [141]. The material properties of the concrete specimen are summarized in Table 5.2

The thermal load profile (heating and cooling) that was used for the thermography

Property	Value	Unit
Density	0.0003262	kg/m^3
Thermal conductivity (intact)	0.0015681	w / (m k)
Thermal conductivity (damage)	0.0009271	w / (m k)
Specific heat capacity	0.0009271	J/(kg k)

Table 5.2: Concrete material properties used in finite element models [1]

experiment in the laboratory is shown in Figure 5.4. The finite element simulation follows the same thermal profile as that of the laboratory experiment. The specific heating-cooling cycle in the experiment lasts about 10 hours in real-time.

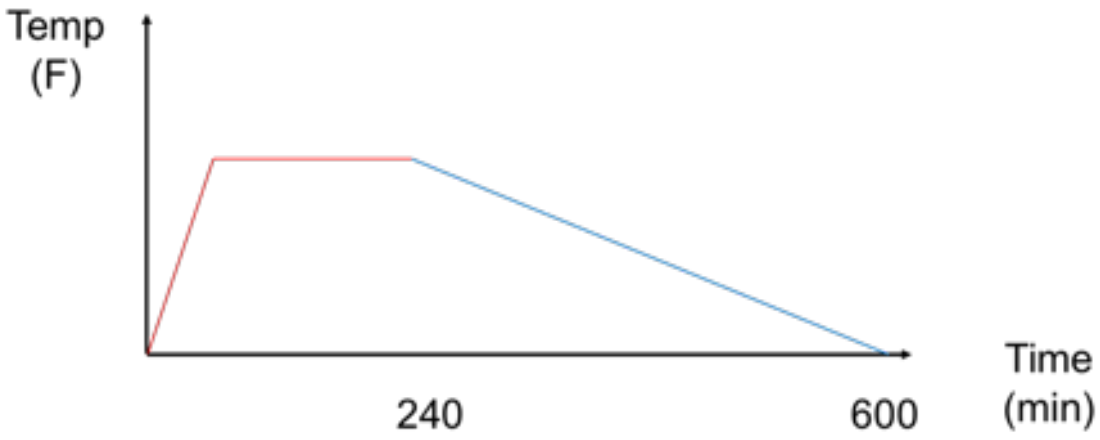

Figure 5.4: Heating and cooling profile of the experiment

To select appropriate parameters for the finite element models, we performed two rounds of tests for parametric study. The first round focuses on the number of CPUs. We fixed the mesh size and time step at $\Delta_x = \frac{L_z}{6}$ and $\Delta_t = 15''$, and choose various numbers of CPUs to perform the simulation; the results are shown in Table 5.3

Number of CPUs	Computational time ($'$)
1	6
2	4
4	3
8	5

Table 5.3: Computational time of the standard test (time-step = 15*sec* and finite element size = $\frac{L_z}{6}$) with different numbers of CPUs

The computational time deteriorates with the number of CPUs, due to the initialization time for parallel computing, and the communication between the nodes. Therefore, for further computer simulation, we choose only a single CPU. For the second round of the parametric study, we focus on how the combinations of different Δ_x and Δ_t values affect the computational time and simulation stability. The results are listed in Table 5.4

Time step($''$)	**Elements along L_z**	**CPU time($'$)**	***r*-value**
7.5	3	6	6.37×10^{-5}
7.5	6	14	2.55×10^{-4}
7.5	12	83	1.02×10^{-3}
15	3	3	1.27×10^{-4}
15	6	8	5.10×10^{-4}
15	12	41	2.04×10^{-3}
30	3	2	2.55×10^{-4}
30	6	4	1.02×10^{-3}
30	12	40	4.08×10^{-3}

Table 5.4: CPU time and *r*-value at different time steps and meshing sizes

As shown in the Table 5.4, for all combinations of Δ_x and Δ_t, the *r*-values are all much less than 0.5 (i.e., the CFL condition holds and the simulations are all stable). However, the CPU time varies significantly, from 4 minutes to 83 minutes. To better understand the accuracy of different simulations, we select the central point on the top surface as a reference and plot the temperature time-series during the entire heating-cooling process for different parametric combinations. The result is shown in Figure 5.5. The results from the simulations with different parameter combinations closely match each other, and the largest difference between the outputs at two parameter settings is about 1%. Thus the parametric combination $\Delta_t = 15''$ and $\Delta_x = \frac{L_z}{6}$ appears to give satisfactory accuracy and computing effort.

With the model properties above, we represent damage by assigning a lower thermal conductivity, as mentioned before. Three different damage shapes are considered, as shown in Figure 5.6. (Note that this is a very small number of shapes, only for the sake of illustration, and limited by computational resources; real-world applications will need to consider

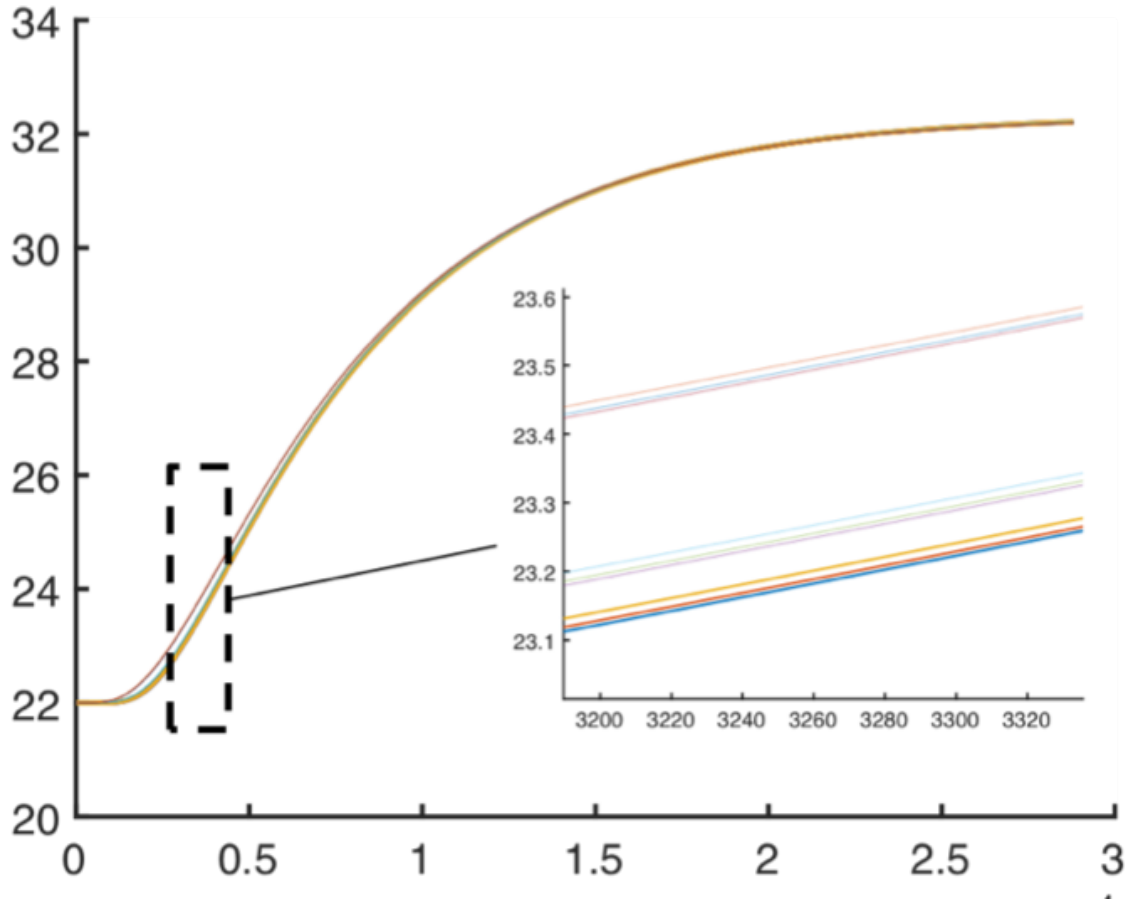

Figure 5.5: Temperature time-series plot for various parameter combinations

many more). We create models with all possible damage locations in x-y coordinates. We assign the damaged material to the middle two layers in the z dimension. Totally, we have over 1500 different damage conditions from the FE simulations.

5.3.2 Deep neural network model training and results

5.3.2.1 Deep neural network model

In this example, we use the convolutional core from the VGG-19 architecture. A brief description of VGG-19 can be found in Section 2.7. The detailed information about the setup of this specific damage diagnosis model is shown in Fig. 5.7. The inputs are selected

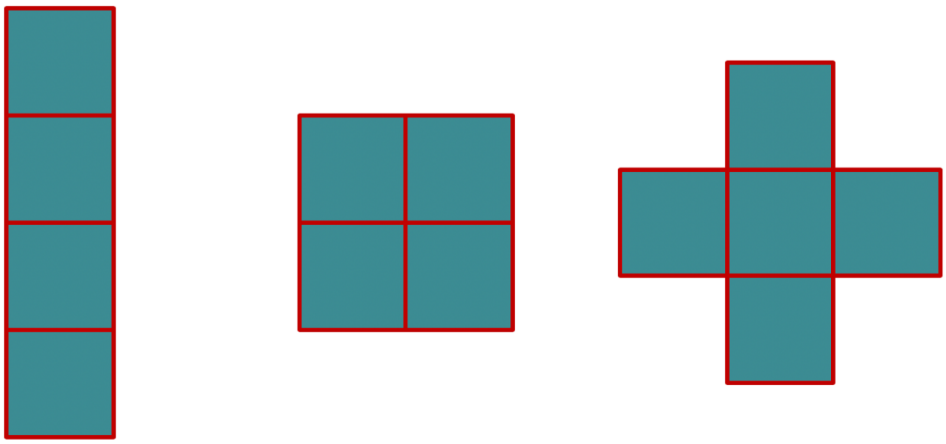

Figure 5.6: Damage shapes considered

thermal images of the top surface of the concrete samples, and the outputs are the horizontal and vertical damage locations, and the damage shape.

The output from the core CNN layers of VGG-19 has 4096 nodes, i.e., the output from the VGG-19 CNN core is a vector of size 4096×1.

In this example, our objectives are to predict the horizontal and vertical locations (x, y) and the shape of the damage. The neural network has three branches (sub-networks) after the VGG-19 CNN core. One sub-network is for horizontal location, another for vertical location, and the third for damage shape. We first tried to build the network to predict the x and y coordinates with numerical values. However, the performance of the model remained very poor even after extensive training and parameter tuning. One of the major reasons is that, given the limitation of computational power, the finite element model has only a 24×24 coarse mesh in the $x - y$ plane. This limits the choices for damage locations, and the number of samples that we can generate for the training dataset. Thus, the information that can be learned by the model is rather limited. In this example, we divide the image into a 4×4 grid. Then, the proposed damage diagnosis model predicts the possible locations

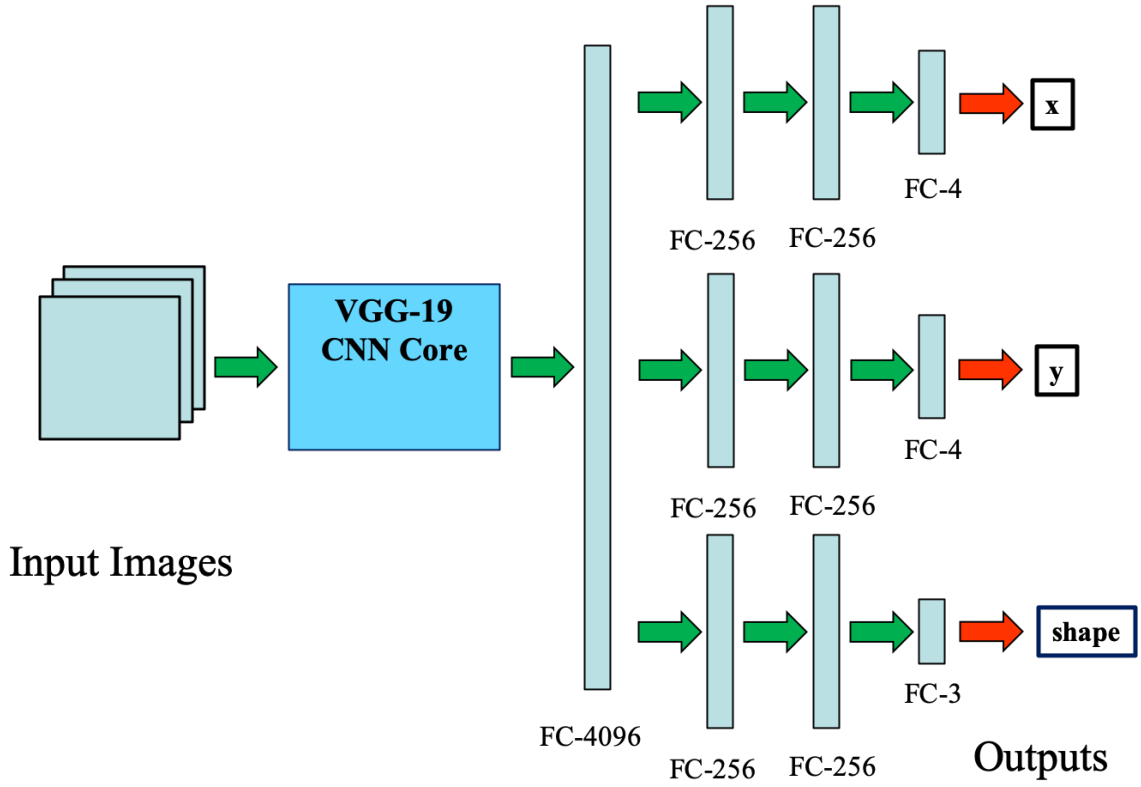

Figure 5.7: Proposed deep neural network architecture for damage diagnosis

within these 4 horizontal and 4 vertical locations on the grid. We use the following one-hot encoding for the locations and shapes in Table 5.5.

x **locations**		**Results by one-hot encoding**
0.00	0.25	1000
0.25	0.50	0100
0.50	0.75	0010
0.75	1.00	0001

Table 5.5: One-hot encoding for x locations

As mentioned earlier, the proposed neural network has three branches. After passing the input images through the VGG-19 CNN core, sub-network 1 takes the outputs from VGG-19 CNN core and uses two additional fully connected (FC) layers of 256 nodes each (FC-256), and one additional FC layer with 4 nodes (FC-4) to predict the encoded horizontal location x. Similarly, sub-network 2 takes the outputs from the VGG-19 CNN core, and

uses two additional FC-256 layers and one additional FC-4 to predict the encoded vertical location y. Sub-network 3 also has two FC-256 layers and one FC-3 layer for the damage shape (since we have three different shapes in our data set).

The first derivatives of the temperature profiles are shown in Fig.5.8. From the figure, it is seen that time step 185 has the most number of counts. Therefore, we set the input images to be the temperature fields at time steps 184, 185, 186. An alternative approach is based on the heating-cooling profile, as shown in Fig.5.4. We can select the time steps based on the rising segment (left). Thus we select time steps 29, 30, and 31 to form the second option of the input data set.

As mentioned earlier, the original thermal images from the finite element models have a resolution of 24×24. And there are 5 max-pooling layers in the VGG-19 CNN core that we use for transfer learning. Each time when an image passes through one of these max-pooling layers, its size reduces by 50% in each dimension. Besides, each convolution calculation with a 3×3 filter results in a reduction of 2 pixels along both dimensions. Therefore, in order to fully take advantage of transfer learning using the pre-trained CNN core, we have to obtain images with high resolution. Therefore, we use the idea of interpolation and transfer the original images to a resolution of 128×128. This interpolation process is applied to the entire data set, which has over 1500 images.

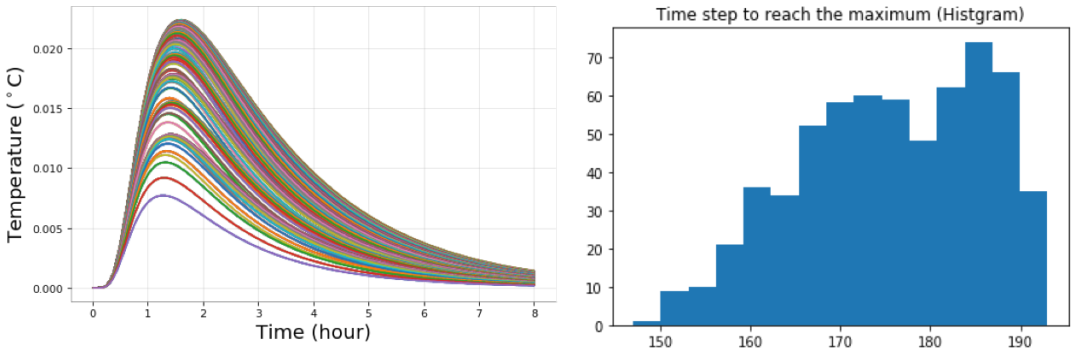

Figure 5.8: First derivatives of the temperature profiles of each pixels on the top surface

5.3.2.2 Model Training

The proposed damage diagnosis model is trained in Python with Scikit-learn and TensorFlow packages. In the TensorFlow architecture, we build on the VGG-19 CNN core with the pre-trained parameters on ImageNet data set. We randomly divide the data into two subsets, 80% for training and 20% for validation. Since we have three sub-networks for the prediction of x, y, and damage shape, we freeze the CNN core from VGG-19 and only train the parameters within each sub-network. We set the loss function to be cross-categorical entropy and used Adam optimizer used for the training.

The GPU computing cluster at Vanderbilt University‘‘s ACCRE (Advanced Center for Computing Research and Education) facility is used. ACCRE uses Nvidia Pascal Architecture, and each GPU has 3584 CUDA cores. Each of the nodes has 12GB GPU memory. Each of the three sub-networks is assigned one GPU node and is trained individually for 1000 epochs. The validation calculation follows the training calculation in each epoch. The total process for each sub-network takes about 45 minutes on one GPU node.

5.3.3 Results

5.3.3.1 Results on simulated dataset

As described in the previous section, we have 2 options for input selection and 2 options for output encoding. For the input image selection, we have one based on the top surface temperature profile and one based on the temperature profile of the heating mat at the bottom of the specimen. For the output encoding, we categorize and encode the outputs for damage locations into 4×4 grids. In this case, the last layer (output layer) in sub-networks 1 and 2 has four nodes, and each of them has an activation function of softmax to match the one-hot encoding. And the loss function is chosen to be cross-categorical entropy. We can also map the output for x and y into the range of $[0, 1]$. For this output setting, the last layer (output layer) in sub-networks 1 and 2 has only one node, and its activation function

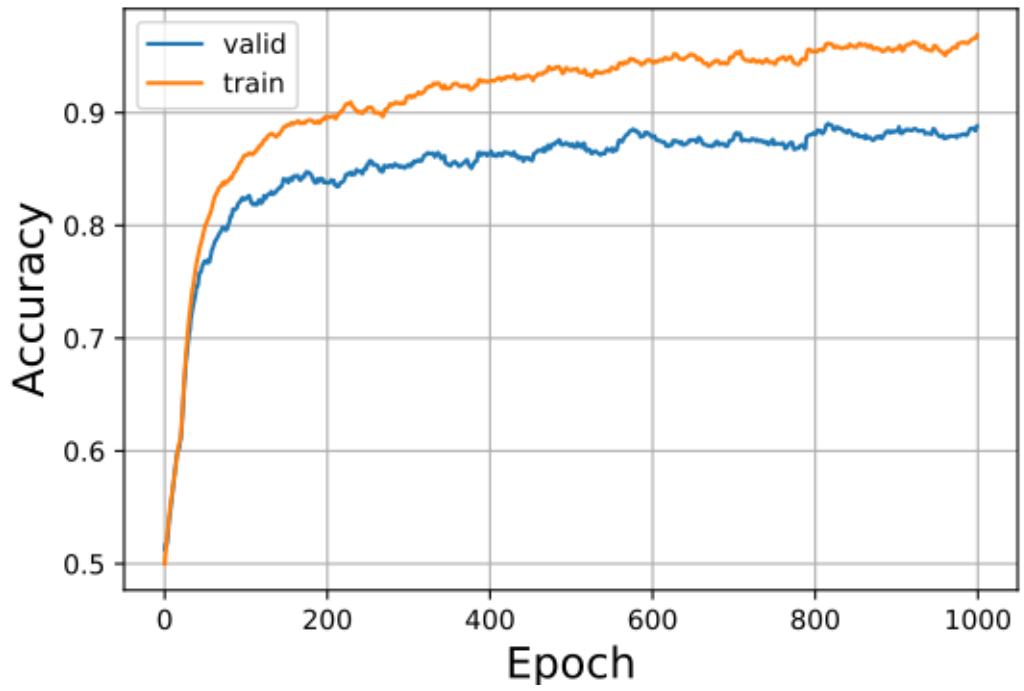

Figure 5.9: Accuracy of x on the training and validation data sets during the learning

is set to be sigmoid to force the value into the range $[0,1]$. And the loss function needs to be changed to "RMS" instead of "cross-categorical entropy".

$$RMS = \frac{1}{n}\Sigma_i(\bar{Y}_i - Y_i)^2 \tag{5.4}$$

After training for 1000 epochs, we find that 3 out of 4 input/output combinations are not satisfactory. Setting input images based on the top surface temperature profile results in an accuracy of at most 60%. This is because the contrast between the elements on the top surface becomes milder with increased heating. Thus, each of the samples from this group brings less information than the ones with better contrast among each element. Therefore, many more samples are needed to improve the model accuracy. For the setting of the outputs that have been mapped within the range $[0,1]$, the model has an accuracy of about 30% with the same training effort. An explanation for this is that the samples in our data

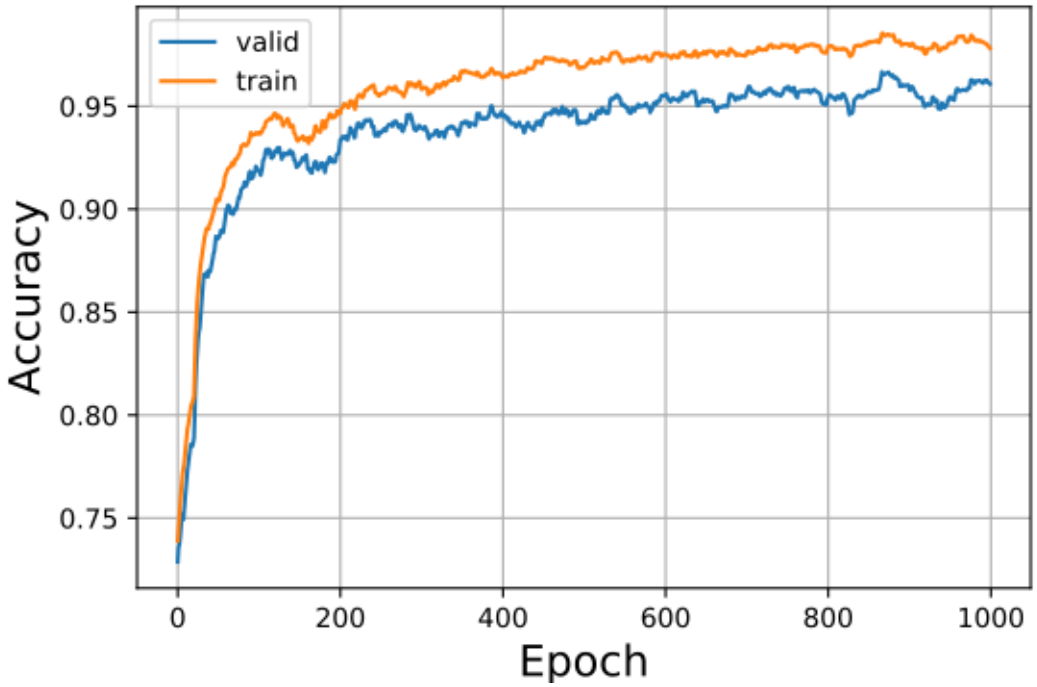

Figure 5.10: Accuracy of y on the training and validation data sets during the learning

set locate on a grid of 24×24 and we have at most 3 samples (shapes) at each grid point. Thus we do not have enough samples for an accurate regression model, and the model is under-fitted.

However, when we select the second category of input images (based on the heating-cooling profile of the heating mat), and the categorical one-hot encoded outputs, to build a classification model, the performance is much better. The performance for x and y prediction is shown in Fig. 5.9 and Fig. 5.10. Sub-network 1 for x prediction shows over 95% accuracy for the training data set and close to 90% accuracy for the validation data set. The performance of the sub-network 1 exceeds 90% accuracy after about 200 epochs of training and reaches convergence after about 800 epochs. Sub-network 2 for y prediction shows over 95% accuracy for both training and validation data sets. This sub-network exceeds 90% accuracy after about 100 epochs of training and reaches convergence at about 900 epochs.

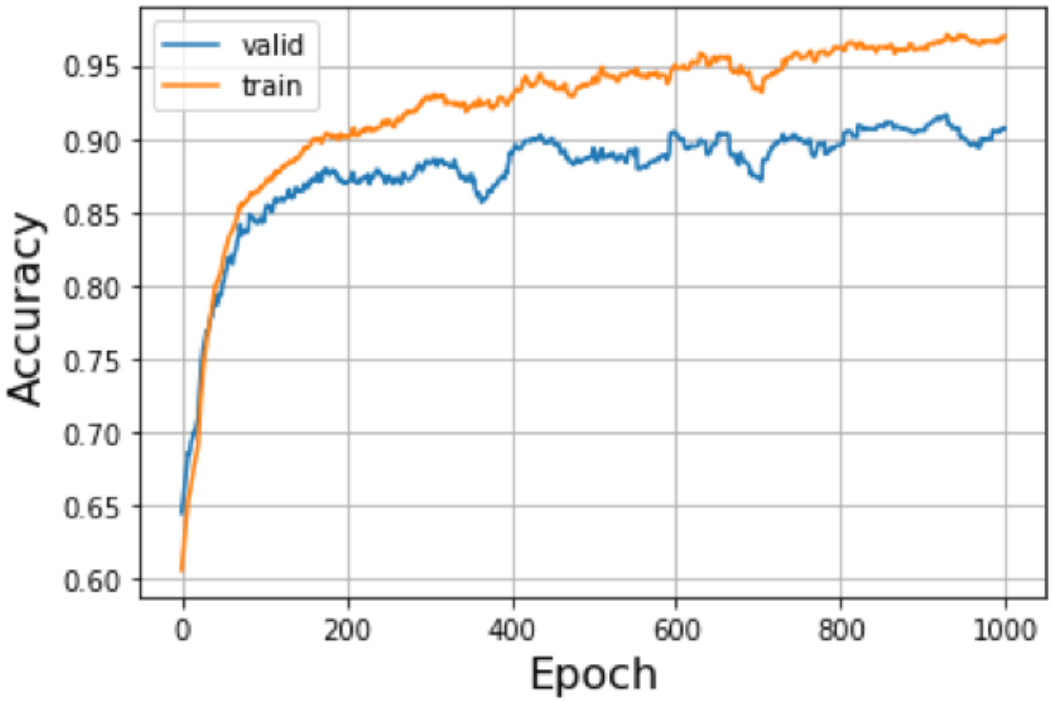

Figure 5.11: Accuracy of shape predictions on the training and validation data sets during the learning

Sub-network 3, as mentioned earlier, is designed to identify the geometric shape of the damage. The outputs of the shape are encoded into vectors of 3 elements each by one-hot encoding. The output layer of the sub-network has a softmax activation function on each of the 3 nodes. The loss function is based on cross-categorical entropy as mentioned in Section 5.2. This sub-network is also trained for 1000 epochs with 80% of the data (randomly selected), and the validation task uses the remaining 20% of the data. As a result, as shown in Fig. 5.11, model accuracy increases rapidly and reaches over 95% accuracy with the training data set and over 90% with the validation data set. Similarly, after about 900-epoch training, the model reaches a steady performance in terms of accuracy.

To sum up, in this section, we discussed the setup of the 3 sub-networks, and the corresponding training and validation details. We discussed two choices for input images and two choices for output encoding methods. The best performance results from using the images obtained when the heating mat's temperature ascends rapidly as inputs and one-

hot encoding for the outputs. This combination brings over 90% accuracy (both training and validation) in all three sub-networks (i.e., damage location (x, y) and damage shape). Whereas, the accuracies failed to reach about 50% from building a similar deep convolutional neural network from scratch.

5.3.3.2 Validation with laboratory experiments

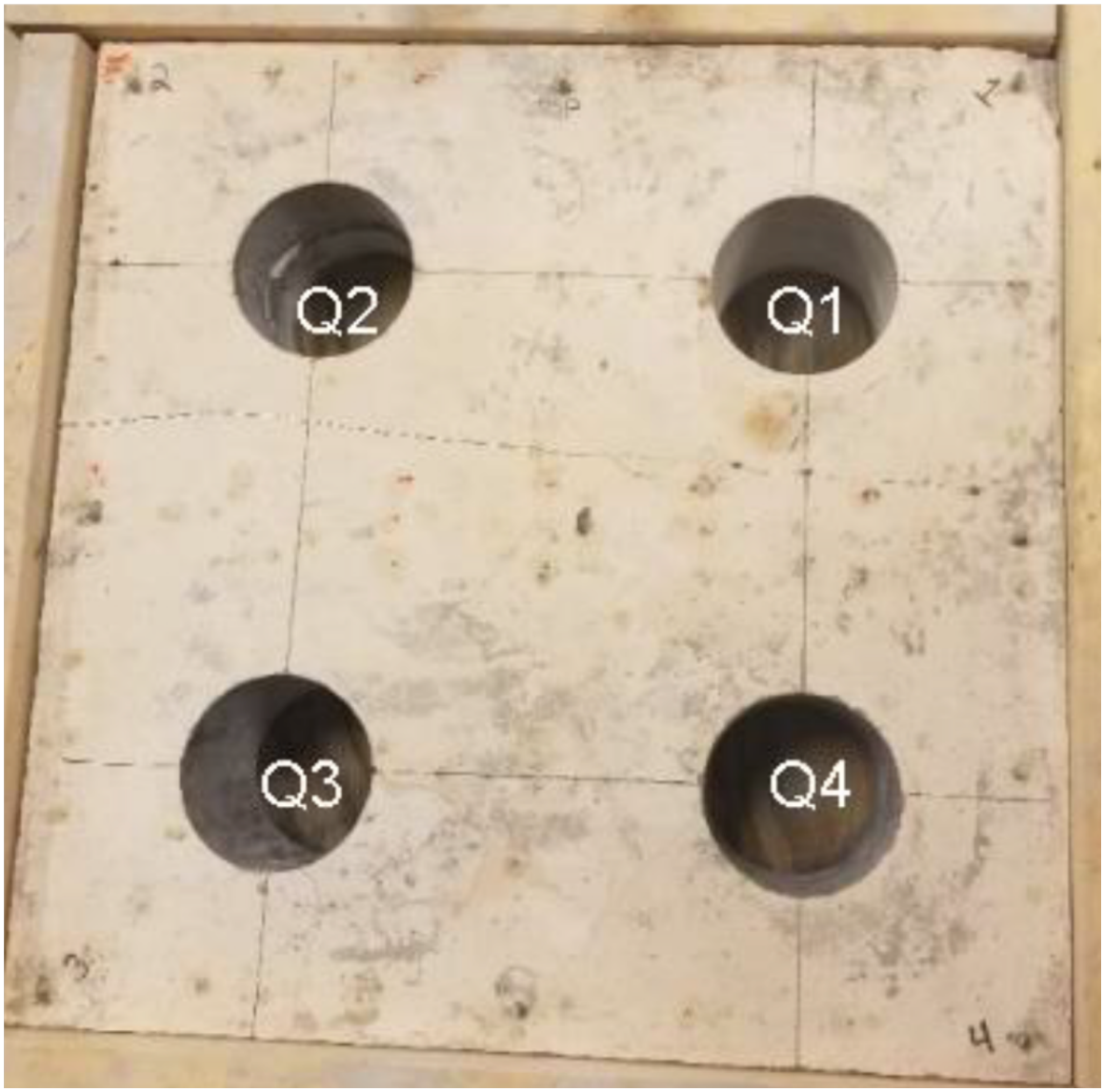

Figure 5.12: Core extraction from the concrete specimen

As described in Section 5.3.1.1, we carried out thermography testing of the concrete

specimen in the laboratory. The heating-cooling profile used in thermography testing is the same as for the finite element simulations used to train the machine learning model. The thermal image obtained from the laboratory experiment at the same time instant as the training data set is used to test the model. The trained model identifies the top-left quadrant of the concrete slab as the most probable damaged region, and the third damage shape (the plus sign) as most probable. We validated the result regarding the location by extracting cores from each of the four quadrants of the slab as shown in Fig. 5.12. It was observed that the top-left quadrant had a large void, as a result of which the core from this quadrant could only be extracted in multiple pieces. Detailed information of the concrete specimen and results from core testing can be found in [137]. The top left quadrant had a large amount of damage, and the lower-left and lower-right quadrants had small cracks caused by alkali‘‘silica reaction (ASR). Thus the proposed model is able to correctly identify the most damaged region. Since the model is constructed to predict only the single most probable location of damage, it did not identify regions with smaller cracks at the lower portions of the concrete specimen. This result shows that the transfer learning with a deep convolutional neural network can be used to identify damage locations. The identification of damage shape was inconclusive due to two limitations: (1) only three shapes were used in the model training, and the model identified the cross shape as most likely; and (2) the core was extracted in multiple pieces due to the large void. The validation of damage shape identification will need model training with many more possible shapes (this is computationally demanding), and the induced damage in the experiment will need to be less drastic so that an intact core could be extracted and then carefully cut to identify the damage shape. Further improvement is also needed in the machine learning model in future so that it can identify multiple possible damage locations; currently it only identifies the most damaged location.

5.4 Uncertainty Quantification in the Deep Neural Network Model

Though deep learning architectures show tremendous performance in various machine learning applications, these models do not capture the model uncertainty in regression and classification tasks [142, 143]. Gal and Ghahramani developed a theoretical framework based on the dropout technique in training a deep neural network to achieve approximate Bayesian inference and quantify the model uncertainty. Since then, researchers have used dropout to study the uncertainty in various models, such as recurrent neural networks [144, 145, 146, 147].

The application of dropout was proposed by Srivastava et al. to handle the over-fitting problem in deep neural network training[148]. The idea is that each of the nodes in a dropout layer has a given probability to be turned off during the training epoch. The process can be visualized in Figure 5.14. The dropout process is carried out in each layer individually. The dropout probability of each node, called dropout rate, only affects the nodes within a single layer. In practice, researchers usually keep the same dropout rate for all the selected layers within one deep neural network model.

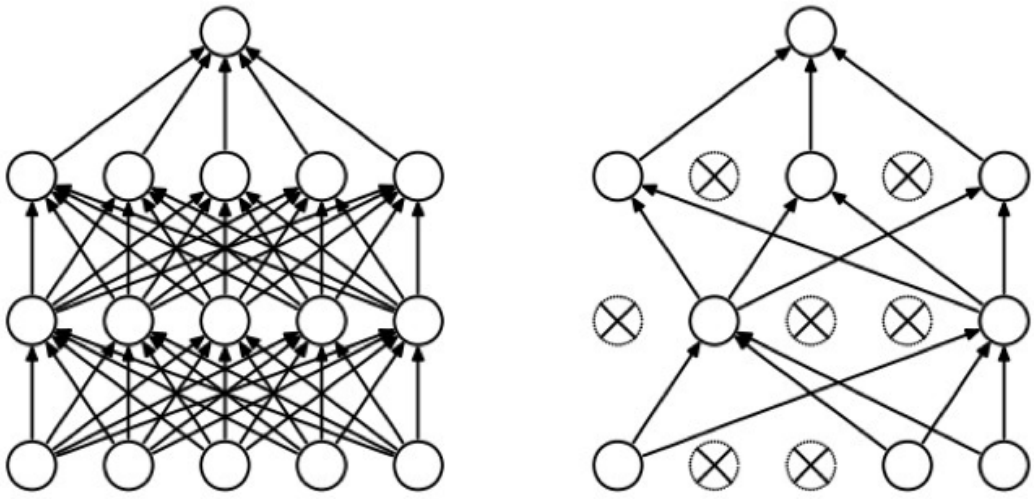

(a) Standard Neural Net (b) After applying dropout.

Figure 5.13: Dropout Process in Deep Neural Network

In our case, our dropout layers were set as the last two fully connected (FC) layers.

To implement that in Keras, we appended a Dropout layer after each of the FC layers. A Dropout layer in Keras is a layer, whose nodes will be turned on and off following a Bernoulli distribution during the training and prediction steps. The dropout rate is typically set as the one that gives the minimum accuracy difference between the training and validation processes. With the trained model using the selected dropout rate, we can perform Monte Carlo simulation and quantify the uncertainty in diagnosis.

Layer (type)	Output Shape	Param #
vgg19 (Model)	(None, 4, 4, 512)	20024384
flatten_7 (Flatten)	(None, 8192)	0
dense_19 (Dense)	(None, 256)	2097408
dropout_13 (Dropout)	(None, 256)	0
dense_20 (Dense)	(None, 256)	65792
dropout_14 (Dropout)	(None, 256)	0
dense_21 (Dense)	(None, 4)	1028

Total params: 22,188,612
Trainable params: 22,188,612
Non-trainable params: 0

Figure 5.14: Dropout Model for Bayesian Inference

Consider the prediction of x location of damage as an example. We explore the dropout rate within a range of values and found that 0.04 provides us with the lowest training vs validation accuracy gap and a prediction accuracy over 90%. With the trained model, we perform 1000 Monte Carlo simulations. In our case, we used one-hot encoding and the output of the sub-network has 4 nodes. Within each Monte Carlo run, we have predicted values for each of the 4 nodes. After 1000 runs, we plot the histogram of the predictions in Figure 5.15. As shown in Section 5.3, the model predicts location **0** as the x-location for damage and the coring results also agree on that. With the Monte Carlo dropout model, we can predict the x-location with a probability with uncertainty.

Applying Monte Carlo simulation with dropout in deep learning models thus helps in

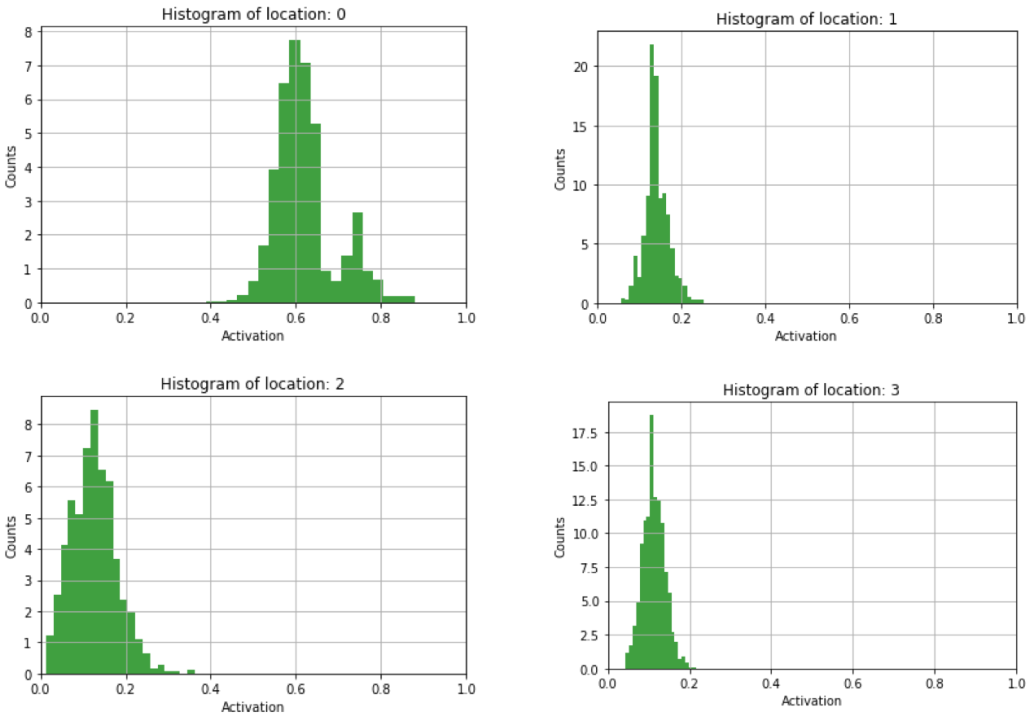

Figure 5.15: Monte Carlo of Dropout Model as Bayesian Inference

quantifying the model uncertainty. The computational effort added to a model with dropout layers is not too significant compared with that without dropout (15% more time on average). This mitigates the problem of representing uncertainty in deep learning models with reasonable computational cost and prediction accuracy.

5.5 Conclusion

This chapter investigated the use of transfer learning and deep neural network in structural health monitoring, and illustrated the methodology for concrete damage diagnosis. The proposed methodology overcomes several challenges in practical SHM. The first problem is the lack of data since real-world laboratory experiments on structures are time-consuming and expensive. We overcome this using two strategies, one focusing on data generation and one on model construction. We use finite element-based computer simulations to generate the training data. We study the resource selection for simulation to balance

the accuracy and computational cost. With the carefully designed and simulated models, we generated over 1500 samples with different damage shapes at various locations.

For model construction, we proposed using the idea of transfer learning and used the pre-trained CNN core from VGG-19, which is a powerful deep convolutional neural network trained with a large volume of image data. The proposed deep neural network model for damage diagnosis has three sub-networks (branches) added to the VGG-19 model. Each sub-network focuses on one output parameter (x location, y location, and damage shape), and all three are trained in parallel. We tested different selections for input images and output encoding. With the optimal selection, the proposed model achieved over 90% accuracy in predicting the horizontal and vertical locations and the damage shape in both the training and validation data sets. We also tested the model with data from physical laboratory experiments with concrete specimens subjected to alkali-silica reaction, and the model was able to correctly identify the most damaged location. In addition, we also used the model to classify which shape the damage is closest to. Lastly, we also quantified the diagnosis uncertainty of the proposed deep convolutional neural network model using the dropout technique during training, followed by Monte Carlo simulation of the diagnosis inference.

Chapter 6

Conclusion

This dissertation work explored data-driven methods for structural health monitoring by considering two monitoring techniques and quantified the uncertainty in the diagnosis result of each technique. The proposed methodologies were applied using heterogenous material concrete) in the examples; however, the idea and potential application is general for both homogenous and heterogenous materials. First, traditional image processing with thermography was considered for internal damage diagnosis. Next, the new damage sensitive features were developed for damage detection and localization with time-series vibration data. Third, the dissertation explored feature automation and interior damage diagnosis with deep convolutional neural network and transfer learning in problems with limited and small datasets. In each case, the reliability of the data-driven method was assessed through uncertainty and robustness analyses. Specific contributions under each method are summarized below.

6.1 Summary of Accomplishments

Chapter 3 investigated thermal image processing for internal damage diagnosis in concrete. Detection, localization, as well as quantification of the damage were considered. An important feature of the investigation is uncertainty quantification in the damage diagnosis result, by aggregating various sources of uncertainty introduced at each step of the image processing. Further, global sensitivity analysis is applied to identify the dominant contributors to diagnosis uncertainty. Based on the results of uncertainty quantification and global sensitivity analysis, a Bayesian technique is formulated to identify the optimal values of parameters to be selected at each step of the image processing, in order to minimize the uncertainty in diagnosis. An illustrative example of damage diagnosis of a concrete

slab is used to examine the effectiveness of the damage diagnosis technique as well as the uncertainty quantification and parameter selection methods.

Chapter 4 developed a damage diagnosis methodology that overcomes difficulties faced by most SHM methods aiming for homogenous materials and is capable of detecting and localizing the damage, using harmonic vibration tests with swept and sinusoidal waveforms. The proposed damage detection procedure uses novel features based on Singular Value Decomposition (SVD) of linearly swept waveform test data. The latter singular vectors of the intact basis are found to be sensitive to the presence of damage. The damage localization uses a K-factor metric calculated using sinusoidal waveform test data. The K-factor is used to measure the deviation of a signal away from a sinusoid. The damage diagnosis methodology is demonstrated and validated using experiments on thin concrete slabs with drilled holes and thicker concrete blocks with alkali-silica reaction (ASR) damage.

Chapter 5 proposed a damage diagnosis framework using a deep convolutional neural network and transfer learning. We use thermography to study the heat transfer characteristics and infer the presence of damage in the structure. It is challenging to get sufficient data samples for training deep neural networks, especially in the field of structural monitoring. Therefore we use finite element computer simulations to generate a large volume of training data for the deep neural network. The training data include multiple damage shapes and locations. These computer-simulated data are used along with pre-trained convolutional cores of a sophisticated computer vision-based deep convolutional network to facilitate effective transfer learning. The convolutional neural network automatically generates features for damage diagnosis as opposed to manual feature generation in traditional image processing. Systematic parametric selection study is carried out to investigate accuracy vs. computational expense in generating the training data. The methodology is demonstrated with an example of damage diagnosis in concrete, a heterogeneous material, using both computer simulations and laboratory experiments. The combination of finite element simulation, transfer learning and experimental data is found to achieve high accu-

racy in damage localization with affordable effort. We also successfully perform Bayesian Inference on the proposed deep learning model using the dropout technique and Monte Carlo simulation, in order to quantify the uncertainty in damage diagnosis.

6.2 Future Work

For thermal image-based diagnosis, we can investigate the performance of the thermal image processing for more complicated and realistic damage scenarios in concrete. Concrete is a heterogeneous material consisting of aggregates, reinforcement and voids; thus damage diagnosis using thermal images might pose significant challenges for realistic damage scenarios caused by mechanisms such as alkali silica reaction, chloride diffusion etc. The thickness of the slab is another challenge; the example here used a relatively thin slabs with well-defined damage (drilled holes and specific locations of ASR damage). Future work needs to investigate the effectiveness of damage diagnosis for realistic structural sizes and damage geometries. However, the proposed methodology for uncertainty quantification, sensitivity analysis, and parameter value selection is general and can be applied to a variety of image processing-based damage diagnosis techniques.

Considering vibration-based diagnosis, we could explore several additional investigations. First, the locations of the actuator in the experiments were based on experience. A systematic study of the effect of different locations of the actuator would be valuable. Second, in the harmonic vibration experiments, the frequencies of the waveforms were selected based on the allowable range of the equipment. There might be a much better selection of the frequencies within this range and investigation in this direction could be helpful in improving the proposed methodology. Meanwhile, other metrics could be explored for damage detection and localization, and advanced machine learning algorithms could be investigated to improve the overall damage diagnosis. In this work, we did not consider the effect of temperature variation on the performance of the proposed method. Temperature may affect sensor bonding and the resultant data, and this effect needs to be

studied in the future. As our proposed method is data driven, we have not explicitly considered any nonlinearity in the detection and localization procedure. Finally, our experiments focused on the performance of the methodology in localizing the damage on a 2-D plane. Future research needs to investigate the extension of the proposed methodology to 3-D damage localization.

For deep learning-based damage diagnosis, additional research can be pursued to improve the capability and robustness of the methodology. The first direction is data generation. Due to the limitation of computational resources, we generated only 1500 samples with three damage shapes. Investment can be made in more accurate finite element models, and generation of a larger number of samples with multiple damage shape options. Second, in training our model, we manually selected the thermal images at a specific time instant. Since our samples are image volumes (videos), state-of-the-art video processing techniques can be applied to extract more information and automate the entire process. Third, the model currently identifies only a single location as the most probable damaged location. The model could be enhanced to identify multiple damage locations and damage shapes in case they are present in the structure. However, this is computationally demanding, since it needs the generation of a large amount of training data set using the finite element simulations, by considering many possible damage locations and shapes.

Lastly, future work is also needed to comprehensively quantify the uncertainty in the damage diagnosis. There are multiple sources of uncertainty, such as variability of structural properties, errors uncertainties in measurement and processing of sensor data, and approximations in the damage diagnosis methodology. Only the uncertainty in the deep learning model was quantified using the dropout technique in this work. Both classical and Bayesian approaches have been proposed earlier [55, 149], for damage detection, localization and quantification; however, these are directly based on experimental data. The methods need to be extended to the proposed diagnosis approach that combines machine learning, transfer learning, simulation-based training data, and experimental observations,

by aggregating the uncertainty contributions from these multiple sources. Meanwhile, future work also involves to investigate information fusion of multiple structural health monitoring techniques and the uncertainty quantification within structural health monitoring systems. Efforts can be done in finding how to make a comprehensive decision with multiple damage diagnosis and monitoring techniques with techniques, such as Bayesian Networks.

BIBLIOGRAPHY

[1] J. F. Lamond, J. H. Pielert, Significance of tests and properties of concrete and concrete-making materials, in: ASTM International Standards Worldwide STP 169D, ASTM West Conshohocken, PA, pp. 691–696.

[2] O. Plekhov, T. PALIN-LUC, N. Saintier, S. Uvarov, O. Naimark, Fatigue crack initiation and growth in a 35crmo4 steel investigated by infrared thermography, Fatigue & Fracture of Engineering Materials & Structures 28 (2005) 169–178.

[3] S. M. Talai, D. A. Desai, P. S. Heyns, Infrared thermography applied to the prediction of structural vibration behaviour, Alexandria Engineering Journal (2019).

[4] Y. Bao, S. Mahadevan, Uncertainty quantification of thermal image-based concrete diagnosis, International Journal of Sustainable Materials and Structural Systems 2 (2015) 77–95.

[5] E. Figueiredo, G. Park, J. Figueiras, C. Farrar, K. Worden, Structural health monitoring algorithm comparisons using standard data sets, Technical Report, Los Alamos National Lab.(LANL), Los Alamos, NM (United States), 2009.

[6] D. Adams, R. Allemang, A frequency domain method for estimating the parameters of a non-linear structural dynamic model through feedback, Mechanical Systems and Signal Processing 14 (2000) 637–656.

[7] W. Contreras, S. Ziavras, Low-cost, efficient output-only infrastructure damage detection with wireless sensor networks, IEEE Transactions on Systems, Man, and Cybernetics: Systems (2017).

[8] J. J. Lee, M. Shinozuka, A vision-based system for remote sensing of bridge displacement, Ndt & E International 39 (2006) 425–431.

[9] I. Abdel-Qader, S. Pashaie-Rad, O. Abudayyeh, S. Yehia, Pca-based algorithm for unsupervised bridge crack detection, Advances in Engineering Software 37 (2006) 771–778.

[10] D. Lattanzi, G. R. Miller, Robust automated concrete damage detection algorithms for field applications, Journal of Computing in Civil Engineering 28 (2012) 253–262.

[11] H. Leclerc, J.-N. Périé, S. Roux, F. Hild, Integrated digital image correlation for the identification of mechanical properties, in: International Conference on Computer Vision/Computer Graphics Collaboration Techniques and Applications, Springer, pp. 161–171.

[12] P. Poozesh, J. Baqersad, C. Niezrecki, E. Harvey, R. Yarala, Full field inspection of a utility scale wind turbine blade using digital image correlation, CAMX, Orlando, FL 10 (2014) 2891–2960.

[13] C. Murray, A. Hoag, N. A. Hoult, W. A. Take, Field monitoring of a bridge using digital image correlation, in: Proceedings of the Institution of Civil Engineers-Bridge Engineering, volume 168, Thomas Telford Ltd, pp. 3–12.

[14] H.-N. Li, D.-S. Li, G.-B. Song, Recent applications of fiber optic sensors to health monitoring in civil engineering, Engineering structures 26 (2004) 1647–1657.

[15] D. Kinet, P. Mégret, K. W. Goossen, L. Qiu, D. Heider, C. Caucheteur, Fiber bragg grating sensors toward structural health monitoring in composite materials: Challenges and solutions, Sensors 14 (2014) 7394–7419.

[16] N. Mallik, A. Wali, N. Kuri, Damage location identification through neural network learning from optical fiber signal for structural health monitoring, in: Proceedings of the 5th International Conference on Mechatronics and Control Engineering, ACM, pp. 157–161.

[17] S. E. Umbaugh, Computer vision and image processing: a practical approach using cviptools with cdrom, Prentice Hall PTR, 1997.

[18] S. Kabir, P. Rivard, D.-C. He, P. Thivierge, Damage assessment for concrete structure using image processing techniques on acoustic borehole imagery, Construction and Building Materials 23 (2009) 3166–3174.

[19] J. C. Russ, The image processing handbook, CRC press, 2016.

[20] B. K. Horn, R. J. Woodham, Destriping landsat mss images by histogram modification, Computer Graphics and Image Processing 10 (1979) 69–83.

[21] C. R. Farrar, K. Worden, Structural Health Monitoring.: A Machine Learning Perspective, John Wiley & Sons, 2012.

[22] T. Viangteeravat, D. M. Wilkes, Modified noncausal smoothing filter and low rank matrix approximation for noise reduction, in: Signal Processing, Sensor Fusion, and Target Recognition XIX, volume 7697, International Society for Optics and Photonics, p. 76971K.

[23] C. Ya-Lun, Statistical analysis with business and economic applications, Holt, Rinehart and Winston, 1963.

[24] H. Akaike, A new look at the statistical model identification, in: Selected Papers of Hirotugu Akaike, Springer, 1974, pp. 215–222.

[25] J. A. Cadzow, D. M. Wilkes, R. A. Peters, X. Li, Image texture synthesis-by-analysis using moving-average models, IEEE transactions on aerospace and electronic systems 29 (1993) 1110–1122.

[26] S. Chaudhuri, S. Chatterjee, N. Katz, M. Nelson, M. Goldbaum, Detection of blood vessels in retinal images using two-dimensional matched filters, IEEE Transactions on medical imaging 8 (1989) 263–269.

[27] P. William K., Digital Image Processing, John Wiley —& Sons, Inc., New York, 5 edition, 2001.

[28] P. Litwinowicz, Processing images and video for an impressionist effect, in: Proceedings of the 24th annual conference on Computer graphics and interactive techniques, Citeseer, pp. 407–414.

[29] R. Franke, A critical comparison of some methods for interpolation of scattered data, Technical Report, NAVAL POSTGRADUATE SCHOOL MONTEREY CA, 1979.

[30] B. Schölkopf, S. Mika, A. Smola, G. Rätsch, K.-R. Müller, Kernel pca pattern reconstruction via approximate pre-images, in: International Conference on Artificial Neural Networks, Springer, pp. 147–152.

[31] S. Mika, B. Schölkopf, A. J. Smola, K.-R. Müller, M. Scholz, G. Rätsch, Kernel pca and de-noising in feature spaces, in: Advances in neural information processing systems, pp. 536–542.

[32] P. N. Belhumeur, J. P. Hespanha, D. J. Kriegman, Eigenfaces vs. fisherfaces: Recognition using class specific linear projection, IEEE Transactions on Pattern Analysis & Machine Intelligence (1997) 711–720.

[33] J. Yang, D. Zhang, A. F. Frangi, J.-y. Yang, Two-dimensional pca: a new approach to appearance-based face representation and recognition, IEEE transactions on pattern analysis and machine intelligence 26 (2004) 131–137.

[34] C. Zang, M. Imregun, Structural damage detection using artificial neural networks and measured frf data reduced via principal component projection, Journal of sound and vibration 242 (2001) 813–827.

[35] F. Magalhães, A. Cunha, E. Caetano, Vibration based structural health monitoring

of an arch bridge: from automated oma to damage detection, Mechanical Systems and Signal Processing 28 (2012) 212–228.

[36] N. C. Yoder, D. E. Adams, Vibro-acoustic modulation utilizing a swept probing signal for robust crack detection, Structural Health Monitoring 9 (2010) 257–267.

[37] T. Kanungo, D. M. Mount, N. S. Netanyahu, C. D. Piatko, R. Silverman, A. Y. Wu, An efficient k-means clustering algorithm: Analysis and implementation, IEEE Transactions on Pattern Analysis & Machine Intelligence (2002) 881–892.

[38] A. Likas, N. Vlassis, J. J. Verbeek, The global k-means clustering algorithm, Pattern recognition 36 (2003) 451–461.

[39] D. P. Kingma, J. Ba, Adam: A method for stochastic optimization, arXiv preprint arXiv:1412.6980 (2014).

[40] J. Wang, F. Chen, L. E. Dellalana, M. H. Jagasia, E. R. Tkaczyk, B. M. Dawant, Segmentation of skin lesions in chronic graft versus host disease photographs with fully convolutional networks, in: Medical Imaging 2018: Computer-Aided Diagnosis, volume 10575, International Society for Optics and Photonics, p. 105750N.

[41] Y. Chi, J. Wang, Y. Zhao, J. H. Noble, B. M. Dawant, A deep-learning-based method for the localization of cochlear implant electrodes in ct images, in: 2019 IEEE 16th International Symposium on Biomedical Imaging (ISBI 2019), IEEE, pp. 1141–1145.

[42] I. Goodfellow, Y. Bengio, A. Courville, Deep learning, MIT press, 2016.

[43] J. Yosinski, J. Clune, Y. Bengio, H. Lipson, How transferable are features in deep neural networks?, in: Advances in neural information processing systems, pp. 3320–3328.

[44] K. Simonyan, A. Zisserman, Very deep convolutional networks for large-scale image recognition, arXiv preprint arXiv:1409.1556 (2014).

[45] O. Russakovsky, J. Deng, H. Su, J. Krause, S. Satheesh, S. Ma, Z. Huang, A. Karpathy, A. Khosla, M. Bernstein, A. C. Berg, L. Fei-Fei, ImageNet Large Scale Visual Recognition Challenge, International Journal of Computer Vision (IJCV) 115 (2015) 211–252.

[46] J. Deng, O. Russakovsky, J. Krause, M. Bernstein, A. C. Berg, L. Fei-Fei, Scalable multi-label annotation, in: ACM Conference on Human Factors in Computing Systems (CHI), pp. 3099–3102.

[47] Z. Hu, S. Mahadevan, Global sensitivity analysis using efficient distribution surrogates, in: AIAA Scitech 2019 Forum, p. 0440.

[48] C. M. Bishop, Pattern recognition and machine learning, springer, 2006.

[49] A. Saltelli, S. Tarantola, K.-S. Chan, A quantitative model-independent method for global sensitivity analysis of model output, Technometrics 41 (1999) 39–56.

[50] T. Homma, A. Saltelli, Importance measures in global sensitivity analysis of nonlinear models, Reliability Engineering & System Safety 52 (1996) 1–17.

[51] G. J. McRae, J. W. Tilden, J. H. Seinfeld, Global sensitivity analysis‘‘a computational implementation of the fourier amplitude sensitivity test (fast), Computers & Chemical Engineering 6 (1982) 15–25.

[52] A. Saltelli, T. Andres, T. Homma, Sensitivity analysis of model output: an investigation of new techniques, Computational statistics & data analysis 15 (1993) 211–238.

[53] C. Li, S. Mahadevan, An efficient modularized sample-based method to estimate the first-order sobol‘ index, Reliability Engineering & System Safety 153 (2016) 110–121.

[54] Z. Hu, S. Mahadevan, Global sensitivity analysis-enhanced surrogate (gsas) modeling for reliability analysis, Structural and Multidisciplinary Optimization 53 (2016) 501–521.

[55] S. Sankararaman, S. Mahadevan, Uncertainty quantification in structural damage diagnosis, Structural Control and Health Monitoring 18 (2011) 807–824.

[56] M. M. Petrou, C. Petrou, Image processing: the fundamentals, John Wiley & Sons, 2010.

[57] R. M. Haralick, L. G. Shapiro, Computer and robot vision, volume 1, Addison-wesley Reading, 1992.

[58] R. Jain, R. Kasturi, B. G. Schunck, Machine vision, volume 5, McGraw-Hill New York, 1995.

[59] A. Ito, Y. Aoki, S. Hashimoto, Accurate extraction and measurement of fine cracks from concrete block surface image, in: IEEE 2002 28th Annual Conference of the Industrial Electronics Society. IECON 02, volume 3, IEEE, pp. 2202–2207.

[60] Y. Fujita, Y. Mitani, Y. Hamamoto, A method for crack detection on a concrete structure, in: 18th International Conference on Pattern Recognition (ICPR'06), volume 3, IEEE, pp. 901–904.

[61] G. Van de Wouwer, P. Scheunders, D. Van Dyck, Statistical texture characterization from discrete wavelet representations, IEEE transactions on image processing 8 (1999) 592–598.

[62] S. Foucher, G. B. Bénié, J.-M. Boucher, Multiscale map filtering of sar images, IEEE Transactions on image processing 10 (2001) 49–60.

[63] A. Ammouche, D. Breysse, H. Hornain, O. Didry, J. Marchand, A new image analysis technique for the quantitative assessment of microcracks in cement-based materials, Cement and Concrete Research 30 (2000) 25–35.

[64] E. Masad, B. Muhunthan, N. Shashidhar, T. Harman, Internal structure characterization of asphalt concrete using image analysis, Journal of computing in civil engineering 13 (1999) 88–95.

[65] M. A. Rumsey, J. A. Paquette, Structural health monitoring of wind turbine blades, in: Smart Sensor Phenomena, Technology, Networks, and Systems 2008, volume 6933, International Society for Optics and Photonics, p. 69330E.

[66] L. Doliński, M. Krawczuk, Damage detection in turbine wind blades by vibration based methods, in: Journal of Physics: Conference Series, volume 181, IOP Publishing, p. 012086.

[67] P. Stanley, Applications and potential of thermoelastic stress analysis, Journal of materials processing technology 64 (1997) 359–370.

[68] B. Milovanović, I. Banjad Pečur, Detecting defects in reinforced concrete using the method of infrared thermography, HDKBR INFO Magazin 3 (2013) 3–13.

[69] A. Dutton, Thermoelastic stress measurement and acoustic emission monitoring in wind turbine blade testing, in: European Wind Energy Conference London, pp. 22–25.

[70] Z. Hameed, Y. Hong, Y. Cho, S. Ahn, C. Song, Condition monitoring and fault detection of wind turbines and related algorithms: A review, Renewable and Sustainable energy reviews 13 (2009) 1–39.

[71] N. K. Del Grande, P. F. Durbin, Precise thermal nde for quantifying structural dam-

age, in: Review of Progress in Quantitative Nondestructive Evaluation, Springer, 1996, pp. 525–531.

[72] D. G. Pollock, K. J. Dupuis, B. Lacour, K. R. Olsen, Detection of voids in prestressed concrete bridges using thermal imaging and ground-penetrating radar, Washington State Transportation Center (TRAC) (2008).

[73] R. Paynter, A. Dutton, The use of a second harmonic correlation to detect damage in composite structures using thermoelastic stress measurements, Strain 39 (2003) 73–78.

[74] N. Friedman, D. Geiger, M. Goldszmidt, Bayesian network classifiers, Machine learning 29 (1997) 131–163.

[75] Y. Wang, J. Vassileva, Bayesian network-based trust model, in: Proceedings IEEE/WIC International Conference on Web Intelligence (WI 2003), IEEE, pp. 372–378.

[76] C. M. Bishop, Pattern recognition and machine learning, springer, 2006.

[77] S. M. Kay, Fundamentals of statistical signal processing, Prentice Hall PTR, 1993.

[78] T. Ishigami, T. Homma, An importance quantification technique in uncertainty analysis for computer models, in: [1990] Proceedings. First International Symposium on Uncertainty Modeling and Analysis, IEEE, pp. 398–403.

[79] W. K. Hastings, Monte carlo sampling methods using markov chains and their applications (1970).

[80] H. Sohn, D. Dutta, J.-Y. Yang, H.-J. Park, M. DeSimio, S. Olson, E. Swenson, Delamination detection in composites through guided wave field image processing, Composites science and technology 71 (2011) 1250–1256.

[81] H. Sohn, C. R. Farrar, F. M. Hemez, J. J. Czarnecki, A review of structural health review of structural health monitoring literature 1996-2001., Technical Report, Los Alamos National Laboratory, 2002.

[82] C. R. Farrar, K. Worden, An introduction to structural health monitoring, Philosophical Transactions of the Royal Society A: Mathematical, Physical and Engineering Sciences 365 (2006) 303–315.

[83] A. Mordini, K. Savov, H. Wenzel, The finite element model updating: a powerful tool for structural health monitoring, Structural engineering international 17 (2007) 352–358.

[84] G. Qiao, T. Liu, Y. Hong, J. Ou, Optimization design of a corrosion monitoring sensor by fem for rc structures, IEEE Sensors Journal 11 (2011) 2111–2112.

[85] P. Gong, M. E. Patton, D. W. Greve, J. B. Harley, C. Liu, I. J. Oppenheim, Alkali-silica reaction (asr) detection in concrete from frequency dependent ultrasonic attenuation, in: AIP Conference Proceedings, volume 1581, AIP, pp. 909–916.

[86] P. Gong, M. E. Patton, C. Liu, I. J. Oppenheim, D. W. Greve, J. B. Harley, W. R. Junker, Ultrasonic detection of the alkali-silica reaction damage in concrete, in: 2014 IEEE International Ultrasonics Symposium, IEEE, pp. 361–364.

[87] J. G. Chen, N. Wadhwa, Y.-J. Cha, F. Durand, W. T. Freeman, O. Buyukozturk, Modal identification of simple structures with high-speed video using motion magnification, Journal of Sound and Vibration 345 (2015) 58–71.

[88] Y. Bao, P. Seshadri, S. Mahadevan, Motion magnification for quantifying aeroelastic modes from high-speed videos, in: 58th AIAA/ASCE/AHS/ASC Structures, Structural Dynamics, and Materials Conference, p. 0869.

[89] H. Sohn, H. J. Lim, M. P. DeSimio, K. Brown, M. Derriso, Nonlinear ultrasonic wave modulation for online fatigue crack detection, Journal of Sound and Vibration 333 (2014) 1473–1484.

[90] V. Agarwal, Y. Bao, S. Mahadevan, D. Adams, B. Hallbert, Data Analytics for Concrete Structural Health Monitoring in Nuclear Power Plants, Technical Report, Idaho National Lab.(INL), Idaho Falls, ID (United States), 2015.

[91] S. Mahadevan, K. Neal, P. Nath, Y. Bao, G. Cai, P. Orme, D. Adams, V. Agarwal, Quantitative diagnosis and prognosis framework for concrete degradation due to alkali-silica reaction, in: AIP Conference Proceedings, volume 1806, AIP Publishing, p. 080006.

[92] L. Pieczonka, A. Klepka, A. Martowicz, W. J. Staszewski, Nonlinear vibroacoustic wave modulations for structural damage detection: an overview, Optical engineering 55 (2015) 011005.

[93] S. Mahadevan, V. Agarwal, K. Neal, P. Nath, Y. Bao, G. Cai, P. Orme, D. Adams, D. Kosson, A Demonstration of Concrete Structural Health Monitoring Framework for Degradation due to Alkali-Silica Reaction, Technical Report, Idaho National Lab.(INL), Idaho Falls, ID (United States), 2016.

[94] N. Boffa, E. Monaco, L. Maio, V. Memmolo, F. Ricci, E. Mendoza, T. Kundu, Hybrid guided wave based shm system for composite structures for impact and delamination detection combining fiber bragg grating sensing and piezoelectric patches, in: Health monitoring of structural and biological systems XII, volume 10600, International Society for Optics and Photonics, p. 106000D.

[95] H. Choi, J. S. Popovics, Nde application of ultrasonic tomography to a full-scale concrete structure, IEEE transactions on ultrasonics, ferroelectrics, and frequency control 62 (2015) 1076–1085.

[96] C. Liu, J. Harley, N. O'Donoughue, Y. Ying, M. H. Altschul, M. Bergés, J. H. Garrett, D. W. Greve, J. M. Moura, I. J. Oppenheim, et al., Robust change detection in highly dynamic guided wave signals with singular value decomposition, in: 2012 IEEE International Ultrasonics Symposium, IEEE, pp. 483–486.

[97] C. Liu, J. Harley, N. O'Donoughue, Y. Ying, M. H. Altschul, J. H. Garrett Jr, J. M. Moura, I. J. Oppenheim, L. Soibelman, Ultrasonic monitoring of a pipe under operating conditions, in: Sensors and Smart Structures Technologies for Civil, Mechanical, and Aerospace Systems 2012, volume 8345, International Society for Optics and Photonics, p. 83450B.

[98] H. Sohn, H. J. Lim, M. P. DeSimio, K. Brown, M. Derriso, Nonlinear ultrasonic wave modulation for online fatigue crack detection, Journal of Sound and Vibration 333 (2014) 1473–1484.

[99] Y. Ying, J. H. Garrett Jr, I. J. Oppenheim, L. Soibelman, J. B. Harley, J. Shi, Y. Jin, Toward data-driven structural health monitoring: application of machine learning and signal processing to damage detection, Journal of Computing in Civil Engineering 27 (2012) 667–680.

[100] C. Liu, J. B. Harley, Y. Ying, M. H. Altschul, M. Bergés, J. H. Garrett, Jr, D. W. Greve, J. M. Moura, I. J. Oppenheim, L. Soibelman, Ultrasonic monitoring of a pressurized pipe in operation, in: Structures Congress 2013: Bridging Your Passion with Your Profession, pp. 1903–1913.

[101] Z. Hu, X. Du, Reliability analysis for hydrokinetic turbine blades, Renewable Energy 48 (2012) 251–262.

[102] C. R. Farrar, K. Worden, An introduction to structural health monitoring, Philosophical Transactions of the Royal Society A: Mathematical, Physical and Engineering Sciences 365 (2006) 303–315.

[103] Y. Ying, J. H. Garrett Jr, I. J. Oppenheim, L. Soibelman, J. B. Harley, J. Shi, Y. Jin, Toward data-driven structural health monitoring: application of machine learning and signal processing to damage detection, Journal of Computing in Civil Engineering 27 (2012) 667–680.

[104] Y. Bao, S. Mahadevan, Harmonic vibration testing for damage detection and localization in concrete, Structural Health Monitoring (2018) 1475921718816837.

[105] I. Abdel-Qader, O. Abudayyeh, M. E. Kelly, Analysis of edge-detection techniques for crack identification in bridges, Journal of Computing in Civil Engineering 17 (2003) 255–263.

[106] C. M. Yeum, S. J. Dyke, Vision-based automated crack detection for bridge inspection, Computer-Aided Civil and Infrastructure Engineering 30 (2015) 759–770.

[107] T. Nishikawa, J. Yoshida, T. Sugiyama, Y. Fujino, Concrete crack detection by multiple sequential image filtering, Computer-Aided Civil and Infrastructure Engineering 27 (2012) 29–47.

[108] S. German, I. Brilakis, R. DesRoches, Rapid entropy-based detection and properties measurement of concrete spalling with machine vision for post-earthquake safety assessments, Advanced Engineering Informatics 26 (2012) 846–858.

[109] Y.-J. Cha, K. You, W. Choi, Vision-based detection of loosened bolts using the hough transform and support vector machines, Automation in Construction 71 (2016) 181–188.

[110] P.-H. Chen, H.-K. Shen, C.-Y. Lei, L.-M. Chang, Support-vector-machine-based method for automated steel bridge rust assessment, Automation in Construction 23 (2012) 9–19.

[111] J. Park, T. Kim, J. Kim, Image-based bolt-loosening detection technique of bolt joint in steel bridges, in: 6th international conference on advances in experimental structural engineering, University of Illinois, Urbana-Champaign.

[112] E. Zalama, J. Gómez-García-Bermejo, R. Medina, J. Llamas, Road crack detection using visual features extracted by gabor filters, Computer-Aided Civil and Infrastructure Engineering 29 (2014) 342–358.

[113] C. Koch, I. Brilakis, Pothole detection in asphalt pavement images, Advanced Engineering Informatics 25 (2011) 507–515.

[114] A. Cord, S. Chambon, Automatic road defect detection by textural pattern recognition based on adaboost, Computer-Aided Civil and Infrastructure Engineering 27 (2012) 244–259.

[115] X. Zhao, H. Gao, G. Zhang, B. Ayhan, F. Yan, C. Kwan, J. L. Rose, Active health monitoring of an aircraft wing with embedded piezoelectric sensor/actuator network: I. defect detection, localization and growth monitoring, Smart materials and structures 16 (2007) 1208.

[116] C. C. Ciang, J.-R. Lee, H.-J. Bang, Structural health monitoring for a wind turbine system: a review of damage detection methods, Measurement science and technology 19 (2008) 122001.

[117] Y. Bao, S. Mahadevan, Uncertainty quantification of thermal image-based concrete diagnosis, International Journal of Sustainable Materials and Structural Systems 2 (2015) 77–95.

[118] Y. Bao, P. Seshadri, S. Mahadevan, Motion magnification for quantifying aeroelastic modes from high-speed videos, in: 58th AIAA/ASCE/AHS/ASC Structures, Structural Dynamics, and Materials Conference, p. 0869.

[119] P. Tamilselvan, P. Wang, Failure diagnosis using deep belief learning based health state classification, Reliability Engineering & System Safety 115 (2013) 124–135.

[120] Z. Chen, W. Li, Multisensor feature fusion for bearing fault diagnosis using sparse autoencoder and deep belief network, IEEE Transactions on Instrumentation and Measurement 66 (2017) 1693–1702.

[121] A. Zhang, K. C. Wang, B. Li, E. Yang, X. Dai, Y. Peng, Y. Fei, Y. Liu, J. Q. Li, C. Chen, Automated pixel-level pavement crack detection on 3d asphalt surfaces using a deep-learning network, Computer-Aided Civil and Infrastructure Engineering 32 (2017) 805–819.

[122] Y.-J. Cha, W. Choi, G. Suh, S. Mahmoudkhani, O. Büyüköztürk, Autonomous structural visual inspection using region-based deep learning for detecting multiple damage types, Computer-Aided Civil and Infrastructure Engineering 33 (2018) 731–747.

[123] C. Lu, Z.-Y. Wang, W.-L. Qin, J. Ma, Fault diagnosis of rotary machinery components using a stacked denoising autoencoder-based health state identification, Signal Processing 130 (2017) 377–388.

[124] S. Tao, T. Zhang, J. Yang, X. Wang, W. Lu, Bearing fault diagnosis method based on stacked autoencoder and softmax regression, in: 2015 34th Chinese Control Conference (CCC), IEEE, pp. 6331–6335.

[125] Y.-J. Cha, K. You, W. Choi, Vision-based detection of loosened bolts using the hough transform and support vector machines, Automation in Construction 71 (2016) 181–188.

[126] R. Mullen, T. Belytschko, An analysis of an unconditionally stable explicit method, Computers & Structures 16 (1983) 691–696.

[127] A. Coates, A. Ng, H. Lee, An analysis of single-layer networks in unsupervised feature learning, in: Proceedings of the fourteenth international conference on artificial intelligence and statistics, pp. 215–223.

[128] Y. Bengio, A. Courville, P. Vincent, Representation learning: A review and new perspectives, IEEE transactions on pattern analysis and machine intelligence 35 (2013) 1798–1828.

[129] N. N. Hoavy, J. Mothe, M. I. Randrianarivony, Irit & misa at image clef 2017-multi label classification.

[130] A. Sharif Razavian, H. Azizpour, J. Sullivan, S. Carlsson, Cnn features off-the-shelf: an astounding baseline for recognition, in: Proceedings of the IEEE conference on computer vision and pattern recognition workshops, pp. 806–813.

[131] J. E. Beck, B. P. Woolf, High-level student modeling with machine learning, in: International Conference on Intelligent Tutoring Systems, Springer, pp. 584–593.

[132] F. Tramèr, F. Zhang, A. Juels, M. K. Reiter, T. Ristenpart, Stealing machine learning models via prediction apis, in: 25th USENIX Security Symposium (USENIX Security 16), USENIX Association, Austin, TX, 2016, pp. 601–618.

[133] X. Zhang, S. Mahadevan, Bayesian neural networks for flight trajectory prediction and safety assessment, Decision Support Systems (2020) 113246.

[134] R. Gade, T. B. Moeslund, Thermal cameras and applications: a survey, Machine vision and applications 25 (2014) 245–262.

[135] Z. Zhang, M. Sabuncu, Generalized cross entropy loss for training deep neural networks with noisy labels, in: Advances in neural information processing systems, pp. 8778–8788.

[136] P. Karve, S. Miele, K. Neal, S. Mahadevan, V. Agarwal, E. Giannini, P. Kyslinger, Vibro-acoustic modulation and data fusion for localizing alkali-silica-reaction-induced damage in concrete, 2020. (in press).

[137] S. Miele, Y. Bao, P. Karve, S. Mahadevan, V. Agarwal, E. Giannini, J. Zhu, Vibration-Based Techniques for Concrete Structural Health Monitoring, Technical Report, Idaho National Lab.(INL), Idaho Falls, ID (United States), 2019.

[138] S. Mahadevan, K. Neal, P. Nath, Y. Bao, G. Cai, P. Orme, D. Adams, V. Agarwal, Quantitative diagnosis and prognosis framework for concrete degradation due to alkali-silica reaction, in: AIP Conference Proceedings, volume 1806, AIP Publishing, p. 080006.

[139] S. Mahadevan, S. Miele, K. Neal, Y. Bao, V. Agarwal, B. T. Pham, D. Adams, Light Water Reactor Sustainability Program Interrogation of Alkali-Silica Reaction Degraded Concrete Samples using Acoustic and Thermal Techniques to Support Development of a Structural Health Monitoring Framework, Technical Report, Idaho National Lab.(INL), Idaho Falls, ID (United States), 2017.

[140] S. Mahadevan, V. Agarwal, G. Cai, P. Nath, Y. Bao, J. M. Bru Brea, D. Koester, D. Adams, D. Kosson, A Simple Demonstration of Concrete Structural Health Monitoring Framework, Technical Report, Idaho National Lab.(INL), Idaho Falls, ID (United States), 2015.

[141] Z. Perkowski, Change of thermal conductivity of concrete caused by brittle damage evolution, Bauphysik 30 (2008) 434–437.

[142] Y. Gal, Z. Ghahramani, Bayesian convolutional neural networks with bernoulli approximate variational inference, arXiv preprint arXiv:1506.02158 (2015).

[143] Y. Gal, Z. Ghahramani, Dropout as a bayesian approximation: Representing model

uncertainty in deep learning, in: international conference on machine learning, pp. 1050–1059.

[144] Y. Gal, Z. Ghahramani, A theoretically grounded application of dropout in recurrent neural networks, in: Advances in neural information processing systems, pp. 1019–1027.

[145] B. Lakshminarayanan, A. Pritzel, C. Blundell, Simple and scalable predictive uncertainty estimation using deep ensembles, in: Advances in Neural Information Processing Systems, pp. 6402–6413.

[146] L. Zhu, N. Laptev, Deep and confident prediction for time series at uber, in: 2017 IEEE International Conference on Data Mining Workshops (ICDMW), IEEE, pp. 103–110.

[147] X. Zhang, Machine Learning and Optimization Models to Assess and Enhance System Resilience, Ph.D. thesis, Vanderbilt University, 2019.

[148] N. Srivastava, G. Hinton, A. Krizhevsky, I. Sutskever, R. Salakhutdinov, Dropout: a simple way to prevent neural networks from overfitting, The journal of machine learning research 15 (2014) 1929–1958.

[149] S. Sankararaman, S. Mahadevan, Bayesian methodology for diagnosis uncertainty quantification and health monitoring, Structural Control and Health Monitoring 20 (2013) 88–106.